UNIVERSITÀ DEGLI STUDI
DI MODENA E REGGIO EMILIA

Dottorato di Ricerca in Ingegneria Industriale e del Territorio

Ciclo XXXVIII

Numerical studies of urban climate in paradigmatic environments

Relatore: Prof. Andrea Cimarelli

Candidata: Anna Pavan

Correlatore: Prof. Enrico Stalio

Coordinatore del Corso di Dottorato: Prof. Alberto Muscio

Ai miei nonni,
Ada, Liliana, Giuseppe e Romano

Abstract

Urban climate is an expanding research field that poses a wide range of scientific challenges, particularly in view of future climate change and increasing urbanisation. As expected, the urban canopy plays a central role in the dynamics of urban climate flows. Simplified geometries, typically consisting of arrays of parallelepipeds, have been extensively investigated in the literature through both numerical simulations and laboratory experiments, including studies focusing on limited portions of real urban environments and considering either calm or perturbed conditions. Despite these efforts, the dependence of the flow dynamics on the specific geometrical and physical characteristics of the urban configuration makes it difficult to achieve a comprehensive understanding of the complex phenomena involved and hinders the development of a sufficiently general theoretical framework. To address this limitation, this thesis proposes a novel approach based on the development of a paradigmatic flow configuration aimed at reproducing the essential features of urban environments. The methodology relies on an idealised urban canopy described by a minimal set of five measurable statistical parameters, thereby enabling a general assessment of the key urban characteristics governing the urban climate without restricting the applicability of the results to a narrow range of configurations. The potential of this paradigmatic framework is assessed with the objective of establishing a robust best-practice methodology for urban climate studies. Direct Numerical Simulation (DNS) is first conducted to provide fully resolved reference data, by considering the conditions of natural convection at fixed Prandtl $\mathrm{Pr} = 0.7$ and Rayleigh $\mathrm{Ra} = 10^8$ numbers, in order to reproduce the urban heat island effect during summer nights in the absence of wind. Subsequently, coarse grained simulations are performed, to reduce the computational cost while retaining the capability to capture the dominant flow structures and heat transfer mechanisms. Furthermore, a parametric study is carried out to disclose the role of selected key urban parameters in shaping the urban climate. The interaction between urban geometry and heat transfer mechanisms is analysed under both pure natural convection and mixed convection conditions, the latter characterised by a Richardson number of approximately

Ri ~ 1, accounting for the additional effect of an incoming colder mean wind. Overall, the results demonstrates the capability of the proposed framework to systematically investigate the influence of fundamental urban parameters and to identify the key physical processes governing the urban climate.

Table of Contents

Chapter 1

Introduction

Driven by the global population growth, which has accelerated over the last decades, and is projected to continue rising steadily in the coming years, urban areas are expected to expand significantly, due to their high population density. Within this evolving urban context, cities are particularly vulnerable to meteorological hazards as a result of the concentration of people, assets, infrastructure, and capital stocks, which has led to growing concern over urban climate issues and contributed to the rapid expansion of this research field (Masson et al., 2020). In this context, Urban Heat Island (UHI), which refers to urbanised areas that are warmer than their surroundings, is the most studied phenomenon in the urban climate field due to its impact, which ranges from human health to ecological changes. Since its first documentation in London (Howard, 1818), numerous studies have investigated the UHI phenomenon, showing how it manifests across diverse geographic and climatic contexts or in real urban environments such as Hannover (Kabisch et al., 2023), Toulouse (Masson et al., 2020), and cities across South Asia, for a review see Kotharkar et al. (2018). As suggested in Oke et al. (2017), land artificialization is one of the major factors influencing UHI. In particular, the urban canopy plays a central role in the dynamics of the UHI flow, where a typical flow feature is known as the urban heat island circulation (UHIC) (Wang et al., 2020) which has been investigated using both numerical simulations and experiments under calm or perturbed wind conditions. In the case of natural convection above a horizontally heated urban surface, with no wind present, the dominant flow feature is the thermal urban plume, a portion of the fluid with a temperature contrast with respect to the background and originating from the canopy. This convective structure, first proposed by Clarke (1969), can be classified based on the aspect ratio (AR) between the plume height and the source diameter, as proposed by Lu et al. (1997). Two distinct regimes are identified: the plume ($AR > 1$) and the dome ($AR < 0.1$). The former is characterised by a neck that separates the lower and upper parts of the flow, with entrainment occurring along the sides. In contrast, the latter exhibits limited vertical development, and entrainment is replaced by lateral shear layers, as

described by Fan et al. (2020).

The understanding of the complex dynamics that occur within the Urban Canopy Layer (UCL), which extends from the ground up to the height of the dominant urban elements, is essential for weather forecasting models. Indeed, the transport of momentum, heat and pollutants within the urban canopy is strongly affected by the spatial heterogeneity of the urban canopy (Barlow and Coceal, 2008). In this regard, the effect of the urban environment is commonly described by parameters such as the plan area index, ratio between the total building area and the total plan area, the frontal area index, the ratio between the building frontal area and the total plan area, and the average building height (Masson et al., 2020; Sutzl, 2021; Chen et al., 2021; Rostami et al., 2024; Coceal et al., 2006; Abd Razak et al., 2013). Such parameters are also used in urban landscape generators (ULG) (Sützl and van Reeuwijk, 2020; Wilson et al., 2025) where the nature of the geometries enable controlled studies of urban morphology at a neighbourhood scale (Wilson et al., 2026) but restricted to periodic or tiled domains. However, such features are not directly resolved in mesoscale atmospheric models such as the Weather Research and Forecasting (WRF) model but rather are parametrized. As a consequence, a deeper understanding and rationalization of the transport mechanisms at the neighbourhood scale would certainly impact the accuracy of the parametrizations of surface fluxes of momentum and heat commonly employed in weather forecasting models.

In order to address this problem, scale-resolving simulations are often used to provide detailed information about the small-scale physics of the urban canopy layer. Most of the scale-resolving simulations performed are based on a large-eddy simulation (LES) approach (Giometto et al., 2016; Kanda et al., 2013; Xie and Castro, 2009). As a matter of facts, LES models such as uDales (Suter et al., 2022) and PALM (Maronga et al., 2020), have successfully shown to enable building-resolving simulations and the solution of the surface energy balance over complex urban geometries at the neighbourhood scale (Belda et al., 2021; Sützl et al., 2021). However, LES remains inherently model-dependent, as only the large scales are explicitly solved while the subgrid-scales are modelled and because of the typical use, in urban applications, of wall functions to represent both momentum and heat surface fluxes. To overcome these limitations of accuracy, direct numerical simulation (DNS) constitutes a possible solution, resolving all scales of motion without modelling assumptions, but at the expense of the computational cost.

In addition to the lack of accuracy, a second limitation of current investigations is the focus on neighbourhood-scale configurations thus loosing

relevant phenomena related to rural-urban coupling such as the flow circulation at the city scale. Indeed, many simulations consider limited districts, which are appropriate for local transport but do not capture the overall urban-rural flow circulation. Furthermore, numerous studies have considered simplified representations of the urban roughness. These typically consist of periodic arrays of cubic or rectangular obstacles, either aligned or staggered, and often elongated to mimic street canyons (Castro et al., 2017; Leonardi and Castro, 2010; Blunn et al., 2022; Xie et al., 2008). Such idealized approaches certainly enable controlled studies of the effect of urban morphology at a neighbourhood scale on the dynamic of the UCL (Wilson et al., 2026) but restricted to periodic or tiled domains. Consequently, the symmetries introduced by such idealisations may not fully represent the intrinsic heterogeneity and irregularity of real urban environments (Barlow et al., 2017).

Overall, the use of simplified urban canopies restricted to periodic or tiled domains highlight limitations of existing simulations on neighbourhood-scale configurations where large-scale circulations related to rural-urban coupling are missed and where the solution is affected by the symmetries induced by the idealized urban landscape generator adopted. Furthermore, the use of LES approaches coupled with wall models for the surface fluxes of heat and momentum highlights limitations in terms of reliability of the solutions obtained. The aim of the present work is to address these two issues by developing a general understanding of the urban climate phenomena without constraining the applicability of results to a narrow range of scenarios. The design of paradigmatic urban environments, that are well-defined from a statistical point of view, and the simulation of entire urban landscapes are identified in the present investigation as the two key aspects for accessing the essential features of urban climate. In particular, we design a paradigmatic urban canopy composed of non-periodic hexahedral buildings whose geometric aspect ratios, orientations and arrangement are locally random but globally well-defined. Thus, the paradigmatic city is defined from a statistical point of view by five key non-dimensional parameters: the average coverage frequency, the building fraction, the average aspect ratio of the building planform area, the average aspect ratio of the building heights and the coefficient describing the radial shape of the city skyline. As it will be shown in the following, these parameters effectively capture the main statistical features of cities.

Furthermore, a reference configuration composed of hexahedral buildings representing a small village, is first investigated through direct numerical simulation under pure convection conditions, characterized by inhomoge-

neous temperature boundary condition design to mimic a nocturnal urban heat island scenario. Results from DNS are then compared with those of Large Eddy Simulations, where grid resolution and turbulence closures are varied to provide guidelines for high fidelity coarse grained simulations, still lacking in literature. Finally the validated, coarse-grained approach, is employed in a parametric study where the morphological parameters are varied to understand their impact on urban climate. This last analysis is further extended to mixed-convection conditions, accounting for the combined effects of buoyancy and externally imposed mean flow interacting with the urban canopy.

The thesis is structured as follows. Chapter 2 introduces the reduced set of morphological parameters used to generate the idealised urban configurations and describes the algorithm developed to construct the corresponding paradigmatic canopy patterns. The numerical methodology is then presented in chapter 3, where both the direct numerical simulations (DNS) and the coarse-grained modelling approaches are outlined. In chapter 4 results from the DNS analysis of a paradigmatic urban heat island under pure-convection conditions are presented, with emphasis on both the mean-flow organisation and the associated turbulent dynamics. Building on this reference case, the coarse-grained simulation campaign is examined in chapter 5, where the performance of LES approaches is assessed and their modelling implications are discussed. Chapter 6 extends the analysis to mixed-convection conditions, focusing on the response of the reference configuration to the combined action of buoyancy and external forcing. A broader parametric investigation is presented in chapter 7, where eight different urban configurations are analysed under both pure and mixed convection regimes. Finally, concluding remarks are reported in chapter 8. Appendices A and B present selected results from research activities conducted during my PhD within the framework of Master's thesis that I co-supervised.

Chapter 2

Paradigmatic city patterns

Several investigations in urban climate are based on urban patterns extracted from real-case cities or parts of them. Although realistic, such configurations inherently restrict the general applicability of the results. Furthermore, most numerical and experimental investigations adopt simplified geometries, typically cuboids or elongated rectangular blocks either aligned or staggered, or stretched to represent urban canyons (Xie and Castro, 2006; Abd Razak et al., 2013; Castro et al., 2017). In fact, urban models often describe city structures using morphological parameters such as the plan area index, λ_p, the ratio between the total buildings area and the total plan area, the frontal area index λ_f, the ratio between the building frontal area to the total plan area and the standard deviation of the building height σ_h, among other. Many parametrizations of airflow above cities are based on these and similar surface descriptors (Masson et al., 2020; Chen et al., 2021; Sutzl, 2021; Rostami et al., 2024). However, the multi-scale nature of urban flow dynamics complicates the identification of the primary parameters controlling the urban climate. To this end, idealized configurations remain essential for identifying general flow behaviours and isolating the effects of key morphological parameters in urban environments. Hence, the use of paradigmatic urban configuration described by a limited number of statistical parameters, provides a more systematic approach than relying on detailed reconstructions of specific cities, which would constrain the applicability of the results to a narrow range of scenarios, characterized by the same statistical properties.
The aim of this chapter is to introduce the five parameters identified as characterising urban configurations and to describe the main stages of the numerical algorithm used for the generation of paradigmatic cities of arbitrary shape investigated in this thesis.

2.1 Geometrical parametrization

The numerical algorithm that we propose, was developed for this thesis work with the aim of create idealized urban configuration that could also rep-

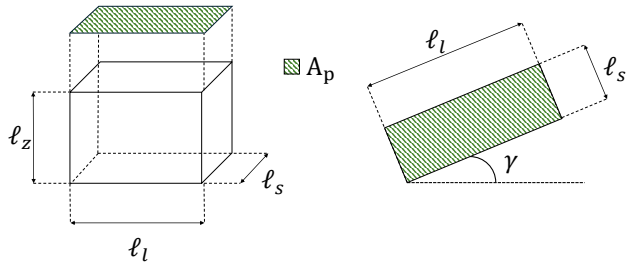

Figure 2.1: Schematic representation of the dimensions and orientation of the parallelepipeds.

resent the main features of real complex city pattern, for the study of urban climate. For that purpose, the urban canopy is composed by an ensemble of hexahedral buildings, distributed within a circular domain of radius R. Each hexahedral building exhibits unique dimensions, shape and orientation and the distinctive character of each urban configuration is ensured only globally by imposing that the ensemble of buildings statistically respect a minimal set of five key urban parameters. In this way, morphological diversity is preserved within a statistically controlled framework. The first four key urban parameters that are statistically targeted by the developed paradigmatic urban environment are:

$$N = \frac{A_T}{A_p} \qquad \lambda_p = \frac{nA_p}{A_T} \qquad \mathcal{AR}_p = \langle \frac{\ell_l}{\ell_s} \rangle_b \qquad \mathcal{AR}_z = \frac{\langle \ell_z \rangle_b}{\sqrt{A_p}} \tag{2.1}$$

The longer and the shorter planform lengths and the buildings height are denoted by ℓ_l, ℓ_s and ℓ_z respectively, see figure 2.1. The notation $\langle \cdot \rangle_b$ indicates the algebraic average taken over all buildings. The average planform area of buildings is defined as $A_p = \langle \ell_l \ell_s \rangle_b$ while the total urban area is given by $A_T = \pi R^2$, where R is the city radius, as defined before. If n denotes the actual number of buildings contained within the urban domain, the statistical parameter N represents the maximum number of buildings that can be placed in the city, being the ratio between the urban area and the average building planform area. The density coverage of buildings, commonly referred to as the plan area index is λ_p. Lastly, $\mathcal{AR}_p$ and $\mathcal{AR}_z$ are the average buildings planform and vertical aspect ratio, respectively. The fifth parameter, denoted by ϵ, is employed to describe the heterogeneous distribution of building heights among different radial distances from the city

centre, thus defining the city skyline. It identifies the radial envelope $g(r)$, a Gaussian distribution whose average in the range $[0, R]$ is unity prescribed by ϵ, that is statistically imposed to the building heights:

$$\langle \ell_z \rangle_{b,r} = g(r)\langle \ell_z \rangle_b = \frac{2}{\sqrt{\pi\epsilon}\,\mathrm{erf}(1/\sqrt{\epsilon})}\; e^{-r^2/(\epsilon R^2)}\langle \ell_z \rangle_b \tag{2.2}$$

A fundamental feature of this framework is that, by varying the parameters described above, it is possible to generate an arbitrary number of distinct roughness configurations, or equivalently, distinct urban patterns. Each configuration is uniquely defined, from a statistical perspective, by a minimal set of five key urban parameters $(N, \lambda_p, \mathcal{AR}_p, \mathcal{AR}_z, \epsilon)$ that can be evaluated in every urban configuration. This formulation enables a systematic and quantitative assessment of the influence of each parameter on urban climate.

2.2 Generation of the urban configurations

The pattern generation process starts after setting as the reference length the city radius R, thus defining the total city area $A_T = \pi$, that combined with the established urban statistical parameters, $(N, \lambda_p, \mathcal{AR}_p, \mathcal{AR}_z, \epsilon)$, allow to compute the shape and the orientation of each building according to the relations reported below:

$$\ell_l = \sqrt{A_p}\mathcal{AR}_p f' \tag{2.3}$$

$$\ell_s = \frac{\ell_l}{\mathcal{AR}_p} f'' \tag{2.4}$$

$$\ell_z = g(r)\sqrt{A_p}\mathcal{AR}_z f''' \tag{2.5}$$

$$\gamma = \frac{\pi}{2} g' \tag{2.6}$$

where γ is the planar orientation of the building, see figure 2.1. Various random number generator functions f centred in the interval $[0.5; 1.5]$ and g' centred in the interval $[-1; 1]$ are used to brake symmetries in the city configuration. As a consequence, the irregularity of building orientation, shape and dimensions can be reproduced as in real urban scenarios. Subsequently this first step, each building is placed in the city area by applying a displacement (2.7) which consider a building clearance length that is statistically available in the city pattern.

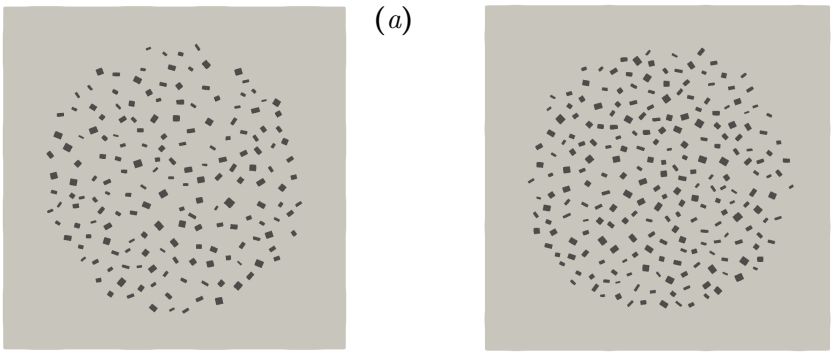

Figure 2.2: Effect of λ_p on the resulting city layout obtained for $(N, \mathcal{AR}_p, \mathcal{AR}_z, \epsilon) = (2243, 1.7, 1, 0.6)$. Panel (a) shows the city configuration obtained for $\lambda_p = 0.08$, while panel (b) shows the city configuration for λ_p=0.11.

$$\delta = \delta_f f'''' \qquad \text{with} \quad \delta_f = \sqrt{A_T}/n - \sqrt{A_p} \tag{2.7}$$

This last random number generator f'''', again centred in the interval $[0.5; 1.5]$ allows for a globally homogeneous but locally irregular distribution of buildings. We recall that the staggered or non-staggered homogeneous distribution of buildings introduces symmetries in the flow solutions that are not representative of urban climate.
Several city patterns have been generated in order to address the effect of the five statistical parameters $(N, \lambda_p, \mathcal{AR}_p, \mathcal{AR}_z, \epsilon)$ on the final layout of the city. As can be seen in figure 2.2, by maintaining all other parameters fixed, an increase of the density coverage index is related to an increase of the number of buildings n. While a decrease in the radial smoothing coefficient ϵ, leads to an enhanced radial non-homogeneity of the heights of the buildings between the centre and the periphery of the city, figure 2.3.

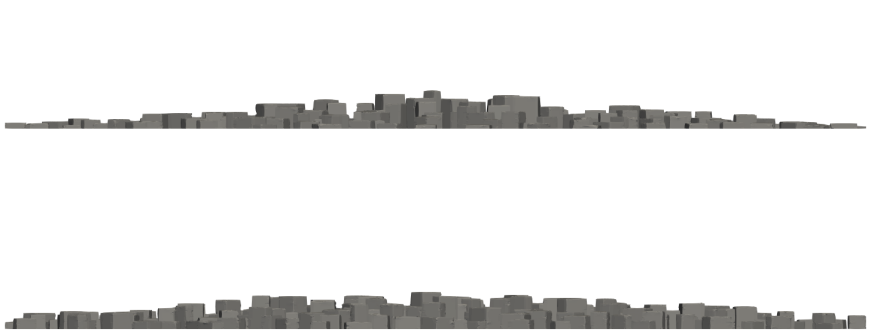

Figure 2.3: Effect of ϵ on the resulting city skyline obtained for $(N, \lambda_p, \mathcal{AR}_p, \mathcal{AR}_z) = (2094, 0.8, 1.68, 1.68)$. The city skyline obtained for $\epsilon = 0.7$ is reported in panel (a) while panel (b) shows the skyline obtained for $\epsilon = 1$.

2.3 Reference configuration

The first urban configuration analysed and adopted as reference for the best-practice assessment is characterized by $(N, \lambda_p, \mathcal{AR}_p, \mathcal{AR}_z, \epsilon) = (1963, 0.08, 1.7, 1.68, 1.08)$, and composed of 176 buildings randomly distributed in the city area. This is representative of a small town. Figures 2.4–2.5 show a horizontal and vertical view, to emphasise the building arrangements in the city area and the vertical profile of the canopy. Furthermore, the value selected for the parameter governing the city skyline ϵ is such that the height of buildings in the city center is 30% higher than the average $\langle \ell_z \rangle_b$, while in the periphery it is 45% lower, mimicking the tendency of real urban areas to exhibit taller cores respect to the outlying areas.

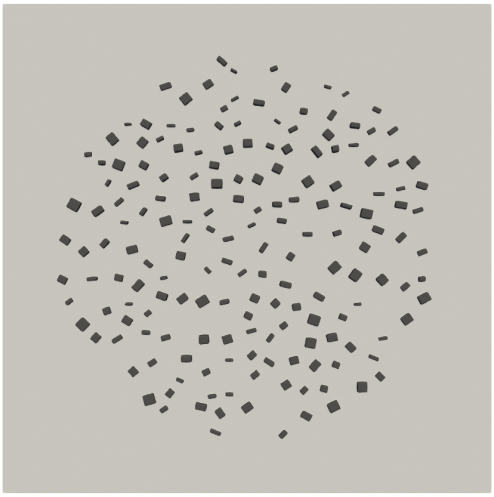

Figure 2.4: Top view of the reference configuration showing the buildings distribution.

Figure 2.5: Skyline of the reference configuration.

Chapter 3

Numerical Techniques

This chapter presents the two numerical codes employed in this thesis for the simulation of urban climate in paradigmatic configurations. In particular, the focus is on CaNS, including the specific implementations required for the present set-up, and on OpenFOAM, in which the Wall Adapting Local Eddy-viscosity (WALE) model is employed for the coarse grained simulations.

3.1 CaNS

The direct numerical simulation of the urban heat island in pure convection condition, is performed with with the massively-parallel open-source code CaNS, Canonical Navier-Stokes (Costa, 2018). CaNS solves the incompressible Navier–Stokes equations for constant-density flows with kinematic viscosity ν:

$$\begin{cases} \dfrac{\partial u_i}{\partial x_i} = 0 \\ \dfrac{\partial u_i}{\partial t} + \dfrac{\partial (u_i u_j)}{\partial x_j} = -\dfrac{\partial p}{\partial x_i} + \nu \dfrac{\partial^2 u_i}{\partial x_j \partial x_j} \end{cases} \tag{3.1}$$

where $i, j = 1, 2, 3$ denote the Cartesian components of the velocity field u and p is the pressure field. Equations (3.1), are solved in a structured Cartesian grid. The code uses a standard pressure-correction method with the spatial discretization based on a staggered second-order finite-difference scheme. Furthermore time integration uses a low storage, three-step Runge-Kutta. The Poisson equation for the pressure field is efficiently computed using a direct FFT-based solver. This FFT solver leverages eigenfunction expansions, significantly reducing computational cost and enabling high scalability on parallel computing architectures. This combination of numerical methods allows for the accurate and efficient resolution of the full range of turbulence scales critical for the detailed study of urban climate.

To resolve the complex flow within the urban canopy, an immersed boundary method (IBM) has been exploited, following the formulation proposed by Yang and Balaras (2006). The IBM approach has been adopted in order to preserve the degree of accuracy of the DNS approach also within the canopy region but avoiding the use of large number of discretization points that would be otherwise required by using mesh-fitted discretization. The implemented IBM relies on a sign distance field Φ to identify the solid boundaries and their normals. In particular, the sign distance field is defined at each grid point of the computational domain, with the solid boundaries identified as the isosurface $\Phi = 0$. Positive and negative values of Φ correspond to the fluid and solid regions respectively. The gradient of the sign distance field $\nabla\Phi$ unequivocally defines the normals to the solid boundaries ($\Phi = 0$) and is used to identify the forcing and interpolation points used by the IBM method to impose the desired boundary conditions.

3.2 OpenFOAM

While CaNS is employed for the DNS reference simulation, the coarse-grained simulations under both pure and mixed convection conditions are performed using OpenFOAM (OpenFOAM Foundation, 2024). Similar to CaNS, OpenFOAM is a free, open-source software widely adopted for its extensive multiphysics simulation capabilities, ranging from incompressible flow to fluid structure interactions. In this work, the ESI release OpenFOAM v2406 is used. This version was selected due to its correct implementation of the Boussinesq approximation, within the *buoyantboussinesqSimpleFoam* solver. In fact, under the Boussinesq approximation, density variations with temperature Θ are accounted for only in the buoyancy term of the momentum equation, while density is treated as constant elsewhere:

$$\rho = \rho_0(1 - \beta(\Theta - \Theta_0)) \tag{3.2}$$

where ρ denotes the density, β the thermal expansion coefficient and the subscript 0 refers to reference conditions. It is worth noting that the formulation of the Boussinesq approximation may differ across OpenFOAM distributions, as a results in some versions, density variations are not confined strictly to the buoyancy term of the momentum equation. In contrast to CaNS, which relies on a finite difference formulation, OpenFOAM is based on the finite volume method and the urban geometries are represented using a body-fitted mesh generated through a combination of Gmsh and the *snappyHexMesh* utility.

3.2.1 WALE Model

The filtered Navier-Stokes equations under the Boussinesq approximation written in a non dimensional form using H, the free fall velocity U_{ff} and the temperature Θ as reference scales for lengths, velocity and temperature reads as follows:

$$\begin{cases} \dfrac{\partial \tilde{u}_i}{\partial x_i} = 0 \\ \dfrac{\partial \tilde{u}_i}{\partial t} + \tilde{u}_j \dfrac{\partial \tilde{u}_i}{\partial x_j} = -\dfrac{\partial \tilde{p}}{\partial x_i} + \tilde{\theta}\delta_{i,3} + \sqrt{\dfrac{\mathrm{Ra}}{\mathrm{Pr}}} \dfrac{\partial^2 \tilde{u}_i}{\partial x_j^2} - \dfrac{\partial \tau_{i,j}}{\partial x_j} \\ \dfrac{\partial \tilde{\theta}}{\partial t} + \tilde{u}_j \dfrac{\partial \tilde{\theta}}{\partial x_j} = \sqrt{\dfrac{1}{\mathrm{Ra}\,\mathrm{Pr}}} \dfrac{\partial^2 \tilde{\theta}}{\partial x_j^2} - \dfrac{\partial \sigma_j}{\partial x_j} \end{cases} \tag{3.3}$$

where $(\tilde{\cdot})$ denotes filtered quantities. The subgrid-scale (SGS) stress tensor and the subgrid-scale scalar flux are defined as $\tau_{i,j} = \widetilde{u_i u_j} - \tilde{u}_i \tilde{u}_j$ and $\sigma_j = \widetilde{\theta u_j} - \tilde{\theta}\tilde{u}_j$ respectively and Ra and Pr denote the Rayleigh and Prandtl numbers. While for the ILES the grid spacing Δ, acts as an implicit filter width and no explicit SGS is introduced, in contrast, for the LES computations that we will perform, the Wall Adapting Local Eddy-viscosity (WALE) model is adopted as subgrid-scale (SGS) closure (Nicoud and Ducros, 1999). The WALE model is specifically designed to provide the correct near-wall scaling of the eddy viscosity without the need for dynamic procedures, making it particularly suitable for wall-bounded flows. This feature is of primary importance in urban canopy configurations, where accurate representation of shear layers and near-wall turbulence strongly influences the overall mixing and heat transfer. Compared to dynamic models, WALE offers a robust and computationally efficient formulation while preserving appropriate behaviour in the vicinity of solid boundaries.

Chapter 4

Direct Numerical Simulation of pure convection in a paradigmatic urban environment

The fluid dynamics phenomena that govern the urban climate are investigated in the paradigmatic city pattern defined in chapter 2 under the conditions of pure thermal convection, in the absence of wind. The geometrical simplicity of the designed paradigmatic city enables the use of a Direct Numerical Simulation (DNS) approach for the solution of the governing equations. After a brief introduction and description of the set-up, results will be shown and analysed.

4.1 Flow settings

The governing equations under the Boussinesq approximation (Gray and Giorgini, 1976; Cimarelli et al., 2025) in a dimensionless form read as follows:

$$\begin{cases} \dfrac{\partial u_i}{\partial x_i} = 0 \\ \dfrac{\partial u_i}{\partial t} + \dfrac{\partial (u_i u_j)}{\partial x_j} = -\dfrac{\partial p}{\partial x_i} + \sqrt{\dfrac{\mathrm{Pr}}{\mathrm{Ra}}} \dfrac{\partial^2 u_i}{\partial x_j \partial x_j} + \theta \delta_{i3} \\ \dfrac{\partial \theta}{\partial t} + \dfrac{\partial (\theta u_j)}{\partial x_j} = \dfrac{1}{\sqrt{\mathrm{Ra}\,\mathrm{Pr}}} \dfrac{\partial^2 \theta}{\partial x_i \partial x_i} \end{cases} \tag{4.1}$$

where $i, j = 1, 2, 3$ denote the horizontal $x - y$ and vertical z directions and δ_{ij} represents the Kronecker delta. Variables $u_1 = u$ and $u_2 = v$ de-

note the horizontal velocity components and $u_3 = w$ the vertical velocity component. Pressure and temperature field are p and θ respectively. The dimensionless form of the governing equations (4.1) is obtained by using the height H of the domain, the highest temperature difference imposed between the top and bottom boundaries $\Delta\Theta_{max}$, and the free-fall velocity $U_{ff} = \sqrt{g\beta\Delta\Theta_{max}H}$ as characteristic scales. Consequently, the two dimensionless numbers, the Rayleigh number and the Prandtl number, are defined:

$$\mathrm{Ra} = \frac{g\beta\Delta\Theta_{max}H^3}{(\alpha\nu)} \qquad \mathrm{Pr} = \frac{\nu}{\alpha} \tag{4.2}$$

where ν is the kinematic viscosity, α the thermal diffusivity, β the thermal expansion coefficient and g the gravitational acceleration. The governing equations are solved in a rectangular cuboid with aspect ratio $W/H = 8$ where the city pattern is placed in the middle of its bottom boundary. Periodic boundary conditions are applied in the horizontal directions. A no-slip, impermeable condition is applied at the bottom boundary while a free-slip is imposed at the top plates. A Dirichlet condition is imposed for the temperature in order to model the typical conditions of the urban heat island during summer nights. In particular, a uniform low temperature is imposed at the top boundary, $\theta(x, y, H, t) = \Theta_{atm}$. On the other hand, a non-homogenous high temperature distribution is imposed at the bottom, including buildings facades, in order to model the temperature contrast of urban environments with respect to the surrounding rural areas and to the atmosphere. The bottom boundary condition for temperature reads:

$$\theta(x, y, 0, t) = \begin{cases} \Theta_{city} e^{-r^2/(\sigma R)^2} & \text{for} \quad r \leq R \\ \Theta_{country} & \text{for} \quad r > R \end{cases} \tag{4.3}$$

where Θ_{city} and $\Theta_{country}$ are the reference temperature for the city and the country side and σ is a non-dimensional coefficient prescribing the temperature distribution within the urban environment. Since we are modelling the urban heat island in summer nights condition, the typical conditions for the reference temperatures are $\Theta_{atm} < \Theta_{country} < \Theta_{city}$ and a view of the imposed temperature distribution within the city pattern is reported in figure 4.1.

4.1.1 Relevant parameters in pure thermal convection conditions

In addition to the five statistical urban characteristics $(N, \lambda_p, \mathcal{AR}_p, \mathcal{AR}_z, \epsilon)$, the imposed boundary conditions introduce five additional fluid dynamic pa-

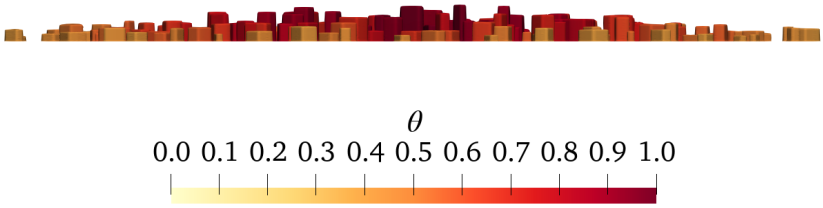

Figure 4.1: Lateral view of the city skyline coloured with the temperature distribution.

rameters that uniquely define the urban environment from a statistical point of view in the conditions of pure thermal convection. The first parameter is related to the atmospheric conditions and is the ratio between the average height of buildings $\langle \ell_z \rangle_b$ and the height of the domain H,

$$\Lambda_{atm} = \frac{\langle \ell_z \rangle_b}{H} \tag{4.4}$$

Considering the fact that a free-slip condition is imposed at the top, Λ_{atm} models the average ratio between the height of the city canopy and the height at which the thermal plume induced by the urban heat island stops rising, i.e., the thickness of the atmospheric layer that is dominated by the surface fluxes, the so-called surface layer. Three other relevant fluid dynamic parameters are introduced by the imposed thermal boundary conditions. Taking into account the temperature contrast between the countryside and the atmosphere, $\Delta\Theta_{country} = \Theta_{country} - \Theta_{atm}$ and the temperature difference between the city and surrounding rural areas, $\Delta\Theta_{city} = \Theta_{city} - \Theta_{country}$, the thermal boundary condition (4.3) can be rewritten with respect to the atmospheric temperature:

$$\theta(x, y, 0, t) = \begin{cases} \Theta_{atm}\left(1 + \dfrac{\Delta\Theta_{country}}{\Theta_{atm}} + \dfrac{\Delta\Theta_{city}}{\Theta_{atm}} F(r)\right) & \text{for} \quad r \leq R \\ \Theta_{atm}\left(1 + \dfrac{\Delta\Theta_{country}}{\Theta_{atm}}\right) & \text{for} \quad r > R \end{cases} \tag{4.5}$$

where

$$F(r) = e^{-r^2/(\sigma R)^2} \tag{4.6}$$

Hence, the intensity of the thermally-induced motions can be uniquely determined by two non-dimensional temperature contrasts, $\Delta\Theta_{country}/\Theta_{atm}$ and $\Delta\Theta_{city}/\Theta_{atm}$ together with a non-dimensional coefficient σ related to the specific urban configuration that prescribes the temperature distribution within the urban environment, from flat to peaked at the city centre.
In the present thesis, we consider $\Lambda_{atm} = 0.04$, $\Delta\Theta_{country}/\Theta_{atm} = 0.5$, $\Delta\Theta_{city}/\Theta_{atm} = 0.5$ and $\sigma = 1$. As an example, this values would lead to a city canopy where the average height of the buildings is in the range $\langle \ell_z \rangle_b = 8 \div 20m$ when the surface layer height is assumed to be in the range $H = 200 \div 500m$, for a thermal condition of the urban and rural areas of $\Theta_{country} = 30°C$ and $\Theta_{city} = 40°C$ when $\Theta_{atm} = 20°C$ is assumed as the temperature of the atmosphere.
The simulation is performed for a typical Prandtl number of air, Pr = 0.7, while the Rayleigh number has been set to $\mathrm{Ra} = 10^8$. For obvious computational cost reasons, this value is significantly smaller than the Rayleigh numbers that are commonly realized in real-world scenarios, $\mathrm{Ra} \sim 10^{17}$ for surface layers $H \sim 500m$ and maximum temperature differences between the city and the atmosphere $\Delta\Theta_{max} \sim 20°C$.
The global heat transfer attained in the system is evaluated by computing the Nusselt number $\overline{Nu} = (H/\Delta\Theta_{max})(\partial\overline{\Theta}/\partial z)|_w$ where $\Delta\Theta_{max}$ is the maximum temperature difference imposed between the top and bottom boundaries and $\overline{(\cdot)}$ denotes the average among the horizontal directions. The final value of the Nusselt number is $\overline{Nu} = 15$ and can be used to estimate the overall thickness of the thermal boundary layer $\overline{\delta_\theta} = H/(2\overline{Nu})$. The ratio between the average height of buildings and this last value introduces the last fluid dynamic parameter,

$$\Lambda_{bl} = \frac{\langle \ell_z \rangle_b}{\overline{\delta_\theta}} \tag{4.7}$$

that measures the effectiveness of the roughness introduced by the city canopy in interacting with the thermal structures. In the present work, we have $\Lambda_{bl} = 1.2$ thus highlighting that the roughness elements of the city exceed the thermal boundary layer in height. The fluid dynamic parameters that govern the flow solution are summarized in table 4.1.

Ra	Pr	$\overline{Nu}$	Λ_{atm}	Λ_{bl}
10^8	0.7	15	0.04	1.2

Table 4.1: Flow settings.

4.2 Numerical simulation

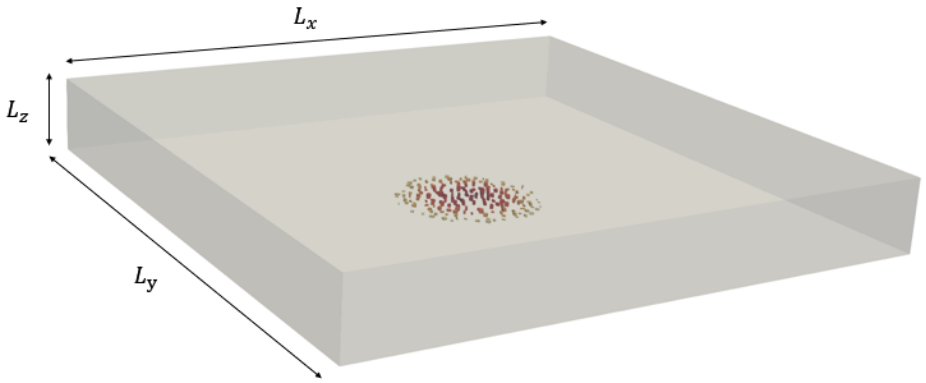

Figure 4.2: Schematic of the domain. The urban pattern is coloured with its temperature distribution.

The Boussinesq equations (4.1) are solved by using the open-source code CaNS 3. Time integration is carried out explicitly by using a three-step Runge-Kutta method and the time step is adapted to respect a condition on the Courant number, $CFL = 0.6$. The Poisson equation for the pressure field is efficiently computed using a direct FFT-based solver. To address the complex flow solution within the city canopy, an immersed boundary method (IBM) as discussed in chapter 3, has been exploited.

The dimensions of the domain are $(L_x, L_y, L_z) = (8R, 8R, R)$ where R is the radius of the city. The computational domain is discretized using a number of grid points equal to $(N_x, N_y, N_z) = (1600, 1600, 263)$ homogenously distributed in the horizontal directions. On the contrary, a hyperbolic tangent stretching is employed in the vertical direction to ensure adequate resolution at the top and bottom boundaries. The number of points used allows us to satisfy classical resolution requirements typical of Rayleigh-Beńard convection.

In particular, by following Shishkina et al. (2010), the minimum number of grid points within the thermal and dynamic boundary layer should be $N_{bl,\theta} \approx 0.35Ra^{0.15} = 5.54$ and $N_{bl,u} \approx 0.31Ra^{0.15} = 4.91$ respectively. The grid used employs $N_{bl,\theta} = 14$ grid points within the boundary layer, and $N_{bl,u} = 12$ within the velocity boundary layer, thus largely exceeding the resolution requirements. The simulation parameters are summarized in table 4.2 while figure 4.2 reports a schematic of the domain.

$L_x \times L_y \times L_z$	$N_x \times N_y \times N_z$	$\Delta\tau$	N_t
$8R \times 8R \times R$	$1600 \times 1600 \times 263$	2.6	55

Table 4.2: Parameters of the simulation. $\Delta\tau$ is the time interval between samples used for time average and is expressed in free-fall times H/U_{ff}, while N_t is the number of samples used.

4.3 Results

The analysis of the direct numerical simulations begins with the investigation of the flow structures arising under purely buoyancy-driven convection. Subsequently, statistical quantities of different orders are evaluated inside and above the urban canopy layer, allowing for a detailed assessment of the turbulence characteristics in both regions.

4.3.1 Statistical approach

The averages are computed by taking into account the statistical symmetries of the solution. Such symmetries can be better exploited by introducing a cylindrical coordinate system (r, φ, z) where r is the horizontal radial distance from the city centre, φ is the azimuthal direction and z is the vertical one. The corresponding velocity components are denoted as (u_r, u_φ, w). In this coordinate system, statistics are homogenous in both the azimuthal direction and time. Hence, statistics are computed by averaging in time, after the initial transient is washed out, and among the azimuthal direction. The resulting average operator will be denoted hereafter as $\langle\cdot\rangle$. Information about statistical samples gathered over time is reported in table 4.2. The classical Reynolds decomposition will be adopted and the corresponding average and fluctuating quantities will be denoted as $u_i = U_i + u_i'$ and $\theta = \Theta + \theta'$ where $U_i = \langle u_i \rangle$ and $\Theta = \langle \theta \rangle$ are the average fields, while u_i' and θ' are the fluctuating ones. In accordance with the statistical symmetries of the system, the only non-zero components of the mean velocity field are the radial and vertical ones, U_r and W, being the azimuthal direction statistically homogeneous, i.e. $U_\varphi = 0$. All statistics presented in the following sections will be reported dimensionless by using the average building height $\langle \ell_z \rangle_b$ for lengths and the free-fall velocity $U_{ff} = \sqrt{g\beta\Delta\Theta_{max}H}$ for velocities. On the other hand, temperature is reported as a temperature difference with respect to the atmospheric temperature Θ_{atm} and is made dimensionless by using the maximum temperature difference $\Delta\Theta_{max}$, i.e. $\theta \in [0:1]$.

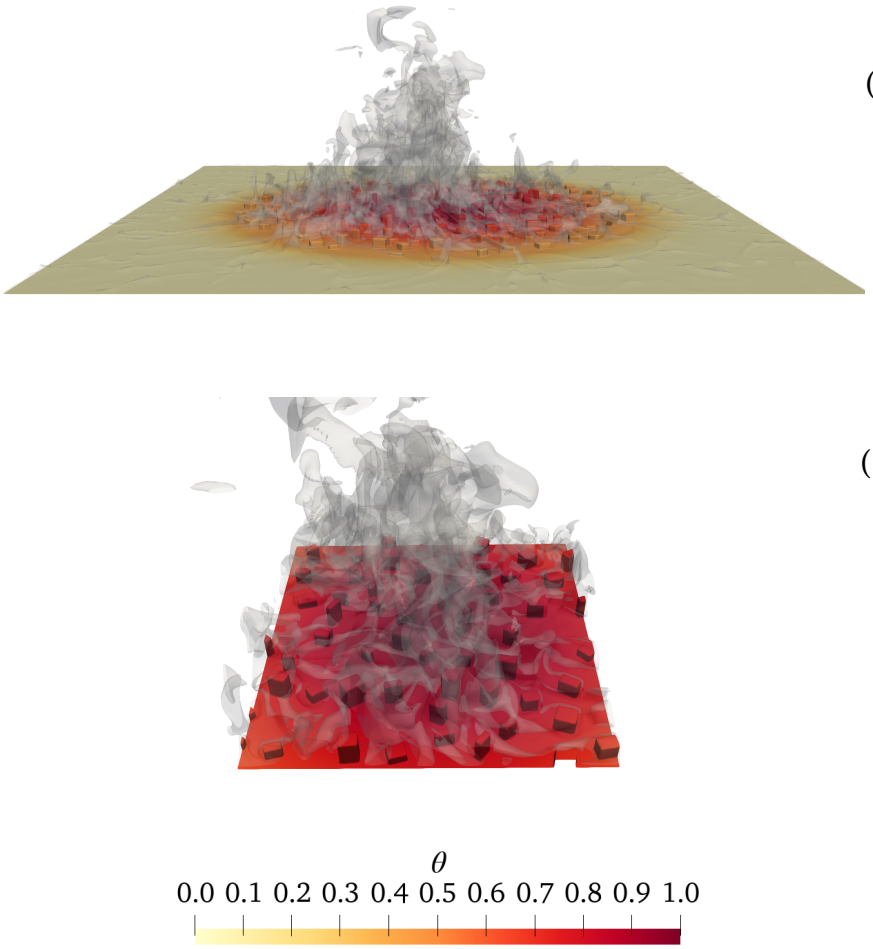

Figure 4.3: Direct numerical simulation of an entire urban environment under the conditions of pure thermal convection. (a) Instantaneous iso-surface of temperature $\theta = 0.45$ and iso-contours of normalized temperature at the ground. (b) Detailed view of the solution in the city centre.

4.3.2 Flow pattern

As shown in figure 4.3, the iso-surface of temperature $\theta = 0.45$ clearly highlights that the dominant flow feature of the urban heat island is given by a large convective structure of the order of the city size (Lu et al., 1997).

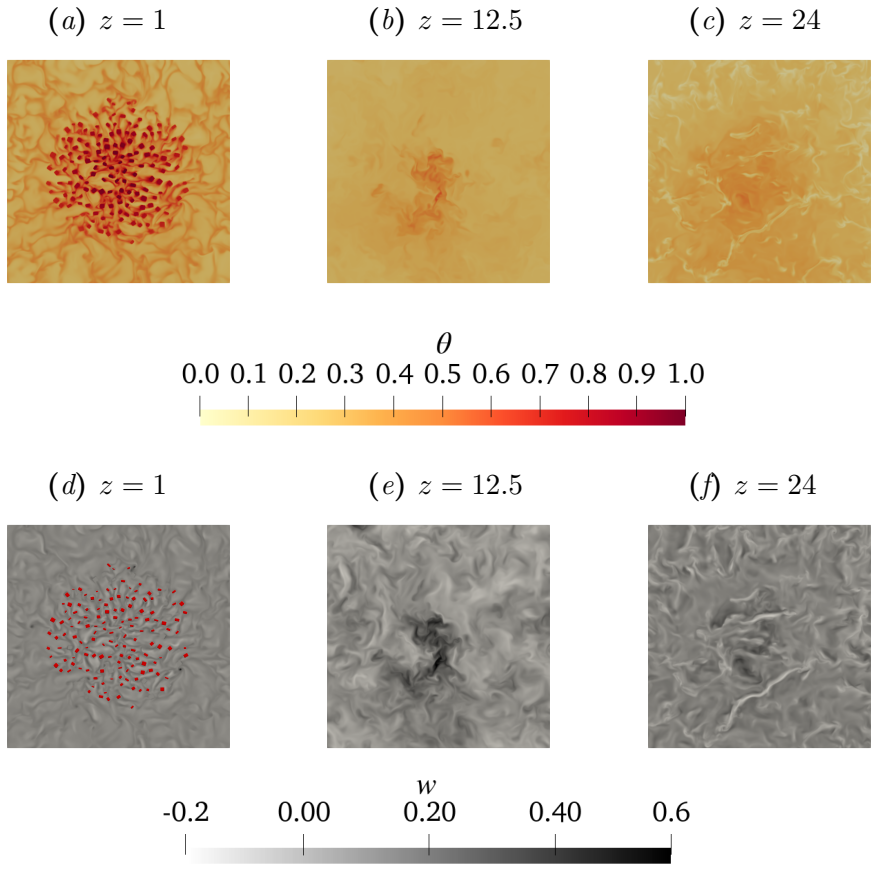

Figure 4.4: Direct numerical simulation of an entire urban environment under the conditions of pure thermal convection. (a-c) Instantaneous normalized temperature slices taken at different elevations. (d-e) Instantaneous slices of the dimensionless vertical velocity taken at different elevations. In (d) buildings trace at $z = 1$ are coloured in red.

It consists in a large thermal structure originating from the urban canopy that is characterized by a significant temperature contrast with respect to the background, see the top panels of figure 4.4. From a kinematic point of view, this large-scale structure is ascending from the urban canopy as a result of the buoyancy induced by its temperature difference between the surrounding atmosphere, as shown in the bottom panels of figure 4.4.

In particular, the large-scale thermal structure takes origin within the urban canopy, accelerates away from it, and, by mixing with the surrounding

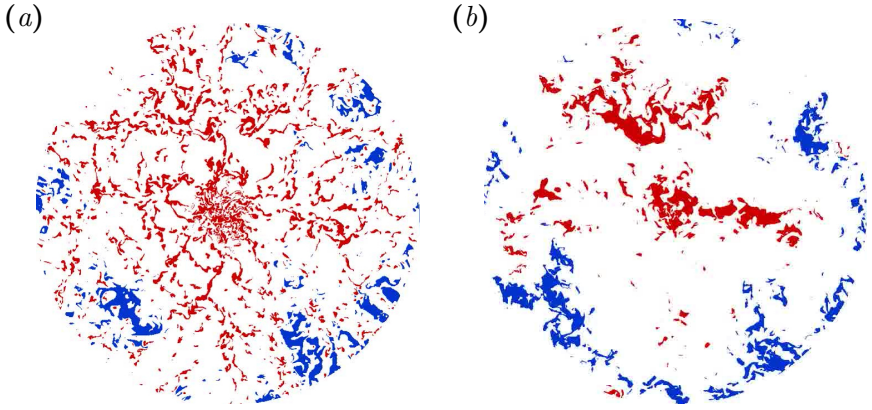

Figure 4.5: Visualization of thermal plumes in a horizontal slice just above the city canopy for (a) $z = 5$ and in the free atmosphere for (b) $z = 12.5$. The identification criterion (4.8) is used and red and blue colours are used to denote hot and cold plumes. The circular domain reported is for $r \in [0, 4]$.

colder atmosphere, eventually weakens and disappears at higher altitudes. Overall, the instantaneous temperature and velocity patterns suggest that the large-scale thermal structure is the principal carrier of heat in the flow system. A deeper inspection of the flow pattern within the urban canopy highlights that the large-scale thermal structure takes its origin from a complex arrangement of turbulent structures, thermal plumes. In order to discern them from the background fluctuations, a frequently used criterion that combine both temperature and heat flux conditions is considered (Xu et al., 2025). It consists in the identification of the thermal plume as the physical space where the fluctuation of temperature and heat flux exceed a given threshold,

$$|[\theta - \overline{\theta}]| > c\sqrt{\overline{(\theta - \overline{\theta})^2}} \qquad \sqrt{\mathrm{Ra}\,\mathrm{Pr}}\;|w(\theta - \overline{\theta})| > c(Nu - 1) \tag{4.8}$$

where the value of the constant used here is $c = 1.2$ as in Van Der Poel et al. (2015). As shown in figure 4.5(a), this procedure allows us to unveil that the urban environment is populated by a plethora of thermal plumes. While ascending, figure 4.5(b), these thermal plumes, interact each other and aggregate. Hence, the large-scale thermal structure is actually the result of a clustering of smaller thermal plumes originating within the city canopy. It is finally worth pointing out that the city canopy is populated most by hot thermal plumes, but despite being smaller in number, cold thermal plumes are also present, figure 4.5(a).

4.3.3 Scaling of ground quantities

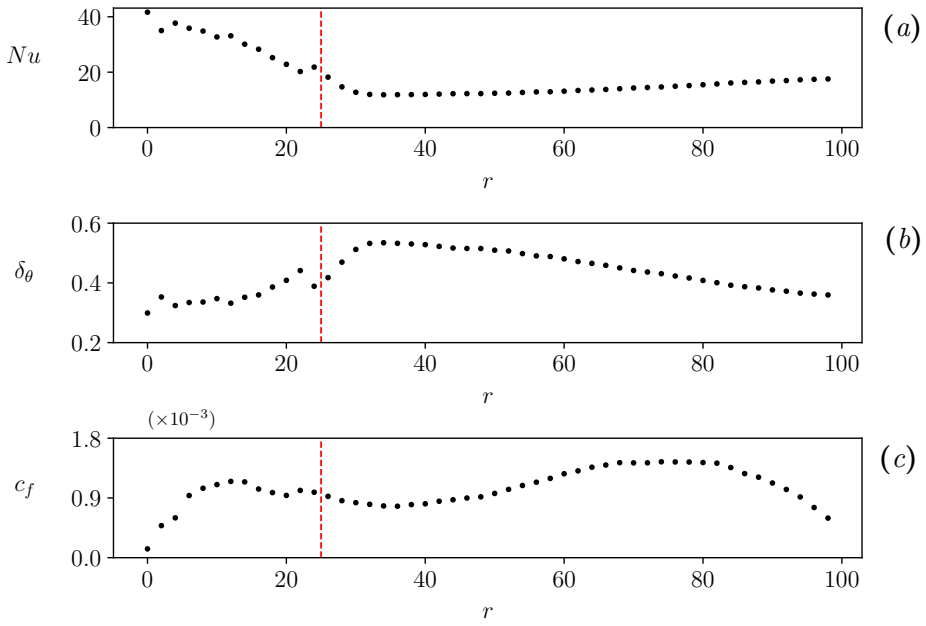

Figure 4.6: Radial scaling of ground quantities. (a) Heat transfer measured in terms of Nusselt number $Nu = (H/\Delta\Theta)(\partial\Theta/\partial z)|_w$. (b) Thermal boundary layer thickness estimated as $\delta_\theta = 1/(2\Lambda_{atm}Nu)$. (c) Momentum transfer measured in terms of friction coefficient $c_f = 2\tau_w/\rho U_{ff}^2$ where $\tau_w = \mu(\partial U_r/\partial z)|_w$. The vertical dashed red line indicates the location of the city boundary.

We start the statistical study of the flow solution by addressing first the behaviour of the fluxes of heat and momentum at the ground. The heat transfer is evaluated through the Nusselt number $Nu = (H/\Delta\Theta)(\partial\Theta/\partial z)|_w$ and is shown in figure 4.6(a). By moving radially from the outer regions toward the centre of the city, the Nusselt number exhibits first a slightly decreasing behaviour. By estimating the thermal boundary layer thickness as $\delta_\theta = 1/(2\Lambda_{atm}Nu)$, this decreasing behaviour of the Nusselt number corresponds to an increase of the thermal boundary layer thickness as shown in figure 4.6(b). By entering the city canopy for $r \leq 25$ ($r\langle\ell_z\rangle_b/R \leq 1$), the heat transfer changes its radial scaling and starts increasing up to reach its maximum at the city centre for $r = 0$. As a consequence, the thermal boundary layer thickness decreases and reaches its minimum value at the city centre. Overall, the flow solution suggests that heat transfer is enhanced

by the roughness elements of the urban environment, at least in the condition when they protrude from the thermal boundary layer, $\delta_\theta < 1$. Let us notice that the urban environment is also characterized by a non-uniform temperature difference with respect to the countryside. However, the effect of this non-uniform boundary condition is directly taken into account in the definition of the Nusselt number since $Nu = (H/\Delta\Theta)(\partial\Theta/\partial z)|_w$ with $\Delta\Theta = \Delta\Theta(r)$. Hence, the increase of heat transfer measured by entering the urban canopy can be reasonably ascribed to the roughness introduced by the city rather than its temperature difference. The analysis of the instantaneous flow pattern reported in the previous section has shown that a large-scale thermal structure is established above the city that, through buoyancy, induces a large-scale upward flux. For obvious mass conservation reasons, this net upward flux must be balanced by a net incoming radial flux from below, thus a boundary layer moving radially towards the city centre is generated. To study the momentum transfer released to the ground by the radially evolving boundary layer, the radial scaling of the friction coefficient $c_f = 2\tau_w/\rho U_{ff}^2$ where $\tau_w = \mu(\partial U_r/\partial z)|_w$, is shown in figure 4.6(c). From a maximum around $r = 78$ ($r\langle\ell_z\rangle_b/R = 3.12$), the friction coefficient decreases by moving radially towards the outer and inner regions. The large-scale thermal structure induced by the urban heat island is responsible for the generation of a large-scale circulation of toroidal shape whose radius of revolution $r = 78$ ($r\langle\ell_z\rangle_b/R = 3.12$), matches the outer peak of the friction coefficient. Hence, this is the distance from the city centre where the large-scale circulation induced by the urban heat island causes the maximum wind speed at ground level. By approaching the city canopy for $r < 35$ ($r\langle\ell_z\rangle_b/R < 1.4$), the radial scaling of the friction coefficient changes by exhibiting a slight increase in magnitude that is maintained up to $r = 12$ ($r\langle\ell_z\rangle_b/R = 0.48$). As better shown in the next section 4.3.5, this increase is related to the roughness of the urban environment rather than to an increase of the wind radial speed at the ground level. From this relative peak of momentum transfer, the friction coefficient starts to decrease again by moving towards the city centre for $r < 12$ ($r\langle\ell_z\rangle_b/R < 0.48$). In this central region, the large-scale thermal structure induced by the urban heat island, causes a lift up of the mean wind streamlines. Hence, the radial component of the wind weakens drastically by moving toward the city centre, leading to a reduction in the momentum transfer to the ground that, indeed, becomes null for $r = 0$.

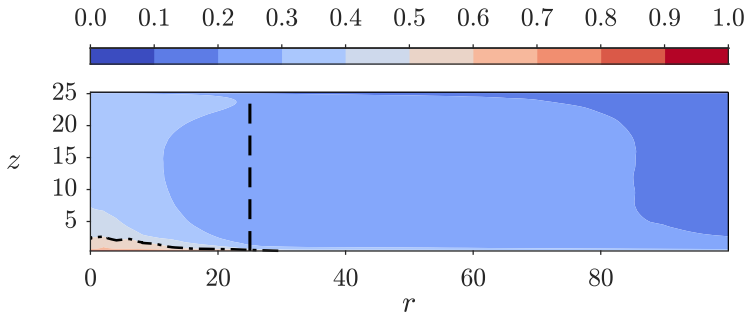

Figure 4.7: Contours of mean temperature $\Theta(r,z)/\Delta\Theta_{max}$. The vertical dashed line indicates the location of the city boundary while the dot dashed line is the contour line for $\Theta = 0.5$.

4.3.4 Mean temperature

As shown in figure 4.7, the contours of the mean temperature $\Theta(r,z)$ reveal the statistical shape and size of the large-scale thermal structure induced by the urban heat island observed in section 4.3.2 by means of instantaneous snapshots of the temperature field. By defining its border as the isoline of temperature $\Theta = 0.5$, the temperature of the countryside, a large-scale thermal plume is observed. Its size changes with the elevation. Starting from the ground where its size equals the city dimension, a minimum of the radius of the urban plume is reached at $z = 15$, i.e. 15 average heights of buildings above. At this elevation, the radius of the urban plume is almost half the city radius, $r = 12$ ($r\langle\ell_z\rangle_b/R = 0.48$).

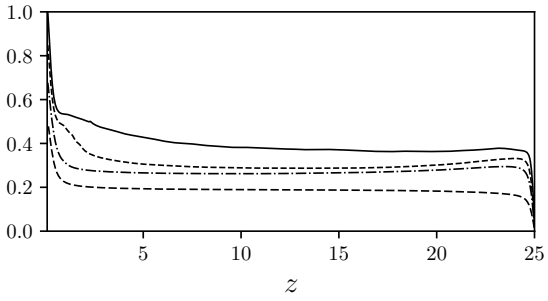

Figure 4.8: Vertical profiles of mean temperature $\Theta(z)/\Delta\Theta_{max}$ at different radial locations, $r = 0$ (solid line), $r = 15$ (dashed line), $r = 25$ (dash-dot line) and $r = 100$ (long-dash line).

By moving in the vertical direction, the thermal plume performs mixing with the colder atmosphere. Hence, a mean temperature decay in the vertical and radial directions is observed in figure 4.7. A more quantitative view of the phenomenon is provided in figure 4.8 where the vertical profiles of mean temperature at different radial locations are shown. By considering first the temperature profile above the city centre for $r = 0$ (solid line), it is possible to observe that a sharp jump of temperature is occurring within the urban roughness. In particular, the temperature is found to be almost halved by moving from the ground to the average height of buildings, $\Theta(0,0) = 1$ and $\Theta(0,1) = 0.54$. Hence, a temperature close to the one imposed for the countryside ($\Theta = 0.5$) is recovered just above the city canopy. This thin layer of steep temperature gradient is hereafter referred to as the thermal boundary layer. For $z > 1$, the temperature decay above the city centre weakens and for $z > 10$ becomes essentially flat around the value $\Theta = 0.4$. Hence, we can distinguish two additional regions above the thermal boundary layer. An intermediate buffer layer for $1 < z < 10$ where the mean temperature profile gradually decreases followed by an outer layer for $z > 10$ where the mean temperature profile is almost flat. Contrary to the thermal boundary layer, these two layers are dominated by turbulence mixing whose action is to homogenize the mean temperature distribution, as it will be shown in the next section 4.3.6.

Moving to intermediate radial locations at $r = 15$ (dashed line), the intermediate buffer layer gradually shrinks up to disappear above the edge of the city at $r = 25$ (dash-dot line), see again figure 4.8. Hence, the intermediate buffer layer of mean temperature decay appears to be a specific flow feature of the urban thermal plume. In fact, the mean temperature profile for $r \geq 25$ has a simple two-layer structure typical of natural convection setups (Chillà and Schumacher, 2012), i.e. a thermal boundary layer where a steep temperature gradient occurs, followed by an outer region where the temperature profile is almost homogeneous.

4.3.5 Mean velocity

As shown in figure 4.9(a), the streamlines of the mean velocity field reveal the presence of a large-scale circulation (LSC) generated by the large-scale urban plume analysed in the previous section 4.3.4. Specifically, an upward flow originates from the rough and hot urban environment that is fed from below by a radial boundary layer moving towards the city centre. As better shown in figure 4.9(b) and 4.9(a), the urban updraft accelerates first driven by buoyancy, see the contours of temperature overlaid to figure 4.9(a), and

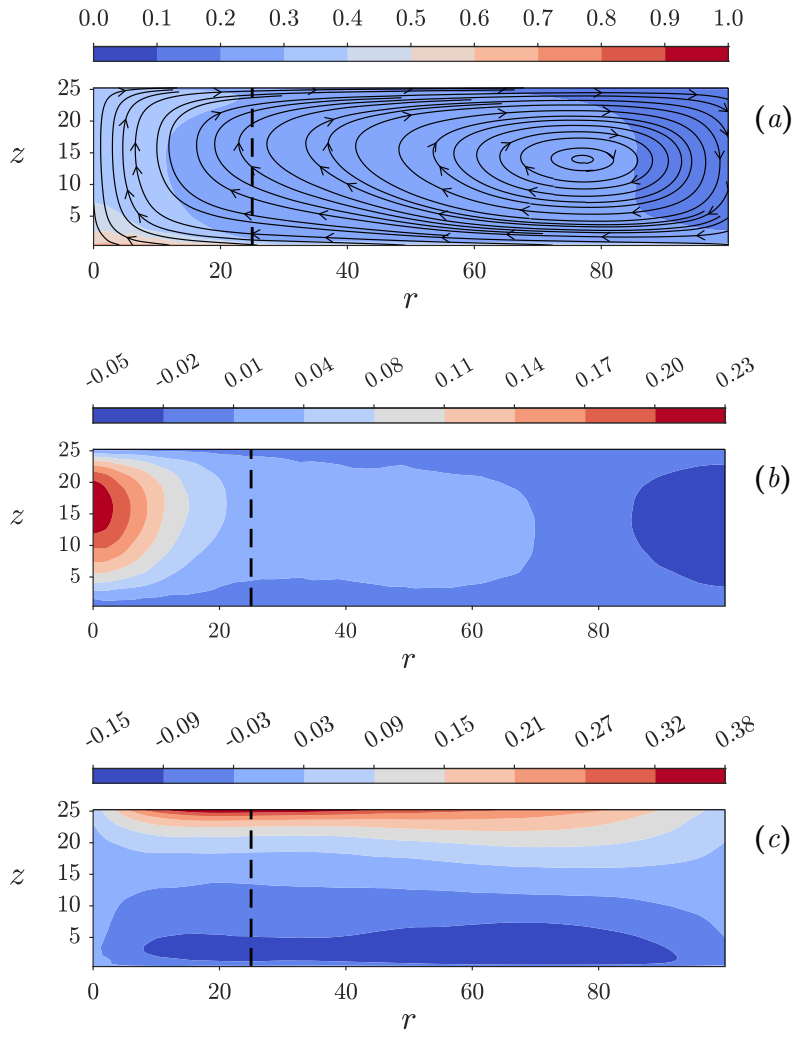

Figure 4.9: (a) Streamlines of the dimensionless mean velocity field $(U_r, W)(r, z)$ superimposed to the contours of mean temperature $\Theta(r, z)/\Delta\Theta_{max}$. (b) Contours of mean vertical velocity $W(r, z)/U_{ff}$. (c) Contours of mean radial velocity $U_r(r, z)/U_{ff}$. The vertical dashed line indicates the location of the city boundary.

reaches it maximum speed above the city centre at the elevation $z = 17$,

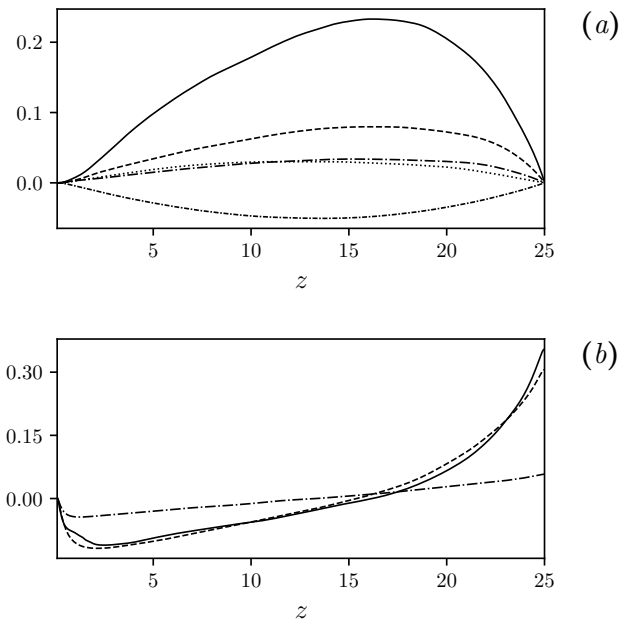

Figure 4.10: Vertical profiles of (a) mean vertical velocity $W(z)/U_{ff}$ and (b) mean radial velocity $U_r(z)/U_{ff}$ at different radial positions. For $W(z)/U_{ff}$, $r = 0$ (solid line), $r = 15$ (dashed line), $r = 25$ (dash-dot line), $r = 50$ (dash–dot–dot line) and $r = 100$ (long-dash line). For $U_r(z)/U_{ff}$, $r = 15$ (solid line), $r = 25$ (dashed line) and $r = 100$ (dot-dash line).

i.e. seventeen times the average height of buildings. Then, for $z > 17$ the urban updraft decelerates and starts to diverge in the radial directions. This velocity reduction of the urban updraft is mainly due by the impermeability condition imposed at the top boundary, $z = 25$, and by the lowering of buoyancy given by the mixing with the surrounding colder atmosphere. Overall, the ascending flow involves regions that significantly exceed the city area. In particular, we measure a positive mean vertical velocity for $r < 77$. Indeed, as better shown by the streamlines in figure 4.9(a), the large-scale circulation induced by the urban heat island has a center of rotation located at $(r, z) = (77, 15)$. Accordingly, a downdraft of cold fluid is found only for country regions far from the city for $r > 77$, i.e. almost three city radius from the center $r\langle \ell_z \rangle_b / R = 3.08$. Because of mass conservation and of the toroidal shape of the large-scale circulation induced by the urban heat island, the downdraft speed in the countryside is weak compared to

the updraft above the city. In particular, we measure $W_{max} = 0.23$ and $W_{min} = -0.05$.

As already pointed out, the large-scale circulation induced by the urban heat island is characterized by a radially incoming boundary layer. This boundary layer is fed by the downdraft of the urban LSC and, hence, plays the relevant role of replenishing the urban environment of colder air but also of transporting all the pollution and contaminant produced within the city towards its center where it is accumulated. The contours of mean radial velocity are reported in figure 4.9(c) where it is possible to observe that the radially evolving boundary layer is almost homogeneous within the regions $8 < r < 90$. To better quantify its scaling, the vertical profiles of mean radial velocity evaluated at different radial locations are reported in figure 4.10. All the profiles exhibit a peak velocity close to the ground whose vertical location δ_ν can be used as a measure of the height of the boundary layer. Starting from the countryside at $r = 50$, namely two city radius far from the city centre $r\langle\ell_z\rangle_b/R = 2$, we measure a boundary-layer height $\delta_\nu = 2.5$ and a peak velocity $U_{r,peak} = -0.12$. By moving towards the city center, the height of the radial boundary layer and its peak velocity decrease. In particular, we measure $\delta_\nu = 2$ and $U_{r,peak} = -0.09$, at the edge of the city canopy for $r = 25(r\langle\ell_z\rangle_b/R = 1)$ and $\delta_\nu = 1$ and $U_{r,peak} = -0.03$ at an intermediate location within the city canopy for $r = 15(r\langle\ell_z\rangle_b/R = 0.6)$. Hence, the urban environment is flushed by a radial boundary layer whose thickness is of the order of the average height of buildings $\langle\ell_z\rangle_b$ and whose peak intensity is 3% the free-fall velocity induced by the urban heat island at city edge and decreases to zero moving towards the city centre. Above the boundary layer height, all the profiles of figure 4.10 show that the intensity of the average radial velocity decreases almost linearly with elevation. This linear scaling is preserved up to the height of inversion of the radial velocity, i.e. the vertical location where $U_{r,peak} = 0$. As shown in figure 4.10(c) this elevation is almost constant among different radial position ranging from $z = 15$ in the very external regions to $z = 17$ above the city environment.

4.3.6 Turbulent mixing

As already noticed in the previous sections, turbulence plays a relevant role in defining the mean temperature and velocity patterns, since the action of turbulence is to perform mixing and, hence, to increase the transport of both heat and momentum. The intensity of turbulence is analysed here by considering the pattern taken by the standard deviation of both the tem-

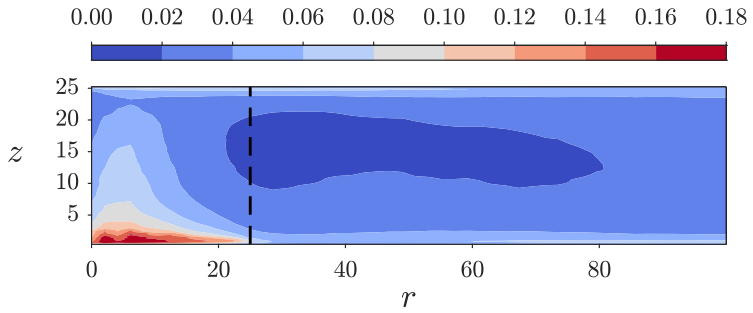

Figure 4.11: Contours of the standard deviation of temperature fluctuations $\sqrt{\langle\theta'^2\rangle}(r,z)/\Delta\Theta_{max}$. The vertical dashed line indicates the location of the city boundary.

perature and velocity fields. As shown in figure 4.11, the standard deviation the temperature field highlights that the urban thermal plume is the most active region. In particular, the most intense temperature fluctuations are found to occur within the city environment for $r \leq 25 (r\langle\ell_z\rangle_b/R \leq 1)$. Here, the intensity of the fluctuations is of the order of 20% the maximum temperature difference within the system $\Delta\Theta_{max}$ and the peak intensity is reached just below the average height of buildings for $z \approx 0.8$. From this peak activity region, the intensity of the temperature fluctuations gradually decays by moving radially towards the countryside and by increasing the elevation. In particular, outside the urban thermal plume the intensity of the temperature fluctuations is very low of the order of 4% the maximum temperature difference $\Delta\Theta_{max}$.

With respect to the velocity fluctuations, we found that the two horizontal velocity components share almost the same behaviour, as shown in figure 4.12(a) and (b). In particular, the radial and azimuthal velocity fluctuations are weak in the bulk of the flow, less than 10% the free-fall velocity U_{ff}, and become more intense, within the radially evolving boundary layer at the bottmo and at the top boundary of the flow system. These peaks at $z = 25$ are essentially induced by the imposed impermeability condition, so that the vertical velocity fluctuations within the city updraft for $r \leq 25$ $(r\langle\ell_z\rangle_b/R \leq 1)$ and country downdraft for $r \geq 77$ $(r\langle\ell_z\rangle_b/R \geq 3.08)$ are reoriented in the horizontal directions through pressure-strain phenomena whose intensity is given by $2\langle p'(\partial u'_z/\partial z)\rangle$. At the ground boundary layer, the intensity of the horizontal velocity fluctuations decreases by moving

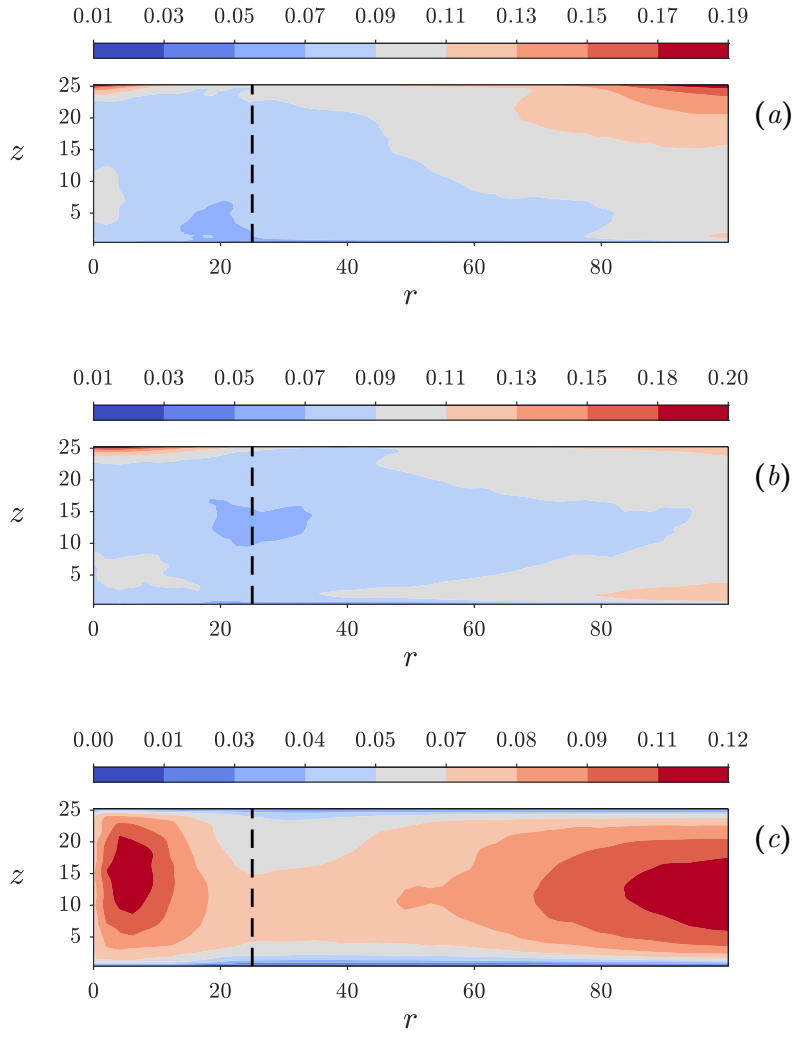

Figure 4.12: Contours of the standard deviation of (a) radial velocity $\sqrt{\langle u_r'^2 \rangle}(r,z)/U_{ff}$, (b) tangential velocity $\sqrt{\langle u_\varphi'^2 \rangle}(r,z)/U_{ff}$ and (c) vertical velocity $\sqrt{\langle w'^2 \rangle}(r,z)/U_{ff}$. The vertical dashed line indicates the location of the city boundary.

radially towards the city center. As a result, the horizontal velocity fluctuations within the radial locations of the city for $r \leq 25$ ($r\langle \ell_z \rangle_b / R \leq 1$),

are weak within the city canopy for $z \leq 2.5$ and more intense above. In contrast to the horizontal components, the vertical velocity fluctuations exhibit a different pattern as shown in figure 4.12(c). Two distinct intense activity regions are found that peak at intermediate elevations, one located within the updraft and the other within the downdraft of the urban thermal plume. The mean flow topology and the distribution of temperature fluctuations observed at the intermediate elevations of the urban updraft suggest that the peak activity of the vertical velocity fluctuations above the urban environment for $r \leq 25$ ($r\langle \ell_z \rangle_b / R \leq 1$) is essentially induced by sourcing mechanisms related to both mean shear and buoyancy whose intensity is given by $\langle w'\theta' \rangle - 2\langle u'_r w' \rangle (\partial W / \partial r)$.

4.3.7 Urban environment

In order to analyse the non-homogeneous effects of the urban configuration on the heat transfer, we consider the local Nusselt number as

$$Nu = -\frac{H}{\Delta\Theta_{max}} \frac{\partial \widetilde{\theta}}{\partial x_j} \hat{n}_j \tag{4.9}$$

where $\hat{\boldsymbol{n}}$ is the unit vector normal to the city boundary and $\widetilde{\cdot}$ denotes the time average operator. The spatial distribution of the local Nusselt number, shown in figure 4.13(a–b), provides further insight. The urban canopy configuration clearly emerges as the most active region in terms of heat exchange at the lower boundary. The highest values are observed on the rooftops, confirming that a substantial portion of the heat transfer occurs there. This effect is particularly pronounced toward the centre of the roughness pattern, consistently with previous observations. In fact, here is located the maximum of temperature fluctuations and the origin of the upward branch of the large-scale circulation (LSC). Another noticeable feature is the shading effect produced by the neighbouring buildings. In combination with the incoming flow, this effect is more evident for buildings located near the edge of the city. Walls facing outward, directly exposed to the radially evolving boundary layer, exhibit higher local Nusselt values compared to those facing the interior of the canopy. Within the urban core, shading effects and reduced average velocity, limit local convective transport, thereby decreasing heat transfer to walls. The plan aspect ratio of the buildings does not appear to significantly affect the overall distribution of the local Nusselt number (4.9).

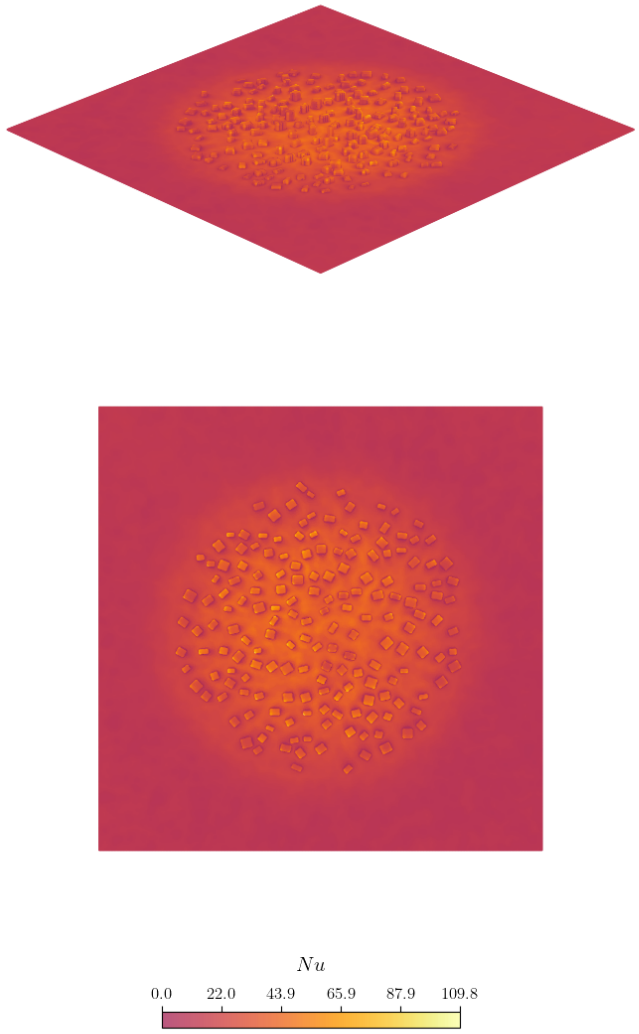

Figure 4.13: Time averaged Nusselt number among the the urban configuration.

Considering the radial distribution of temperature and velocity at $z = 1$, figure 4.14 presents both the mean and root mean square profiles of the tem-

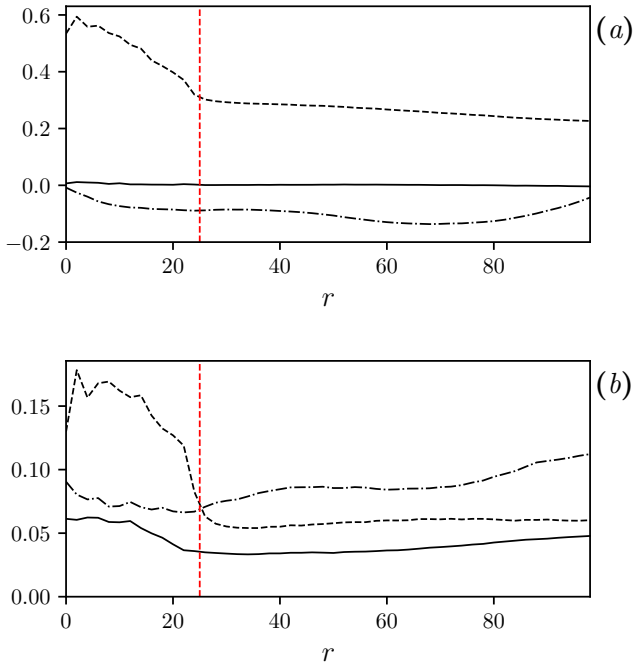

Figure 4.14: Radial profiles for $\Theta(r)/\Delta\Theta_{max}$, $W(r)/U_{ff}$ and $U_r(r)/U_{ff}$ at $z = 1$. Panel (a) shows $W(r)/U_{ff}$ (solid line), $\Theta(r)/\Delta\Theta_{max}$ (dashed line) and $U_r(r)/U_{ff}$ (dashed-dotted line). Panel (b) presents $\sqrt{\langle w'^2(r)\rangle}/U_{ff}$ (r) (solid line), $\sqrt{\langle \theta'^2(r)\rangle}/\Delta\Theta_{max}$ (dashed lined) and $\sqrt{\langle u_r'^2(r)\rangle}/U_{ff}$ (dashed-dot line). The red vertical dashed line indicates the location of the city boundary.

perature field and velocity components. Focusing first on the mean quantities, figure 4.14(a), the temperature exhibits a decreasing trend along the radial direction, with a more pronounced gradient within the urban region. This behaviour directly reflects the imposed thermal boundary condition. At the same height, the mean vertical velocity remains nearly null along the radius being slightly positive in the central area, consistent with the upward branch of the large-scale circulation. In contrast, the radial velocity component is negative throughout the entire domain, indicating the inward motion of colder fluid from the periphery of the domain toward the urban core. Within the canopy region, however, the magnitude of the radial velocity progressively decreases $r \leq 10$ ($r\langle \ell_z \rangle_b / R \leq 0.4$), revealing a weakening of the inward flow. This attenuation of radial momentum reflects the combined

effect of surface roughness and buoyancy: as the flow approaches the city centre, feeds the upward transport associated with the large-scale circulation. Moving to the root mean square reported in figure 4.14(b), the trend of both the vertical velocity and the temperature fluctuations, exhibits a clear reduction within the roughness region, while beyond the urban canopy, these quantities tend to approach an approximately constant level. In contrast, the root mean square of the radial velocity increases in magnitude, especially for $r \leq 75$ ($r\langle \ell_z \rangle_b / R \leq 3$), in the country downdraft area, confirming the trends previously identified in paragraph 4.3.6.

4.3.8 Heat transfer

Under the Boussinesq approximation, the equation governing the average heat transfer $\rho c_p \Theta$, where c_p is the heat capacity, can be reduced to the equation for the mean temperature Θ. For this reason, in the present section we will refer to mean temperature equation to address the mechanisms of heat transfer. Due to the statistical symmetries of the present flow configuration, the transport equation of mean temperature Θ can be written as follows:

$$\frac{1}{r}\frac{\partial}{\partial r} r \left(\langle \theta' u_r' \rangle + \Theta U_r - \frac{1}{\sqrt{\mathrm{Ra}\,\mathrm{Pr}}} \frac{\partial \Theta}{\partial r} \right) + \frac{\partial}{\partial z} \left(\langle \theta' w' \rangle + \Theta W - \frac{1}{\sqrt{\mathrm{Ra}\,\mathrm{Pr}}} \frac{\partial \Theta}{\partial z} \right) = 0 \tag{4.10}$$

By rewriting the heat transfer equation (4.10) in a conservative form

$$\nabla \cdot \boldsymbol{\phi} = 0 \tag{4.11}$$

it is possible to highlight that heat is transferred among different radial locations and elevations by a two-dimensional flux $\boldsymbol{\phi} = (\phi_r, \phi_z)$ defined as

$$\begin{aligned} \phi_r &= \langle \theta' u_r' \rangle + \Theta U_r - \frac{1}{\sqrt{\mathrm{Ra}\,\mathrm{Pr}}} \frac{\partial \Theta}{\partial r} \\ \phi_z &= \langle \theta' w' \rangle + \Theta W - \frac{1}{\sqrt{\mathrm{Ra}\,\mathrm{Pr}}} \frac{\partial \Theta}{\partial z} \end{aligned} \tag{4.12}$$

where it is possible to recognize that fluxes of heat are sustained by turbulence mixing phenomena, advection by the mean flow and diffusion, respectively the first, second and third term of the right-hand sides of (4.12). Obviously, no source or sink of heat are present within the flow system. Indeed, heat is provided at the boundary of the domain by the imposed

boundary conditions on temperature. In particular, by considering the volume integral over the entire flow domain of equation (4.10) and the imposed lateral periodic boundary conditions, we can write the following balance

$$q_g = q_t \tag{4.13}$$

where

$$q_g = \int_{\partial\Omega_b} -\frac{1}{\sqrt{RaPr}}\frac{\partial\Theta}{\partial z}\, dS \tag{4.14}$$

is the heat fluxes entering the system from the bottom boundary $\partial\Omega_b$, the ground surface, and

$$q_t = \int_{\partial\Omega_t} -\frac{1}{\sqrt{RaPr}}\frac{\partial\Theta}{\partial z}\, dS \tag{4.15}$$

is the heat flux exiting the system from the top boundary $\partial\Omega_t$, the atmospheric surface layer. Hence, the field of fluxes $\boldsymbol{\phi}$ have the overall role to perform a net transfer of heat from the ground to the atmosphere with no net effects from the lateral sides.

Figure 4.15 (a) shows the mean temperature contour superimposed with the lines of the total heat fluxes (4.12) whereas panel (b) isolates the turbulent contribution only. The total heat flux exhibits a predominantly inward radial motion from the peripheral regions of the domain, for $r \leq 80$ ($r\langle\ell_z\rangle_b/R \leq 3.2$), towards the urban core, where it is subsequently advected upward along the ascending branch of the large-scale circulation. The spatial organisation of the heat-flux vectors mirrors the structure of the large-scale circulation, clearly identifying the regions where the radial component of the total heat flux exceeds the vertical one and, conversely, where vertical transport becomes dominant.

In contrast, the turbulent heat flux exhibits an opposite radial behaviour. The vector field shown in figure 4.15(b) reveals a predominantly outward oriented trend with a marked vertical component, particularly pronounced for $r \leq 60$ ($r\langle\ell_z\rangle_b/R \leq 2.4$). This tendency becomes even more evident within the region directly influenced by the urban canopy ($r \leq 25$, $r\langle\ell_z\rangle_b/R \leq 1$), where the largest temperature fluctuations are observed. As might be expected, this behaviour reflects the intrinsic role of turbulent fluxes to enhance mixing, to homogenize different flow regions by increasing heat and momentum transport from warmer to colder area, beneficial for urban heat island mitigation.

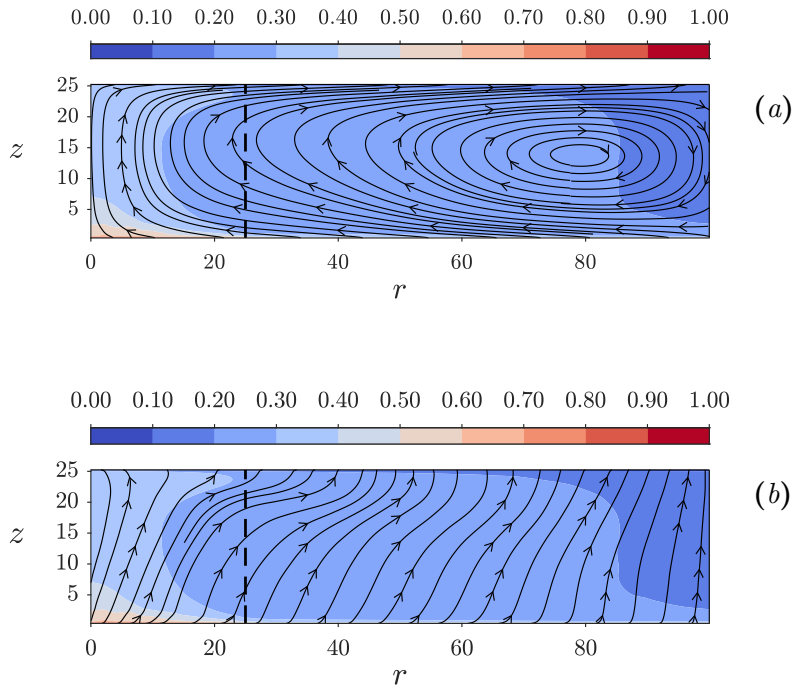

Figure 4.15: Streamlines of total heat flux superimposed to the contour of mean temperature $\Theta(r,z)/\Delta\Theta_{max}$ in panel (a). Streamlines of turbulent heat flux superimposed to the contour of mean temperature $\Theta(r,z)/\Delta\Theta_{max}$ in panel (b). The vertical dashed line indicates the location of the city boundary.

Chapter 5

Best practice for LES in urban environments

This chapter investigates coarse-grained simulations of paradigmatic urban patterns, where grid resolution and subgrid-scale modelling strategies are varied and systematically assessed against the reference DNS dataset. The objective is to establish quantitative guidelines for the reliable application of LES in paradigmatic urban configurations, thus producing a best practice. While DNS provides a detailed and physically consistent description of the flow, its computational cost prevents its application to larger or more realistic domains. Coarse-grained approaches aim instead to resolve the dominant flow structures while modelling the contribution of unresolved turbulent motions through appropriate closures. In this framework, Large-Eddy Simulations (LES) are performed using OpenFOAM and evaluated in terms of their ability to reproduce the main dynamical and thermal features observed in the DNS. In particular, two modelling strategies are examined: an implicit LES approach, and an explicit LES formulation based on the Wall Adapting Local Eddy-viscosity, WALE model. Some of the results of this chapter has been obtained within the master thesis work of Venturelli (2025) which I have supervised during my PhD.

5.1 Computational setup

In order to reproduce the reference configuration described in chapter 4, the physical dimensions of the computational domain are preserved. The domain consists of a rectangular box containing 176 building elements arranged as an urban roughness pattern at the centre of the bottom wall. The main modification in the coarse-grained simulations concerns the spatial resolution, as summarised in table 5.1. The computational grid is generated through a two-step procedure: a base mesh is first constructed using Gmsh (Gmsh Reference Manual, 2026), and subsequently refined with the *SnappyHexMesh* utility of OpenFOAM to enhance the resolution in the vicinity

of the urban canopy. The Gmsh base mesh is designed to provide increased resolution within the urban region while preserving acceptable cell aspect ratios and orthogonality, thereby ensuring robustness of the subsequent refinement stage. As in the DNS configuration, a vertically graded mesh is adopted to limit the total number of cells while maintaining adequate near-wall resolution. Above the height $0.2R = 0.2H = 5\langle \ell_z \rangle_b$, the grid remains structured, with a horizontal spacing approximately three times larger than in the DNS case, $\Delta_{x,y}^{LES} \sim 3\Delta_{x,y}^{DNS}$. As reported in table 5.1, the two coarse-grained simulations employ different refinement levels around the buildings. In particular, the WALE LES requires a finer near-wall resolution, consistent with the more stringent resolution demands of the explicit subgrid-scale model.

Case	$L_x \times L_y \times L_z$	$N_x \times N_y \times N_z$	Refinement	Total cells
DNS	$8R \times 8R \times 1R$	$1600 \times 1600 \times 263$	–	$6.7 \cdot 10^8$
ILES	$8R \times 8R \times 1R$	$550 \times 550 \times 145$	1*	$4.4 \cdot 10^7$
WALE LES	$8R \times 8R \times 1R$	$550 \times 550 \times 145$	2*	$4.5 \cdot 10^7$

Table 5.1: Comparison of meshes between three cases. The third column for the ILES and WALE LES case corresponds to the number of volumes used for the base mesh in Gmsh. The asterisk (*) in the Refinement column indicates a uniform surface refinement level of 1 for the city region.

As in the reference DNS configuration, a no-slip condition is imposed at the bottom wall, while a free-slip condition is applied at the top boundary for the velocity field. A fixed temperature is prescribed at both the bottom and top plates in order to reproduce nocturnal urban heat island conditions, see chapter 4. Periodic boundary conditions are enforced along the lateral boundaries for both velocity and temperature. All fluid properties adopted in the simulations are reported in table 5.2. Time integration is performed using a first-order implicit backward scheme, while the convective terms are discretised through a combination of upwind and bounded schemes to ensure numerical stability. A variable time step is employed, constrained by a maximum Courant number equal to 1. To enhance numerical robustness and accuracy, non-orthogonal corrections and suitable under-relaxation factors are applied. The simulations are carried out using the *buoyantBoussinesqPimpleFoam* solver, which solves the filtered incompressible Navier–Stokes equations under the Boussinesq approximation, see chapter 3.

Case	Pr	Pr_t	Ra
ILES	0.7	–	10^8
WALE LES	0.7	0.9	10^8

Table 5.2: Fluid properties for the coarse grained simulations.

5.2 Validation

Case	Nu	Relative error (%)	Cost saving ratio	Normalized cost (%)
DNS	15	–	1	100
ILES	18.09	20.6	6	0.35
WALE LES	16.62	10.8	4	0.51

Table 5.3: Validation of LES approaches against DNS in terms of heat transfer prediction and computational efficiency. The relative error is computed with respect to DNS. The cost saving ratio represents the measured computational speed-up based on CPU hours per unit time simulated, while the normalized cost corresponds to the theoretical cost relative to DNS estimated from the scaling $N_{cells}/\Delta t$.

The statistical assessment of the different modelling strategies is organised into two main parts. The analysis first focuses on the flow dynamics in the colder atmospheric layer above the canopy, for $z \in [0.2H, H]$ corresponding to $[5\langle\ell_z\rangle_b,\ 25\langle\ell_z\rangle_b]$, and subsequently addresses the effects induced by the urban configuration within the canopy region, $z \in [0, 5\langle\ell_z\rangle_b]$. Consistently with the DNS analysis, all quantities are expressed in dimensionless form using the average building height $\langle\ell_z\rangle_b$ as the reference length scale and the free-fall velocity $U_{ff} = \sqrt{g\beta\Delta\Theta_{max}H}$ as the velocity scale. Statistical averages are computed by exploiting the symmetries of the flow field and are reported in the cylindrical coordinate system (r, φ, z).
As reported in Table 5.3, the WALE LES provides a more accurate prediction of the heat transfer, with a relative error of 10.8% compared to DNS. Conversely, the ILES exhibits a larger deviation of 20.6% but achieves a higher measured computational speed-up. Based on CPU hours per unit time simulated, ILES is approximately six times faster than DNS, whereas WALE LES provides a speed-up of about four. A theoretical estimate based

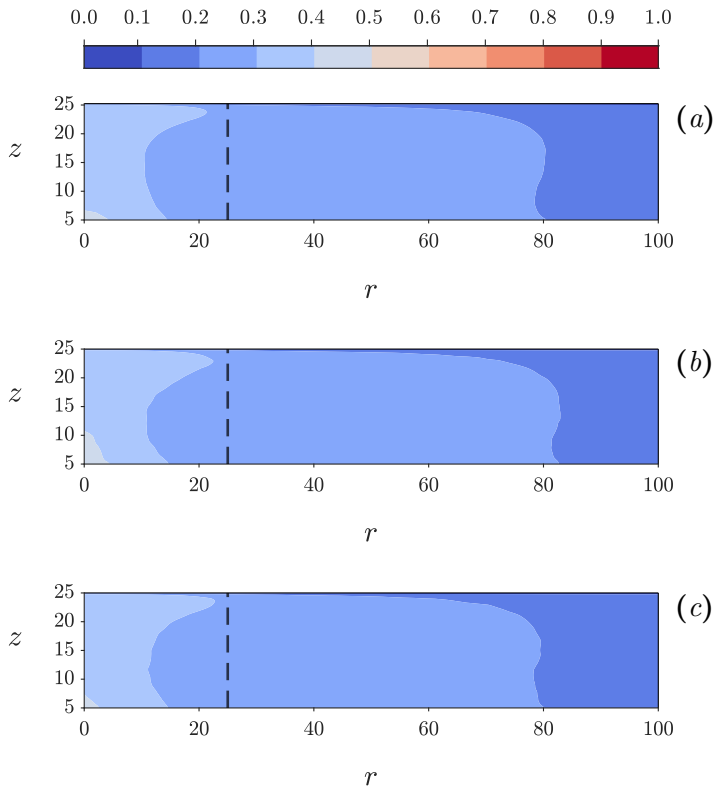

Figure 5.1: Contours of mean temperature $\Theta(r, z)/\Delta\Theta_{max}$ for the three simulations: (a) DNS, (b) ILES, and (c) WALE LES. The vertical dashed line indicates the location of the city boundary.

on the ideal scaling $N_{cells}/\Delta t$ would instead predict a speed-up of the order of 10^2. The discrepancy between the theoretical and measured values arises from implementation factors, including solver efficiency, parallelization strategy, and numerical discretization, see chapter 3.

5.2.1 Free flow statistics

As shown in figure 5.1, the mean temperature contours $\Theta(r, z)$ obtained from the coarse-grained simulations (b–c) reproduce the large-scale thermal structure developing above the urban canopy, consistently with the DNS reference solution (a). In all cases, a monotonic decay of temperature is

observed in both the radial and vertical directions.

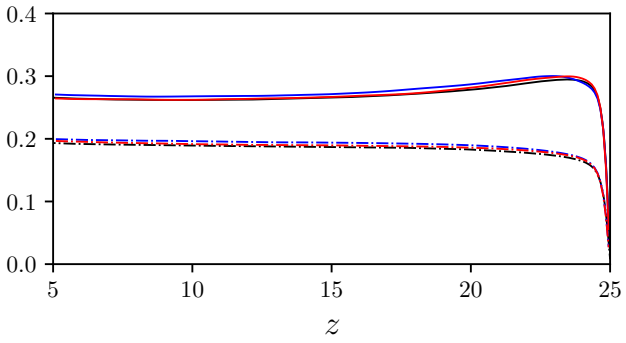

Figure 5.2: Vertical profiles of the mean temperature $\Theta(z)/\Delta\Theta_{max}$ at two radial locations: $r = 25$ (solid lines) and $r = 100$ (dash–dot lines). DNS (black), WALE LES (red), and ILES (blue).

The WALE LES (c) exhibits closer agreement with the DNS in terms of the overall shape and spatial extent of the thermal plume. Minor discrepancies are confined to the city centre at $r = 5$ ($r\langle\ell_z\rangle_b/R = 0.2$), where the warm core appears slightly narrower than in the reference solution. By contrast, the ILES configuration (b) shows more pronounced deviations. In the central urban region ($r = 5$), the warm core is vertically elongated compared to both DNS and WALE LES, with the isotherms corresponding to $\Theta \in [0.4, 0.5]$ extending to higher elevations. This indicates an overprediction of the vertical spreading of the thermal plume. Moreover, for $r > 83$ ($r\langle\ell_z\rangle_b/R = 0.32$), ILES predicts a narrower and relatively colder outer region.

The vertical temperature profiles shown in figure 5.2, extracted at the city edge and near the domain boundary, further confirm these observations. At both radial locations, the profiles largely collapse, indicating that the large-scale thermal structure is robustly reproduced by the LES configurations. Nevertheless, small discrepancies persist. The WALE LES (red line) remains in close agreement with the DNS reference (black line), whereas the ILES solution (blue line) systematically overpredicts the mean temperature across the entire vertical extent. The coarse-grained simulations also capture the two vertical branches of the large-scale circulation, one originating from the heated roughness elements at the bottom plate and the other located near the outer region of the domain figure 5.3. In all cases, the urban region ($r < 25$, $r\langle\ell_z\rangle_b/R < 1$) is characterised by positive vertical velocity W, which

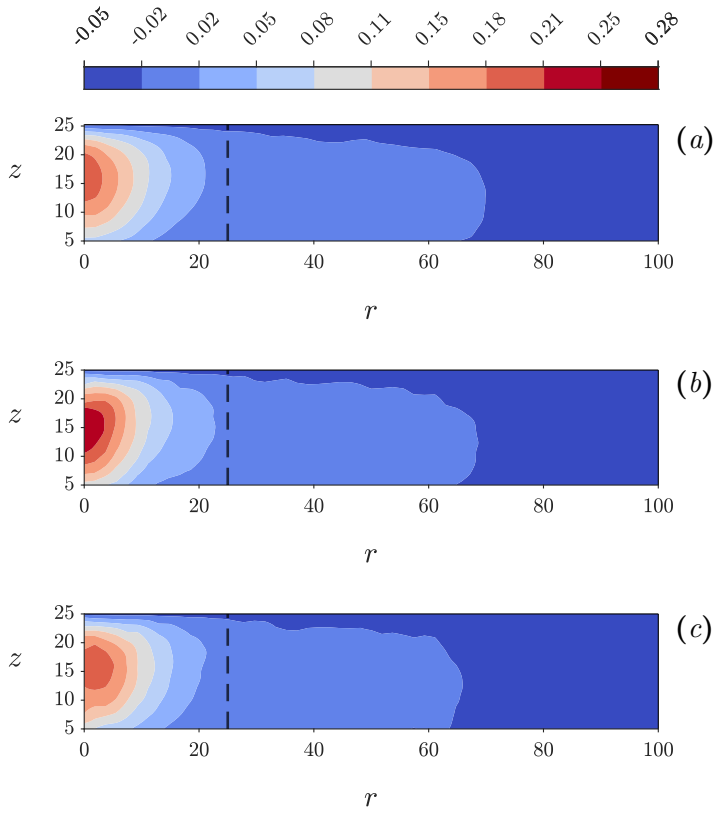

Figure 5.3: Contours of mean vertical velocity $W(r,z)/U_{ff}$ for the three simulations: (a) DNS, (b) ILES, and (c) WALE LES. The vertical dashed line indicates the location of the city boundary.

progressively decreases with increasing radial distance from the city centre. The maximum upward velocity is observed at approximately $z \sim 17$, above which the urban updraft gradually weakens. In the ILES configuration (b), the mean vertical velocity exceeds that of the DNS (a). This behaviour is consistent with the previously identified temperature overprediction in the same region, which enhances buoyancy-driven acceleration.

The ascending branch of the large-scale circulation is located in the outer region of the domain, corresponding to the countryside. The vertical velocity profiles reported in figure 5.4 further support this interpretation. At the city boundary ($r = 1$, $r\langle \ell_z \rangle_b / R = 1$), all three simulations exhibit similar behaviour, with the ILES solution (blue curve) showing a slightly stronger

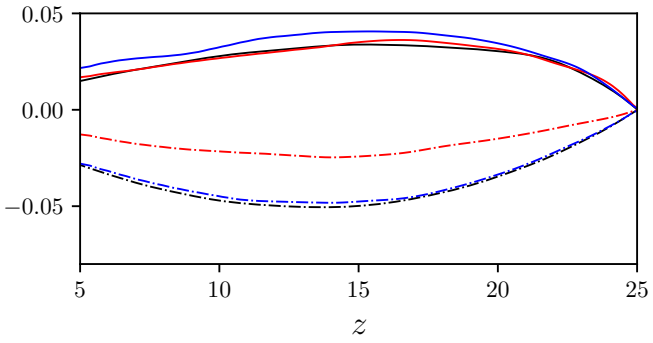

Figure 5.4: Vertical profiles of the mean vertical velocity $W(z)/U_{ff}$ at two radial locations: $r = 25$ (solid lines) and $r = 100$ (dash–dot lines). DNS (black), WALE LES (red), and ILES (blue).

upward motion. At the outer edge of the domain, DNS and ILES almost coincide, whereas the WALE LES predicts a weaker downward velocity, reaching only about 49% of the DNS magnitude. This discrepancy is consistent with the spatial distribution observed in the contour plots figure 5.3. The mean radial velocity contours figure 5.5 complete the description of the horizontal branches of the large-scale circulation. As previously discussed in chapter 4, the urban canopy region is characterised by a radially inward boundary layer. Both coarse-grained simulations consistently reproduce this behaviour. In the lower portion of the domain (approximately $z < 15$), the radial velocity remains negative, indicating flow directed towards the canopy. Conversely, above $z > 17$, the radial component becomes predominantly positive up to the top boundary, particularly around $r \sim 90$ ($r\langle \ell_z \rangle_b / R < 3.6$), corresponding to the descending branch of the large-scale circulation where the flow spreads outward. The WALE LES figure 5.5(c) exhibits a slightly stronger outward radial component in the near-canopy region for $z < 2.5$, particularly around $r \sim 9$ ($r\langle \ell_z \rangle_b / R < 0.1$). This enhanced radial spreading is consistent with the behaviour observed in the vertical velocity field, where the upward motion appears more spatially extended compared to both DNS and ILES, see figure 5.3(c). In particular, vertical velocities in the range $[0.115, 0.181]$ for $r < 8$ ($r\langle \ell_z \rangle_b / R < 0.32$) occupy a broader region. As a consequence, the thermal plume in the WALE configuration expands radially at lower elevations. By contrast, the ILES configuration exhibits a more rapid radial decay of the outward velocity in the upper portion of the domain ($z > 18$), indicating a comparatively more confined plume structure at

higher altitudes. The vertical profiles of the mean radial velocity are shown in figure 5.5. At $r = 25$ ($r\langle \ell_z \rangle_b / R = 1$), the three simulations display very similar behaviour, with both ILES and WALE LES slightly overpredicting the radial velocity relative to the DNS while preserving the overall profile shape. At the outer boundary, the discrepancies become more pronounced. The WALE LES remains in close agreement with the DNS throughout the vertical extent, whereas the ILES solution overestimates the radial velocity below the height at which the sign inversion occurs ($U_r = 0$). Above $z > 15$, ILES predicts a significantly weaker outward radial velocity, reaching only about 22% of the DNS magnitude (0.013 compared to 0.058).

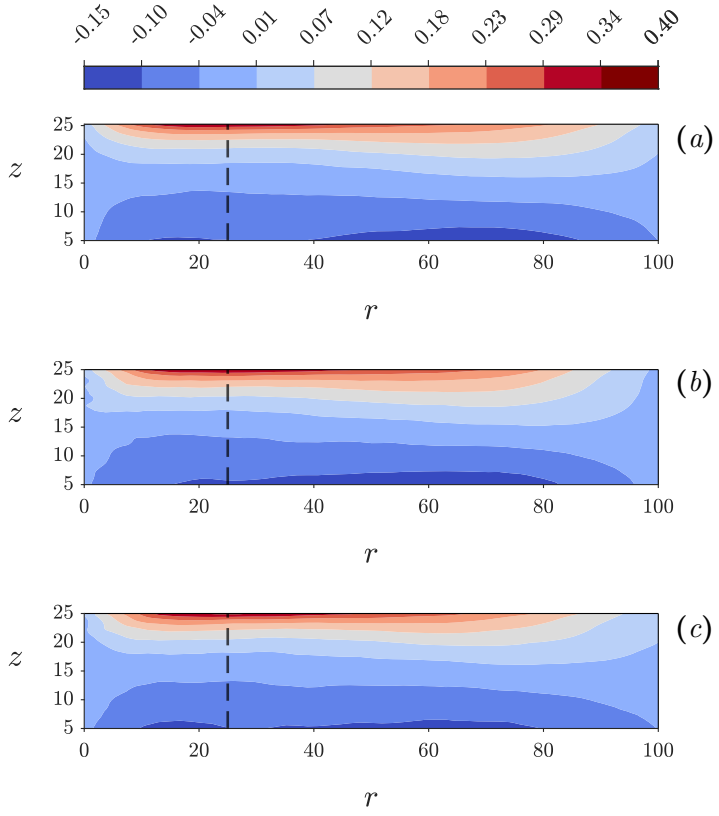

Figure 5.5: Contours of mean radial velocity $U_r(r, z)/U_{ff}$ for the three simulations: (a) DNS, (b) ILES, and (c) WALE LES. The vertical dashed line indicates the location of the city boundary.

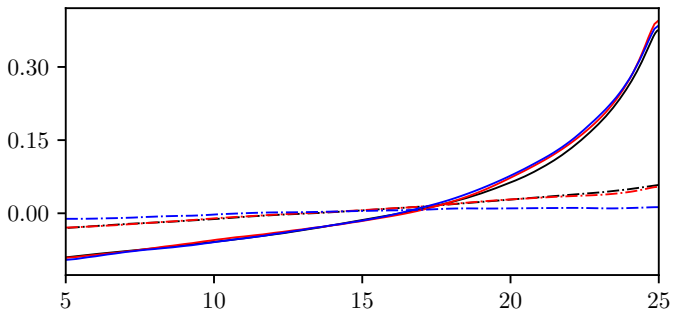

Figure 5.6: Vertical profiles of the mean vertical velocity $U_r(z)/U_{ff}$ at two radial locations: $r = 25$ (solid lines) and $r = 100$ (dash–dot lines). DNS (black), WALE LES (red), and ILES (blue).

5.2.2 Turbulent mixing

Turbulent intensities are evaluated through the contours of the root-mean-square (rms) fluctuations of both temperature and velocity fields. Figure 5.7 presents the temperature rms for the three simulations. Both ILES and WALE LES (b–c) correctly identify the urban thermal plume as the region of maximum temperature fluctuations, in agreement with the DNS reference (a). In all configurations, the fluctuation levels are primarily confined within the urban area and progressively decrease both radially toward the rural surroundings and vertically toward the upper boundary. The rms of the vertical velocity component is reported in figure 5.8. The largest fluctuation levels are concentrated along the ascending and descending branches of the large-scale circulation (LSC), approximately located at $r < 20$ ($r\langle\ell_z\rangle_b/R < 0.8$) and $r > 80$ ($r\langle\ell_z\rangle_b/R < 3.2$), respectively. Compared to DNS, both LES configurations predict enhanced fluctuation intensities distributed over a broader spatial region. In particular, the zones of elevated rms values extend further toward the city centre, especially along the descending branch of the LSC.

A comparable spatial distribution is observed for the horizontal velocity fluctuations. The rms contours of the tangential and radial velocity components figures 5.10 and 5.9 display consistent patterns across all simulations. In each case, a pronounced fluctuation peak develops near the upper boundary, induced by the imposed boundary condition. This feature is particularly evident in the regions $r < 25$ ($r\langle\ell_z\rangle_b/R < 1$) and $r > 77$ ($r\langle\ell_z\rangle_b/R < 3.08$).

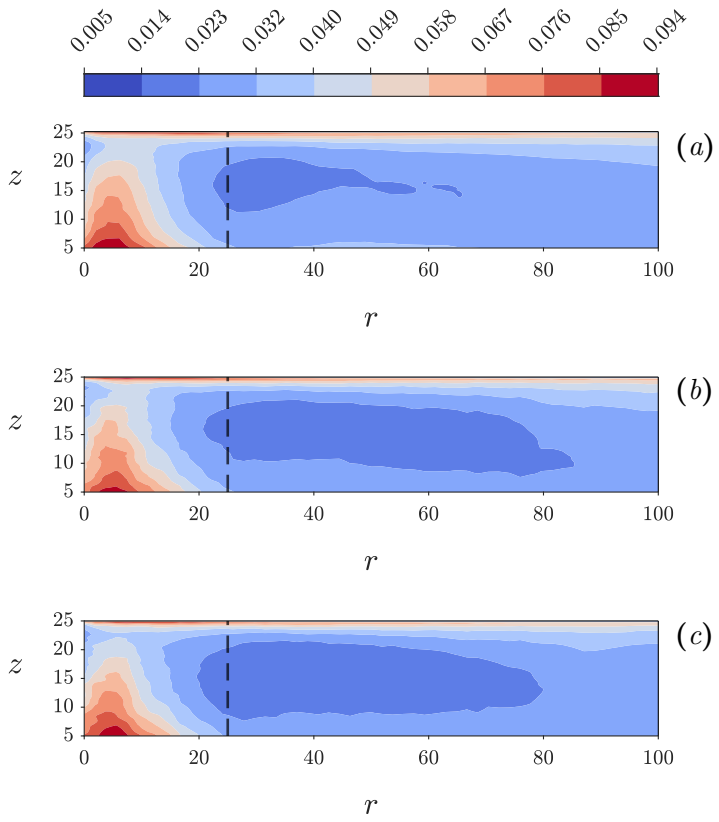

Figure 5.7: Contours of the standard deviation of temperature $\sqrt{\langle\theta'^2\rangle}(r,z)/\Delta\Theta_{max}$ for the three simulations: (a) DNS, (b) ILES, and (c) WALE LES. The vertical dashed line indicates the location of the city boundary.

A comparison between the modelling approaches reveals that the WALE LES (panel c of figure 5.10) systematically predicts lower fluctuation levels for both horizontal components.

5.3 Considerations

Before analysing the lower portion of the domain ($z \in [0, 5\langle\ell_z\rangle_b]$), it is useful to summarise the main findings obtained in the region above the canopy. For the implicit LES configuration, the mean temperature field is systematically overestimated with respect to the DNS reference, particularly

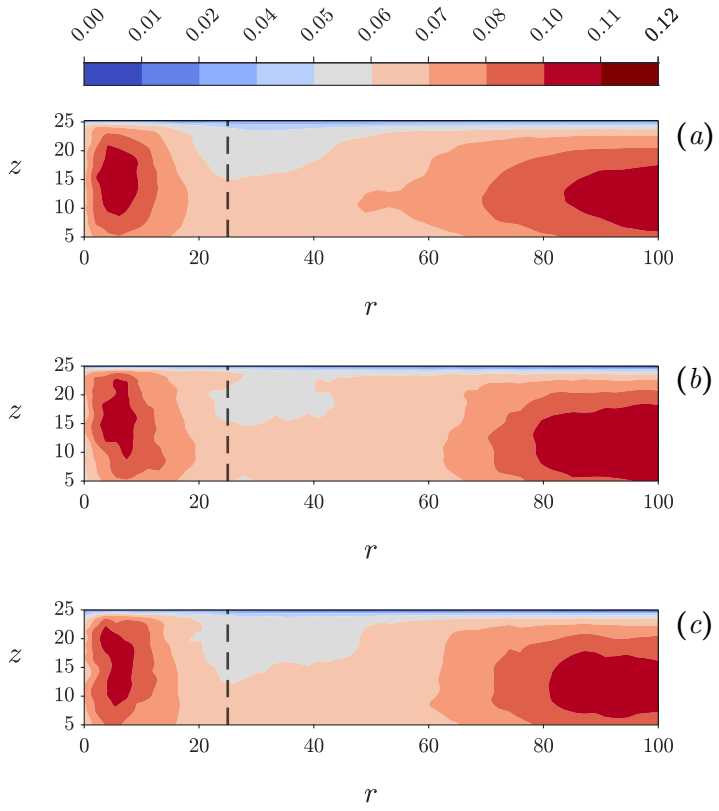

Figure 5.8: Contours of the standard deviation of vertical velocity $\sqrt{\langle w'^2 \rangle}(r, z)/U_{ff}$ for the three simulations: (a) DNS, (b) ILES, and (c) WALE LES. The vertical dashed line indicates the location of the city boundary.

above the city centre for $z < 11$. This thermal bias is reflected in an overestimation of the mean Nusselt number and in a strengthening of the large-scale circulation. In particular, the peak mean vertical velocity increases by approximately 19% relative to DNS. By contrast, the Wall Adapting Local Eddy-viscosity model provides a more accurate representation of the mean temperature distribution, indicating a more consistent balance between resolved momentum and thermal transport. The primary deviation from DNS concerns the structure of the large-scale circulation, whose vertical branches appear slightly broadened and shifted toward the domain centre. Considering the turbulent fluctuations, the WALE LES systematically underesti-

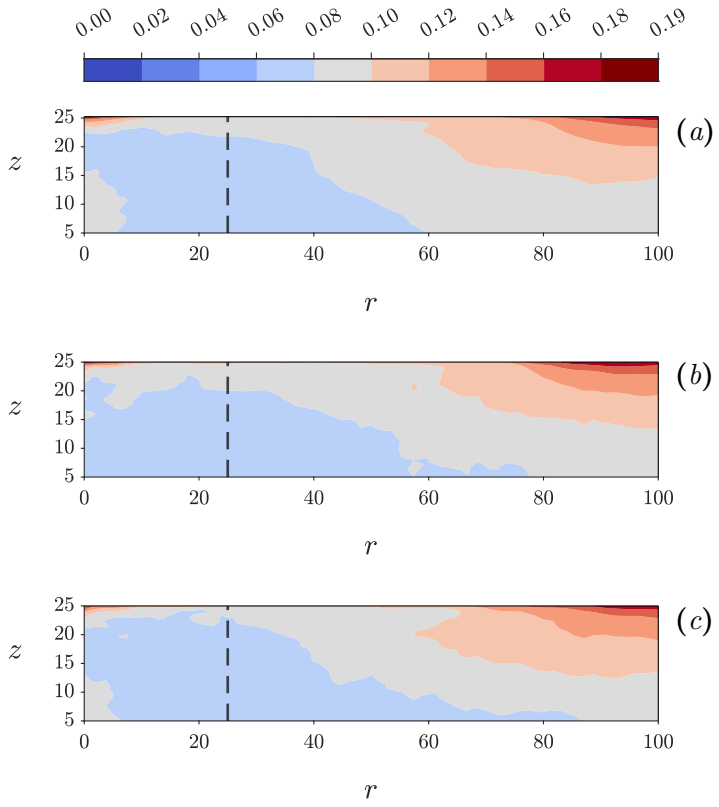

Figure 5.9: Contours of the standard deviation of radial velocity $\sqrt{\langle u_r'^2 \rangle}(r, z)/U_{ff}$ for the three simulations: (a) DNS, (b) ILES, and (c) WALE LES. The vertical dashed line indicates the location of the city boundary.

mates the rms levels, especially for the velocity components. This behaviour indicates a stronger damping of turbulent motions, likely associated with enhanced subgrid-scale dissipation. As a consequence, the WALE configuration exhibits a more diffusive behaviour than the DNS, leading to faster large-scale mixing but reduced fluctuation intensities in low-energy regions, together with a modified large-scale circulation structure. Although ILES is less accurate, its reduced computational cost makes it a efficient choice, as will be demonstrated in section 5.5.

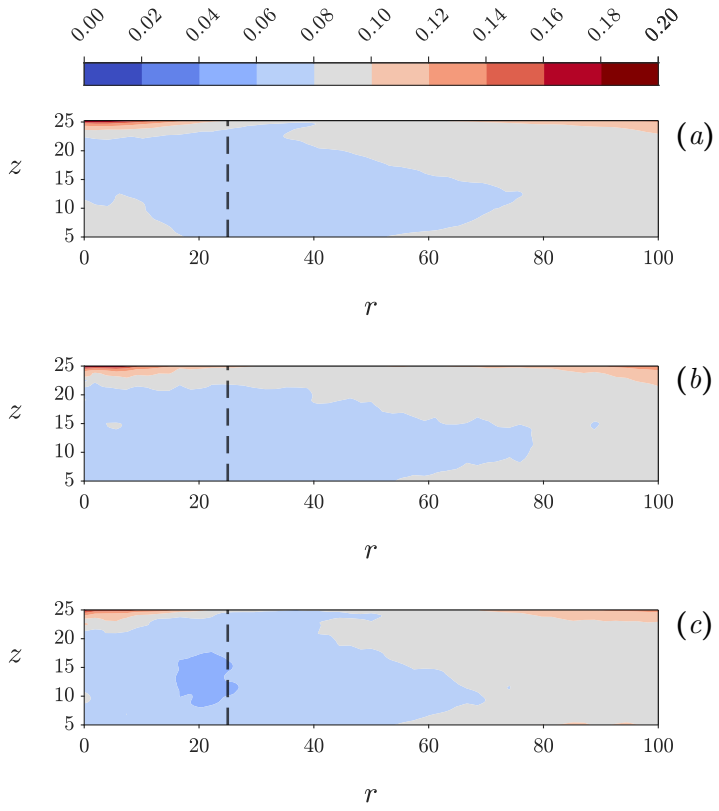

Figure 5.10: Contours of the standard deviation of tangential velocity $\sqrt{\langle u_\varphi'^2 \rangle}(r,z)/U_{ff}$ for the three simulations: (a) DNS, (b) ILES, and (c) WALE LES. The vertical dashed line indicates the location of the city boundary.

5.4 Urban canopy

The urban canopy layer ($0 < z < 5$) is analysed through time averaged contour fields. The mean temperature Θ slices extracted at the mid-plane of the city domain figure 5.11 clearly reveal the thermal plume emerging from the heated roughness elements in all simulations. The WALE LES (c) exhibits closer agreement with the DNS reference (a), particularly in the regions between buildings, where sharper temperature gradients and localized thermal structures are better preserved. This improved representation is consistent with the enhanced mesh refinement adopted in the WALE

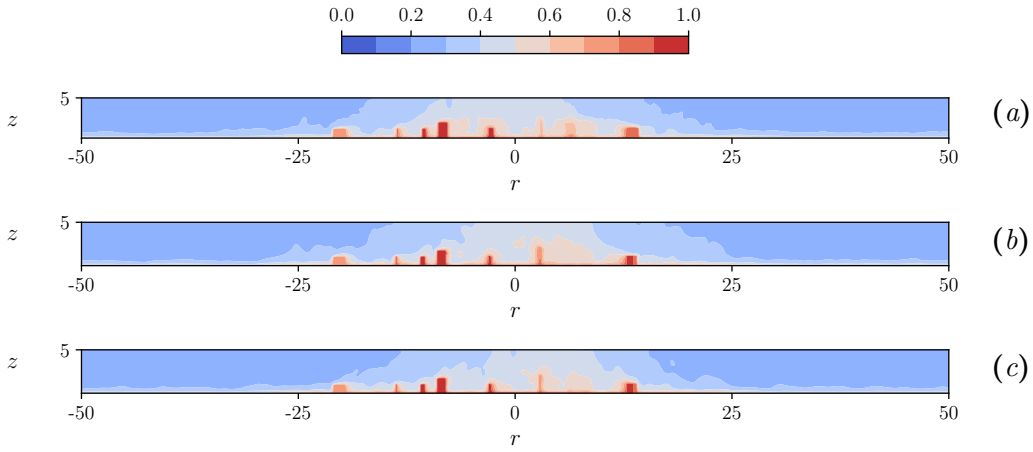

Figure 5.11: Contours of the mean temperature field $\Theta(r, z)/\Delta\Theta_{max}$ for the three simulations: (a) DNS, (b) ILES, and (c) WALE LES.

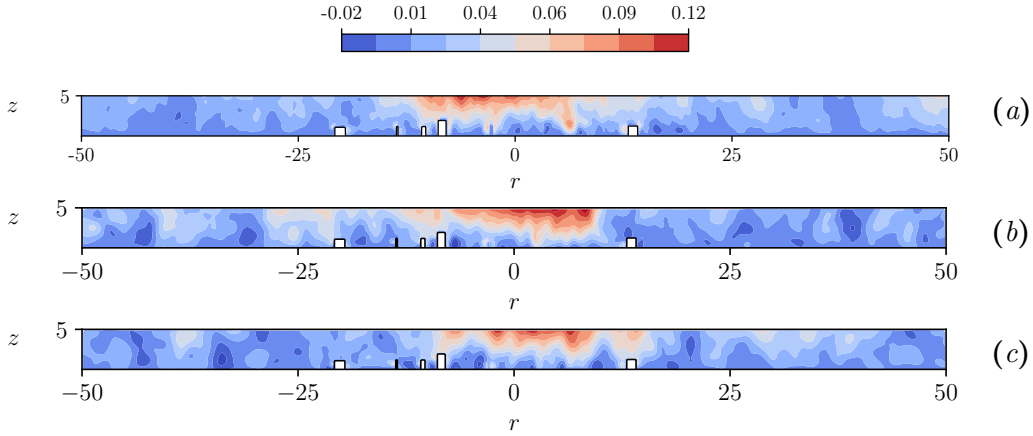

Figure 5.12: Contours of mean vertical velocity $W(r, z)/U_{ff}$ for the three simulations: (a) DNS, (b) ILES, and (c) WALE LES.

configuration. The mean vertical velocity slices figure 5.12 highlight the buoyancy-driven updraft developing within the city centre ($-10 < r < 10$), generated by the warmer roughness pattern. In this region, the WALE LES (c) displays a smoother and more diffused velocity distribution, whereas the ILES configuration (b) shows stronger spatial aggregation of the flow structures, resulting in locally higher velocity magnitudes compared to DNS.

5.5 Modelling considerations

The present analysis highlights the trade-off between computational efficiency and physical accuracy in coarse-grained simulations of urban thermal flows. From a computational perspective, both LES approaches provide a substantial reduction in cost compared to DNS. The ILES configuration is approximately 6 times faster than the reference simulation, whereas the WALE LES achieves a speed-up of about 4. This gain makes coarse-grained approaches attractive for parametric studies and large-domain simulations. In terms of mean-flow prediction, the WALE model delivers the most accurate representation of the temperature field, particularly within the urban canopy and in regions between buildings. The improved agreement with DNS is associated with enhanced near-wall resolution and an explicit subgrid-scale closure. However, this configuration exhibits a more diffusive character in the velocity field and systematically underpredicts turbulent fluctuation levels, indicating stronger subgrid-scale dissipation. The ILES configuration, on the other hand, tends to overestimate the mean temperature within the city and produces a more intense large-scale circulation. While this leads to deviations in buoyancy-driven acceleration and heat transfer, the overall large-scale organisation of the flow is preserved. Given its significantly lower computational cost, ILES represents a competitive alternative when the primary interest lies in global heat-transfer trends rather than in the detailed representation of local turbulence statistics. The present results allow us to identify several practical implications for LES of urban thermal flows. First of all, an adequate mesh refinement within the urban canopy is essential to capture gradients between buildings and shear-layer dynamics. Explicit subgrid-scale modelling (e.g. WALE) improves the prediction of mean thermal fields but may introduce enhanced dissipation of velocity fluctuations. A significantly reduced computational cost can be reached with implicit LES approaches that can provide acceptable accuracy for large-scale circulation and global heat-transfer. Overall, the choice between ILES and WALE should be guided by the specific objectives of the simulation: detailed local mixing and near-wall accuracy favour WALE, whereas large-scale trend analysis and computational efficiency favour ILES.

Chapter 6

High-Fidelity LES of mixed convection in paradigmatic urban environments

After assessing the effect of only buoyancy in an urban configuration, the study of the urban climate is extended to include the combined effect of buoyancy and wind forcing. This chapter analyses the results obtained from the coarse-grained simulations of the reference urban configuration under mixed convection conditions. In this present case, a turbulent colder flow impinges laterally on the urban geometry. Following the description of the new flow setup, results from implicit LES performed with OpenFOAM are presented, with particular attention on the different flow phenomena arising from the interaction between buoyancy and wind shear within an urban canopy.

6.1 Flow setup

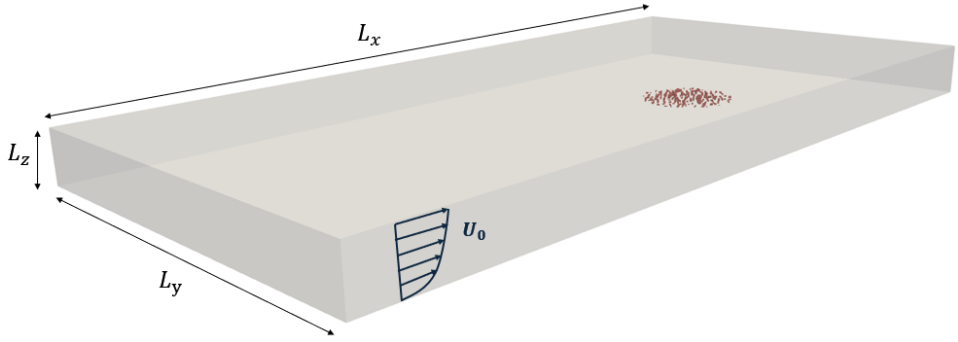

Figure 6.1: Schematic of the domain use for the mixed convection simulation. The urban pattern is highlighted in red.

In order to account for the effect of a wind shear on the urban configuration, the computational domain was extended along the wind direction by duplicating its original length without changing the resolution adopted in the pure convection case. A schematic of the new domain is reported in figure 6.1. This was due to allow the flow to fully develop and transition to turbulence before reaching the urban pattern, which is now centred at $L_x = 12R$ from the inlet, where R denotes the radius of the city. The complete set of domain parameters is reported in table 6.1. A further modification concerns the boundary conditions adopted in this new setup. Fixed value for the velocity field is imposed at the inlet plane for $x = 0$, combined with an outflow condition at $x = 16R$ to prevent a reverse flow. At the bottom wall, the top boundary and at the two lateral sides for $y = 0$ and $y = 8R$, the boundary conditions remain unchanged with respect to the previous configuration thus no slip and impermeable condition for the bottom plate and periodic boundary condition for the lateral sides.
Similarly, for the temperature field, in order to consistently model nocturnal urban heat island conditions while maintaining a global temperature difference of $\Delta\Theta_{max} = 1$ across the entire domain, a fixed temperature value is prescribed at the inlet, $\theta(0, y, z, t) = \Theta_{atm}$. At the top boundary and at the outlet, a Neumann boundary condition with zero normal derivative is imposed. The temperature distribution within the urban canopy remains unchanged with respect to the pure convection case, such that $\Theta_{atm} < \Theta_{country} < \Theta_{city}$, with also $\Delta\Theta_{country}/\Theta_{atm} = 0.5$, $\Delta\Theta_{city}/\Theta_{atm} = 0.5$ respectively. A general overview of the flow evolution shows that a colder inflow enters the domain, progressively warms up and becomes turbulent as it approaches the urban roughness.

$L_x \times L_y \times L_z$	$nx \times ny \times nz$	Refinement	Total cells	CPU hours
$16R \times 8R \times R$	$1100 \times 550 \times 145$	1*	$8.8 \cdot 10^7$	32256

Table 6.1: Domain parameters for the mixed convection case. The asterisk (*) in the Refinement column indicates a uniform surface refinement level of 1 for the city region.

In this regard, to quantify the relative importance of buoyancy forces compared to inertial forces, it is necessary to introduce another dimensionless control parameter, namely the Richardson number, defined as:

$$\mathrm{Ri} = \frac{\beta g \Delta\Theta L_0}{U_0^2} \tag{6.1}$$

where U_0 denotes the reference velocity, L_0 the reference length, $\Delta\Theta$ the reference temperature difference in the domain, g the gravitational acceleration and β the thermal expansion coefficient. The Richardson number can also be rewritten considering the ratio between velocity induced by buoyancy, the free-fall velocity and the velocity induced by an external forcing as:

$$\mathrm{Ri} = U_{ff}^2/U_0^2 \tag{6.2}$$

According to its values, different flow regimes can be identified ranging from the buoyancy dominated or natural convection, when $\mathrm{Ri} \gg 1$, to forced convection, for $Ri \ll 1$, where temperature acts as a passive scalar and buoyancy effects are completely negligible. The present study lies between this opposite flow dynamics: since mixed convection regime is considered, the velocity induced by buoyancy is comparable to the velocity generated by external forcing, resulting in $\mathrm{Ri} \sim 1$.
While the Richardson number characterizes the relative importance of buoyancy and inertial forces and therefore defines the dynamical regime of the flow, it does not provide information on the global thermal balance of the system. In order to assess the heat transfer and to verify that a statistically stationary state has been reached, an additional dimensionless parameter is introduced, the Stanton number:

$$\mathrm{St} = \frac{q_w}{\rho c_p \Delta\Theta U_0} = \frac{\Theta_{outlet} - \Theta_{inlet}}{\Delta\Theta_{max}} \tag{6.3}$$

where q_w indicates heat flux computed at the wall and the second equality follows from a global heat balance between inlet and outlet sections.

In the present simulation the imposed inflow velocity is set such that $U_0/U_{ff} = 0.71$ and the Richardson number computed at the city centre is 1.98 as reported in table 6.2 together with the remaining flow parameters. In order to provide a physical interpretation of these values, and consistently with the scaling arguments discussed in the pure convection case, chapter 4, considering the same range of surface layer $H \sim 500m$, and a temperature differences between the city and the atmosphere $\Delta\Theta_{max} \sim 20°C$, the corresponding value for the Reynolds number, based on the inlet velocity would be of the order would be of order $\mathrm{Re} \sim 10^8$ which is typical of real atmospheric flows but not accessible due to computational reason.
Nevertheless, the simulated flow is primarily governed by the interplay between buoyancy and inertial forcing, quantified through the Richardson number. Therefore, the simulations are expected to capture the dominant

physical mechanisms characterizing full-scale urban mixed convection flows, despite the lower Reynolds number achievable numerically. Given the results obtained using implicit LES in chapter 5 combined with the lower computational cost, we chose to adopt the same approach for the mixed convection case. As in chapter 5 the ILES simulation was carried out with OpenFOAM using the *buoyantBoussinesqPimpleFoam* solver and keeping all the numerical settings unchanged.

$\mathrm{Ri}_{r=0}$	Ra	Re	Pr	$\overline{\mathrm{St}}$
1.98	10^8	340	0.7	0.038

Table 6.2: Flow settings for the mixed convection case. The Richardson number is computed at the city centre for $r = 0$ where $\Delta\Theta_{max} = 1$. Re is evaluated considering the mean buildings height as a reference length.

6.2 Results

To ensure consistency with the results presented in chapter 4, all statistics reported in the following sections are expressed in dimensionless form. The mean buildings height $\langle \ell_z \rangle_b$, is adopted as the reference length scale, while the free-fall velocity $U_{ff} = \sqrt{g\beta\Delta\Theta_{max}H}$ is used as the reference velocity scale. Furthermore, for clarity, a Cartesian coordinate system is adopted instead of the cylindrical one previously used, since the azimuthal symmetry is no longer present in the current configuration. In this framework, the city centre is located at $(L_x, L_y, L_z) = (100\langle \ell_z \rangle_b, 100\langle \ell_z \rangle_b, 0)$.

6.2.1 Instantaneous flow fields

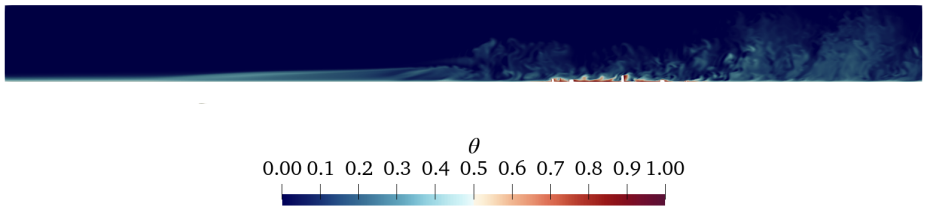

Figure 6.2: Slices of instantaneous dimensionless temperature field θ in the x–z plane taken at $y = 4R$

To provide a qualitative overview of the flow dynamics prior to discussing the time-averaged fields, instantaneous visualisations of the velocity and temperature fields at $t = 55$ free fall times are presented. The instantaneous temperature slice for a portion of the domain for $x \in [-50\langle\ell_z\rangle_b, 200\langle\ell_z\rangle_b]$, and shown in figure 6.2, clearly illustrates the streamwise development of the thermal field. Upstream of the urban canopy, the flow remains initially laminar and characterised by a relatively smooth thermal boundary layer growing from the bottom wall. As the colder incoming flow approaches the heated urban region, the boundary layer thickens and progressively undergoes transition, leading to the formation of turbulent structures. Downstream of the city, a turbulent thermal wake is observed, marked by irregular temperature fluctuations and enhanced vertical mixing.

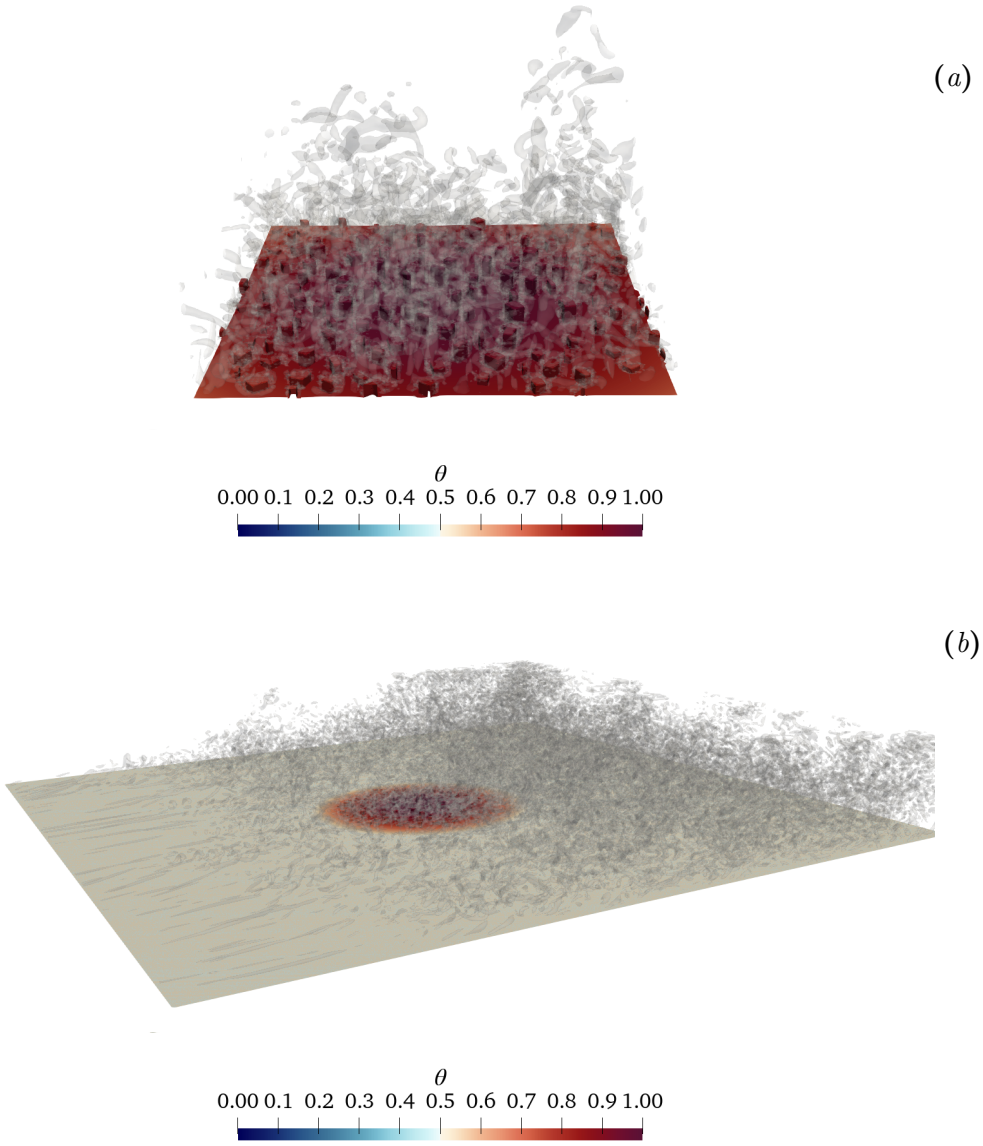

Figure 6.3: Iso-surfaces of the instantaneous Q-criterion at Q=0.85. Buildings and the ground surface are colored according to the instantaneous temperature field. The visualization shows a zoomed view of: (a) city region and (b) lower part of the computational domain.

The visualisation of positive values of the Q-criterion restricted to the

subdomain $x \in [0, 200\langle \ell_z \rangle_b]$, $y \in [0, 200\langle \ell_z \rangle_b]$, and $z \in [0, 25]$, figure 6.3, highlights regions where rotational effects dominate over strain, thus identifying coherent vortical structures. Upstream of the canopy, several hairpin vortices can be observed that under mean shear enhance vertical transport by lifting low-momentum, warmer fluid away from the wall while entraining colder fluid downward. A clear concentration of vortical structures is detected also within the canopy region, where the roughness pattern induces flow separation and local shear layers around the buildings, which promote vortex generation and intensify turbulence production that leads to enhanced mixing. Vertical slices at different streamwise locations, figure 6.4, further clarify the flow evolution. The instantaneous temperature field, figure 6.4(a), reveals the formation of streamwise elongated thermal streaks originating from the heated bottom surface. These structures exhibit a temperature contrast with the background and their axis is aligned with the mean flow direction. While thermal forcing initiates vertical updrafts, the mean velocity gradient stretches and organises them into coherent streamwise structures. Further downstream, figure 6.4(b), the flow exhibits a fully developed turbulent state, with fluctuations spanning more than half of the vertical extent of the domain. In the urban region, where the imposed temperature is higher than the surroundings, it is possible to note additional buoyant plumes originating also from the building surfaces.

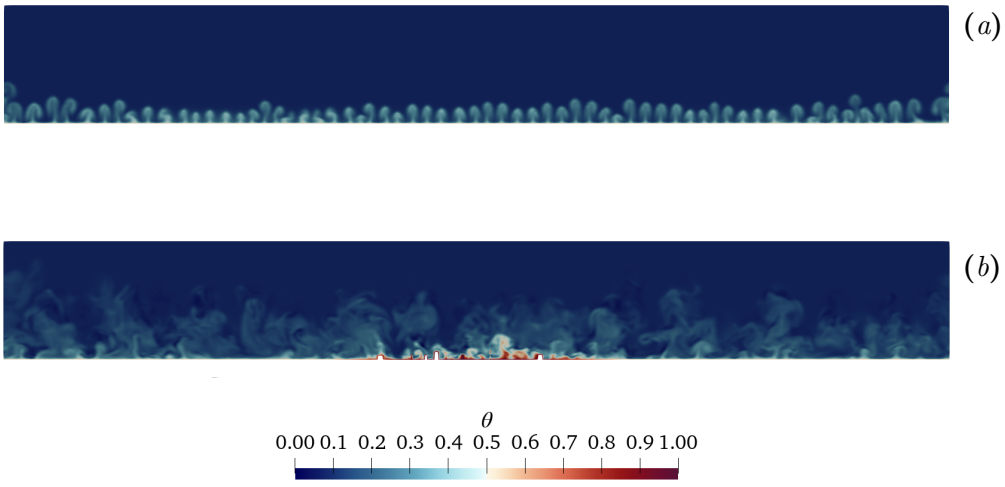

Figure 6.4: Slices of instantaneous dimensionless temperature field θ in the y–z plane at (a) $x = 0$ and (b) $x = 100\langle \ell_z \rangle_b$.

6.2.2 Mean fields

Due to the lack of symmetry in the present configuration, spatial averaging is no longer possible and the statistical analysis relies exclusively on time averaging. The mean fields are therefore computed over a time window of 127 freefall times, corresponding to more than 60 statistically independent snapshots. Slices of the mean temperature field in the x–z plane, limited to the interval $x \in [200\langle \ell_z \rangle_b, 25\langle \ell_z \rangle_b]$ and taken both outside and at the centre of the urban region, figure 6.5, reveal markedly different behaviours as discussed so far. The edge slice, figure 6.5(a), shows that the domain can be clearly divided into two regions separated approximately at $H/2 = 12.5$. The upper half of the domain is almost entirely occupied by the coldest fluid of the system, maintaining an approximately constant thickness along the streamwise direction. In contrast, the lower half exhibits a progressive evolution of the thermal boundary layer. Near the inlet region, the flow remains laminar, and the temperature boundary layer grows gradually in thickness. As the flow approaches the urban region, the boundary layer undergoes transition and becomes increasingly turbulent.

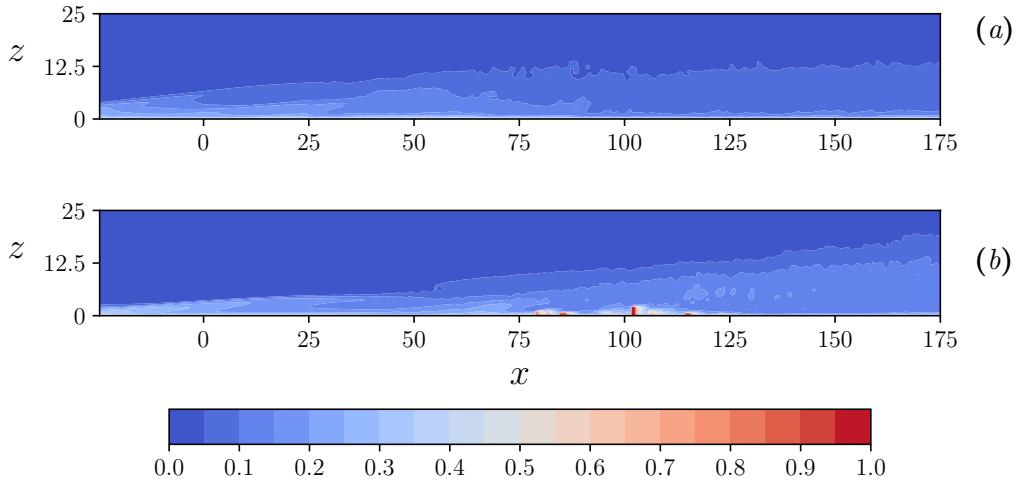

Figure 6.5: Slices of mean temperature fields $\Theta(x, z)/\Delta\Theta_{max}$ in the x–z plane at (a) $y = 0$ and (b) $y = 100\langle \ell_z \rangle_b$.

The middle slice, figure 6.5(b), highlights the combined effect of surface roughness and of the imposed non uniform bottom temperature distribution.

In contrast with the outer slice, the cold upper region does not preserve a constant thickness. Starting from $x \sim 50\langle \ell_z \rangle_b$, its vertical extent decreases due to the upward transport of warmer fluid induced by turbulent motions subsequently enhanced by the urban roughness. The interaction between shear and buoyancy therefore modifies the vertical thermal stratification within the canopy region. Focusing on the urban area, higher temperatures are observed due to the imposed boundary conditions. Under the action of the incoming colder wind, heat is advected downstream, generating a distinct warm wake. Consequently, lower temperatures are detected at the windward side of the city, while the central and downstream portions of the urban canopy, together with the immediate wake region, exhibit higher mean temperature values, figure 6.5(b).

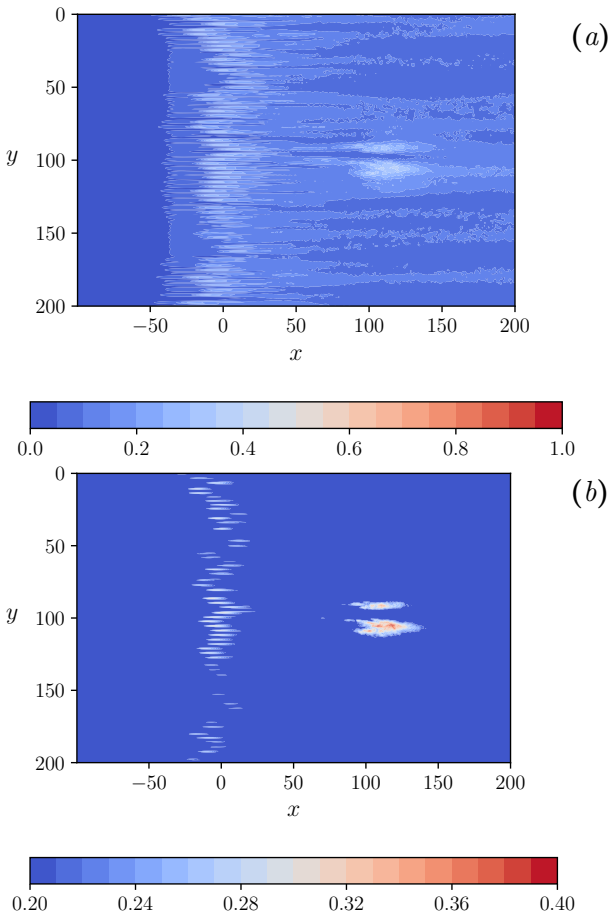

Figure 6.6: Slices of mean temperature field $\Theta(x, y)/\Delta\Theta_{max}$ in the x–y plane at (a) $z = 0.1H$ and (b) $z = 0.1H$. In (b) the colorbar is saturated to highlight the city wake.

The footprint of this warm wake is also visible in horizontal slices, figure 6.6. At $z = 0.1H$ above the building height, two warmer bands can be identified emerging from the city centre and extending approximately $2R$ downstream. These structures reach mean temperature values of about 0.35, corresponding to nearly one third of the maximum imposed temperature difference. Although less intense than the urban core, their persistence highlights the efficiency of downstream heat advection and the longitudinal spreading of the thermal wake.

The streamwise development of the mean temperature field, figure 6.7,

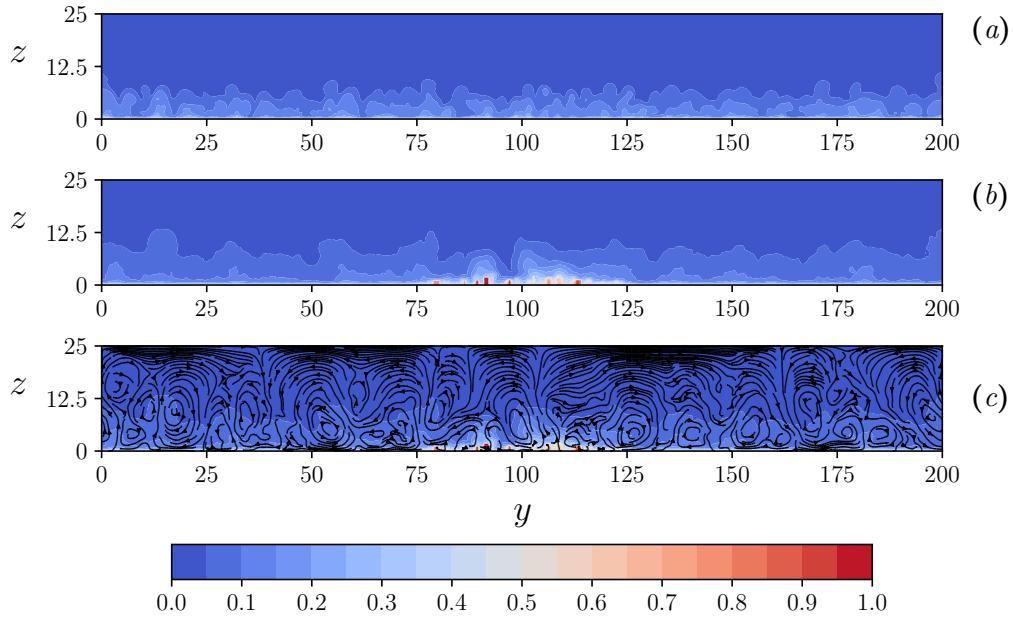

Figure 6.7: Slices of mean temperature field $\Theta(y, z)/\Delta\Theta_{max}$ in the x–z plane at (a) $x = 0$,(b) $x = 4$ and (c) $x = 4$ with superimposed mean streamlines.

further confirms this scenario. At the middle domain section, figure 6.7(a), where transition begins, regions of ascending warm fluid emerge from the heated bottom boundary in a relatively homogeneous manner all along the section. Further downstream at $x = 100\langle\ell_z\rangle_b$, reported in figure 6.7(b), the warmer layer has significantly increased in thickness, leading to a reduction of the cold upper region with the urban core which remains distinctly warmer than the surrounding areas. This behaviour reflects enhanced turbulent mixing, which intensifies vertical heat transport while redistributing temperature within the bulk of the flow. The mean streamlines superimposed on the mean temperature contours in figure 6.7(c) provide insight into the underlying flow organisation. A large-scale circulation (LSC) spanning the entire spanwise extent of the domain can be identified. In particular, the urban region is characterised by two counter-rotating circulation cells emerging around $y = 4R$, which extract heat from the canopy and transport it towards the outer regions of the domain. As the flow ascends, by mixing with the outer region, it cools and reaches the top boundary, where

it spreads radially outward and subsequently descends along the peripheral regions, thereby completing the circulation circle. The influence of the free-slip boundary condition at the top wall is also evident: streamlines in the upper part of the domain are predominantly horizontal, consistent with the upper region of the large-scale recirculation established within the domain. Complementing the two-dimensional representation, figure 6.8(a–b) presents three-dimensional streamlines extracted from the mean flow field. Figure 6.8(a) highlights the vertical acceleration of the flow at the upstream edge of the canopy, where the streamlines bend upward as a consequence of the buoyancy motion and both impingement and blocking effects, generated by the heated urban roughness. Furthermore, figure 6.8(b) shows that streamlines travelling along the periphery of the city are progressively entrained into the ascending branch. This behaviour reflects mass conservation requirements, as the upward transport of warm fluid must be balanced by compensating inflow from the surrounding regions.

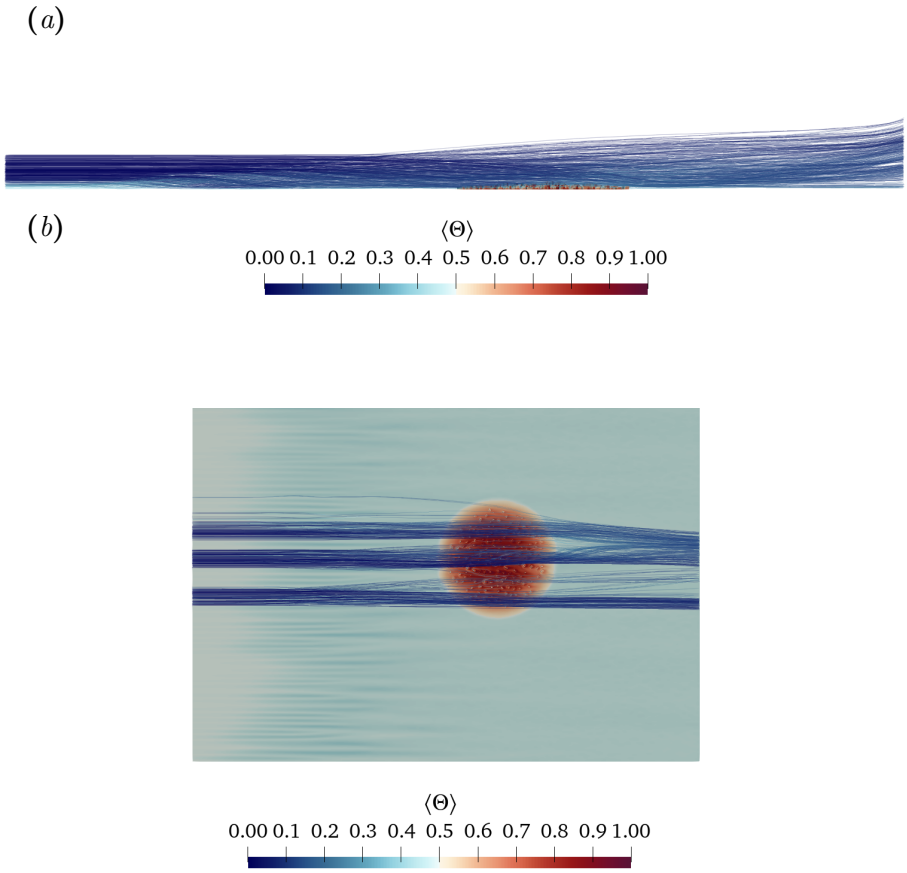

Figure 6.8: Three-dimensional streamlines of the mean field. The streamlines highlight the trajectory above the ground. Buildings and the bottom surface are coloured according to the mean temperature. (a) Slice taken at $y = 0$ and (b) plan view of the x–y plane.

Chapter 7

Urban Canopy parametric studies

Following the assessment of best-practice guidelines for LES in urban environments in chapter 5, the numerical framework is here employed to perform a parametric study of idealized urban canopies. Seven additional urban configurations are generated by varying three key morphological parameters: the plan area density coverage λ_p, the average building vertical aspect ratio $\mathcal{AR}_z$, and the coefficient controlling the radial distribution of building heights ϵ, which defines the overall city-shape profile, and investigated by means of implicit LES using OpenFOAM. This choice is motivated by the reduced computational cost compared to DNS and by the good agreement previously demonstrated between implicit LES and DNS results for the reference configuration. The validated LES framework therefore enables the exploration of a broader parametric space while maintaining high-fidelity resolution of the dominant flow and thermal structures. Each urban configuration is investigated under both pure and mixed convection regimes. The analysis focuses on global heat transfer indicators. In particular, the different configurations together with the reference canopy adopted in the best-practice study, are compared in terms of Nusselt number for the pure convection cases and Stanton number for the mixed convection cases, thus providing a unified measure of the thermal exchange efficiency across the eight considered urban morphologies. After a brief description of the generated city patterns, the results are presented separately for pure and mixed convection, followed by a comparative discussion highlighting the influence of each morphological parameter.

7.1 Urban canopies

Table 7.1 summarizes the five parameters characterizing each urban configuration generated from scratch through the algorithm described in chapter 2. Each canopy is uniquely defined by a specific combination of the five

key urban parameters, morphological descriptors starting from the reference canopy adopted in the DNS study, case 1 in table 7.1, allowing for an exploration of the urban parameter space. While all five parameters define the geometric configuration, the present parametric study primarily focuses on the influence of the first three, namely the plan area density, λ_p, the average building vertical aspect ratio $\mathcal{AR}_z$, and ϵ, the coefficient controlling the radial height distribution on the global heat-transfer performance. These are selected and independently varied, each assuming two distinct values, whereas all other geometric characteristics are kept unchanged.

Simulation	λ_p	$\mathcal{AR}_z$	ϵ	$\mathcal{AR}_p$	n
1	0.08	1.68	1.08	1.7	176
2	0.11	1.67	1.07	1.65	227
3	0.08	1.09	0.7	1.69	179
4	0.098	1.1	0.72	1.72	211
5	0.08	1.68	0.76	1.68	182
6	0.11	1.68	0.8	1.75	243
7	0.11	1.12	0.47	1.70	234
8	0.09	1.09	0.48	1.62	183

Table 7.1: Reference urban canopies parameters for each case study.

7.2 Pure convection

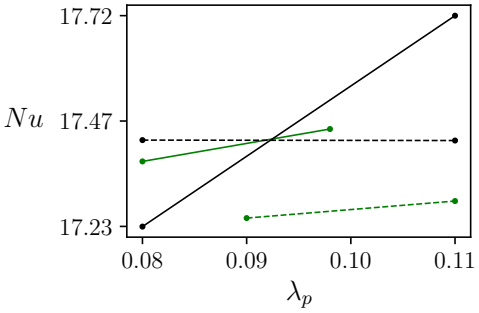

Figure 7.1: Nusselt number Nu as a function of the plan area density λ_p for different values of the smoothing parameter ϵ and vertical aspect ratio $\mathcal{AR}_z$. Green curves refer to $AR_z \sim 1.1$, and black curves to $AR_z \sim 1.68$. Green dashed lines correspond to $\epsilon \sim 0.48$, green solid lines to $\epsilon \sim 0.71$ while black dashed lines represent $\epsilon \sim 0.78$ and black solid lines $\epsilon \sim 1.08$.

Starting from the pure convection analysis, figure 7.1 reports the variation of the Nusselt number as a function of the plan area density λ_p for the different canopy configurations. In general, heat transfer efficiency increases with increasing density coverage, although the magnitude of this enhancement strongly depends on the specific urban morphology. In the configuration characterized by $\mathcal{AR}_z \sim 1.68$ and $\epsilon \sim 1.08$, black solid line, an increase of density coverage of approximately 27% results in a 2.76% increase in the Nusselt number. Figure 7.2 shows two instantaneous slices of the temperature field θ for simulation 1, 7.2(a) with $\lambda_p = 0.08$, and for simulation 2, 7.2(b) with $\lambda_p = 0.11$ as a reference for this effect.

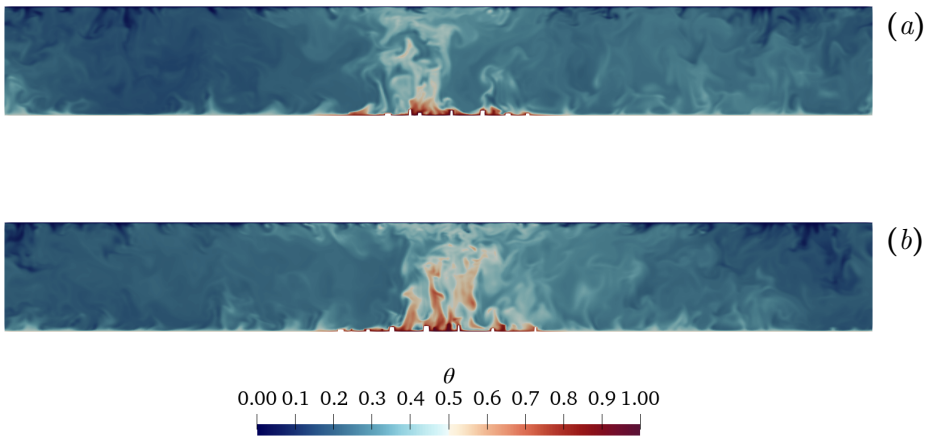

Figure 7.2: Instantaneous slices of dimensionless temperature θ in the x–z plane taken in the middle of the domain at 350 free-fall times. Panel (a) shows simulation 1 with $\lambda_p = 0.08$ while (b) shows simulation 2 with $\lambda_p = 0.11$.

By contrast, in two other configurations, solid and dashed green lines in figure 7.1, an 18% increase in λ_p leads to a much weaker enhancement of heat transfer, below 0.5%, indicating a limited sensitivity to density variations in those cases. To interpret these trends, the combined influence of vertical aspect ratio and radial smoothing must be considered. For canopies characterized by taller and more slender buildings ($\mathcal{AR}_z > 1.5$), increasing the plan area density enhances vertical heat transport when the radial smoothing is weak ($\epsilon \sim 1$). In this configuration, the peripheral buildings retain significant height, contributing effectively to roughness induced mixing and plume generation across a wider portion of the urban area. Vice versa, when $\epsilon < 1$, stronger radial smoothing produces a pronounced height difference between the city centre and the periphery, resulting in significantly lower buildings in the outer region. In this case, part of the peripheral roughness may remain embedded within the thermal boundary layer, reducing its contribution to vertical heat exchange. As a consequence, increasing the density is not reflected into a comparable increase in global heat transfer. This is confirmed also, when considering buildings with $\mathcal{AR}_z \sim 1$, where the combined effect of stronger radial smoothing and increased density can even lead to a slight reduction in heat transfer efficiency.

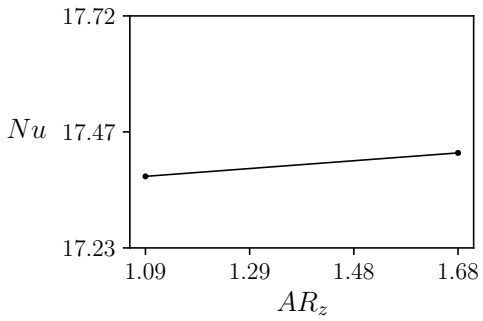

Figure 7.3: Nusselt number Nu as a function of the vertical aspect ratio $\mathcal{AR}_z$ for different values of the smoothing parameter ϵ and the plan area density λ_p. Black solid line refers to $\lambda_p \sim 0.08$ $\epsilon \sim 0.73$.

Concerning the dependence of the Nusselt on the vertical aspect ratio $\mathcal{AR}_z$, figure 7.3 reports a representative configuration for for $\lambda_p \sim 0.08$ $\epsilon \sim 0.73$ considering the maximum variation of the vertical aspect ratio. As $\mathcal{AR}_z$ increases by a 35% the Nusselt number rises from 17.378 to 17.428 that corresponds to an enhancement of 0.29%. Although moderate, this increase confirms that taller and more slender buildings promote slightly stronger vertical heat transport, consistently with the trends previously discussed for the density variation. An illustrative example of this effect can also be observed in figure 7.4, where the lower slice, panel b corresponds to a configuration characterised by higher heat transfer efficiency.

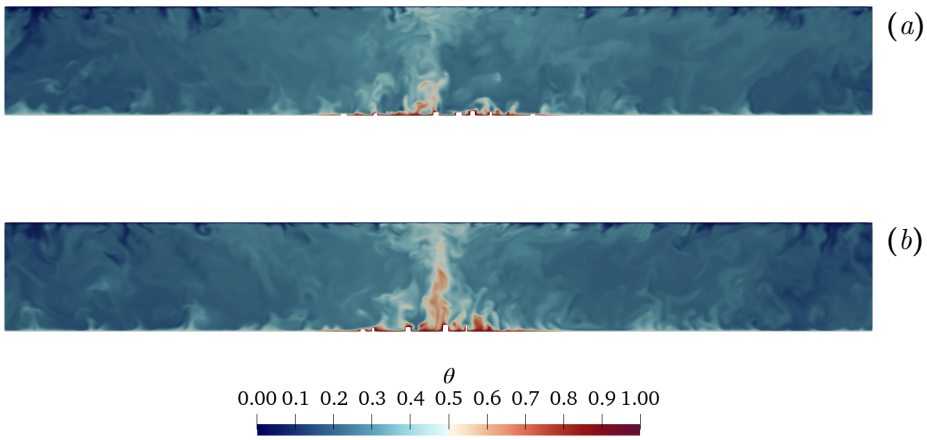

Figure 7.4: Instantaneous slices of dimensionless temperature θ in the x–z plane taken in the middle of the domain at 350 free-fall times. Panel (a) shows simulation 3 characterized by $\mathcal{AR}_z = 1.09$ while (b) shows simulation 5 with $\mathcal{AR}_z = 1.68$.

Finally, the influence of the radial smoothing parameter ϵ on the global heat transfer, shown in figure 7.5, reveals two distinct behaviours depending on the plan area density. For the configuration characterized by $\mathcal{AR}_z \sim 1.67$ and $\lambda_p \sim 0.11$, red solid line in figure 7.5, decreasing ϵ by approximately 25%, from 1.07 to 0.8, leads to a reduction of about 1.6% in the Nusselt number, from 17.72 to 17.427. On the other hand, for the configuration with the same vertical aspect ratio but lower density $\lambda_p \sim 0.08$, a reduction of ϵ of nearly 30%, results in an increase of approximately 1.2% in heat transfer efficiency. This apparently opposite behaviour highlights the coupled effect between radial smoothing and surface coverage. At lower density, stronger radial smoothing concentrates the tallest buildings in the central region where temperature gradient are higher. This concentration leads to a slightly higher Nusselt number. When ϵ increases and the height distribution becomes more uniform, the peripheral buildings are not sufficient to generate comparable additional mixing, resulting in a small reduction in global heat transfer. This behaviour is further illustrated by the instantaneous temperature slices shown in figure 7.5.

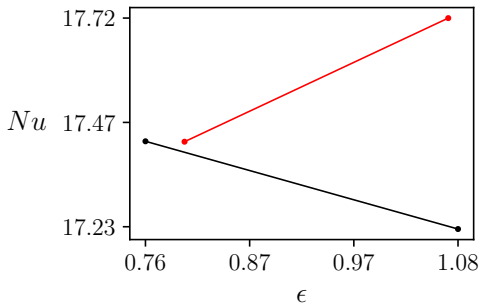

Figure 7.5: Nusselt number Nu as a function of the smoothing parameter ϵ for different values of the vertical aspect ratio $\mathcal{AR}_z$ and the plan area density λ_p. Black solid line refers to $\lambda_p \sim 0.08$ and $\mathcal{AR}_z \sim 1.68$ while red solid line corresponds to $\lambda_p \sim 1.1$ and $\mathcal{AR}_z \sim 1.67$.

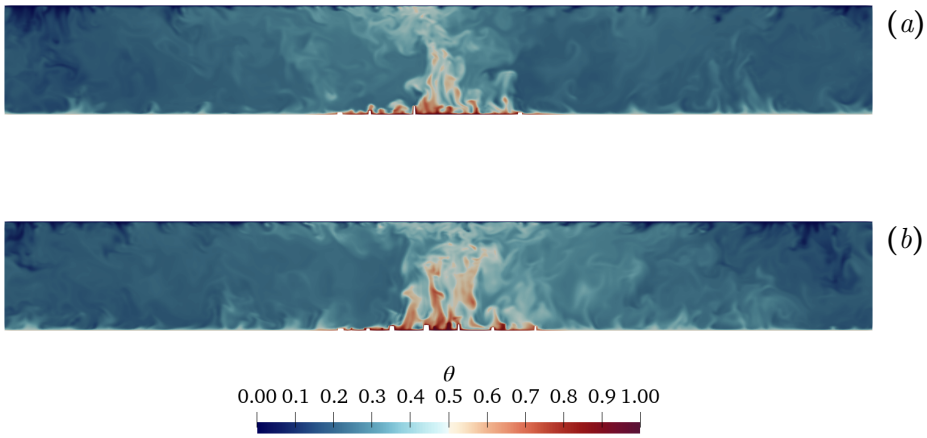

Figure 7.6: Instantaneous slices of dimensionless temperature θ in the x–z plane taken in the middle of the domain at 350 free-fall times. Panel (a) shows simulation 5 while (b) shows simulation 1.

7.3 Mixed convection

Moving to the mixed convection case, and following the same analysis procedure, we first evaluate the Stanton number as a function of the density coverage. In contrast to the pure convection case, where increasing density

generally enhanced heat transfer, mixed convection results reveal the opposite trend. Basically, the Stanton number tends to decrease as λ_p increases. For instance, when considering roughness elements with $\mathcal{AR}_z > 1.5$, it is possible to note how variation of 27% of the density coverage can lead to a decrease of the Stanton number of approximately 0.65% and 1.6% according to the value of ϵ adopted. When roughness elements with $\mathcal{AR}_z \sim 1.1$ are taken into account, two different behaviours emerge. In one scenario, an increase of 18% of λ_p, the ϵ adopted leads to a decrease of almost 5% of the Stanton number. In the other configuration, with the same λ_p, the Stanton increases by 2%. The general trend of the Stanton number can be explained by considering the combined effect of buoyancy and shear. As the canopy becomes more densely populated the blocking effect of the buildings increasingly attenuates the mean flow within the urban canopy. While in pure convection a higher density enhances buoyancy driven mixing, in mixed convection the reduction of shear production may dominate, leading to a net decrease in global heat transfer efficiency, see figure 7.8. This effect is more evident when considering $\mathcal{AR}_z \sim 1.1$ where the blocking and sheltering effect are more evident.

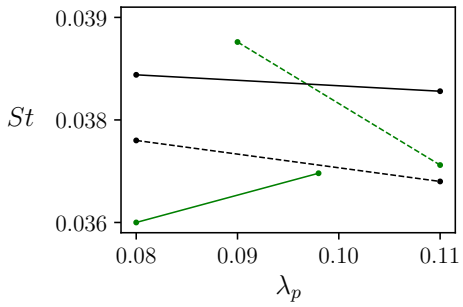

Figure 7.7: Stanton number St as a function of the plan area density λ_p, for different values of the smoothing parameter ϵ and vertical aspect ratio $\mathcal{AR}_z$. Green curves refer to $AR_z \sim 1.1$, and black curves to $AR_z \sim 1.68$. Green dashed lines correspond to $\epsilon \sim 0.48$, green solid lines to $\epsilon \sim 0.71$ while black dashed lines represent $\epsilon \sim 0.78$ and black solid lines $\epsilon \sim 1.08$.

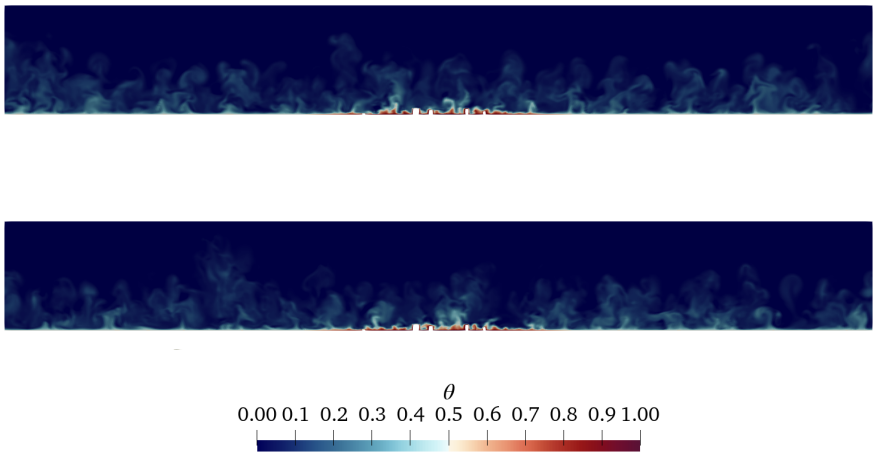

Figure 7.8: Instantaneous slices of dimensionless temperature θ in the y-z plane taken in the middle of the domain at 180 free-fall times. Panel (a) shows simulation 8 with a $\lambda_p = 0.11$ while (b) shows simulation 7 with a $\lambda_p = 0.09$.

As already observed in the pure convection regime, the influence of the vertical aspect ratio on the heat transfer is positive, as shown in figure 7.9 and in the slices 7.10. An increase of $\mathcal{AR}_z$ of almost 35% leads to an enhancement of the Stanton number of of about 3%, one order of magnitude higher respect the corresponding case in pure convection where for the same increase in aspect ratio case, resulted in only 0.29% gain of the Nusselt number.

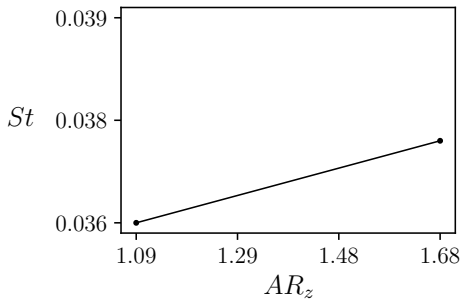

Figure 7.9: Stanton number St as a function of the vertical aspect ratio $\mathcal{AR}_z$ for different values of the plan area density λ_p and the smoothing parameter ϵ. Black solid line refers to $\lambda_p \sim 0.08$ $\epsilon \sim 0.73$.

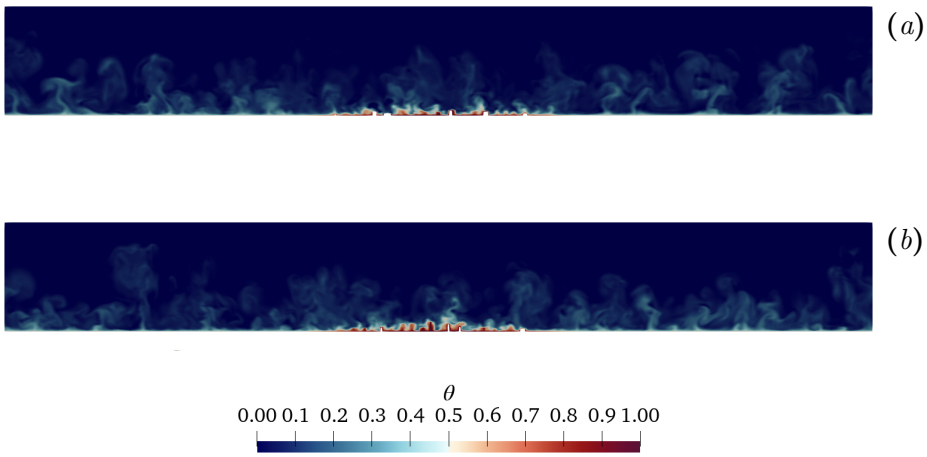

Figure 7.10: Instantaneous slices of dimensionless temperature θ in the y-z plane taken in the middle of the domain at 180 free-fall times. Panel (a) shows simulation 3 with $\mathcal{AR}_z = 1.09$ while (b) shows simulation 5 with $\mathcal{AR}_z = 1.68$.

To conclude, figure 7.11 reports the Stanton number as a function of ϵ, the radial smoothing and figure 7.12 shows two instantaneous slices, as reference for its effect. In this case, it can be observed that by lowering ϵ, thus generating more peaked city configurations, where taller buildings

are concentrated near the city centre and building heights rapidly decrease with radial distance configurations, reduces the heat transfer efficiency for both for both density coverage considered, in contrast to the Stanton trend shown in figure 7.7. This reduction is more evident for denser canopies, the red line in figure 7.11, suggesting that stronger radial smoothing intensifies the blocking effect and so heat transport efficiency.

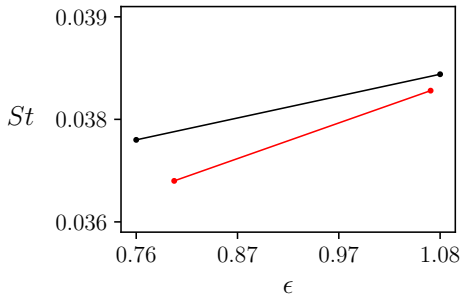

Figure 7.11: Stanton number St as a function of the smoothing parameter ϵ for different values of the plan area density λ_p and the vertical aspect ratio $\mathcal{AR}_z$. Black solid line refers to $\lambda_p \sim 0.08$ and $\mathcal{AR}_z \sim 1.68$ while red solid line corresponds to $\lambda_p \sim 1.1$ and $\mathcal{AR}_z \sim 1.67$.

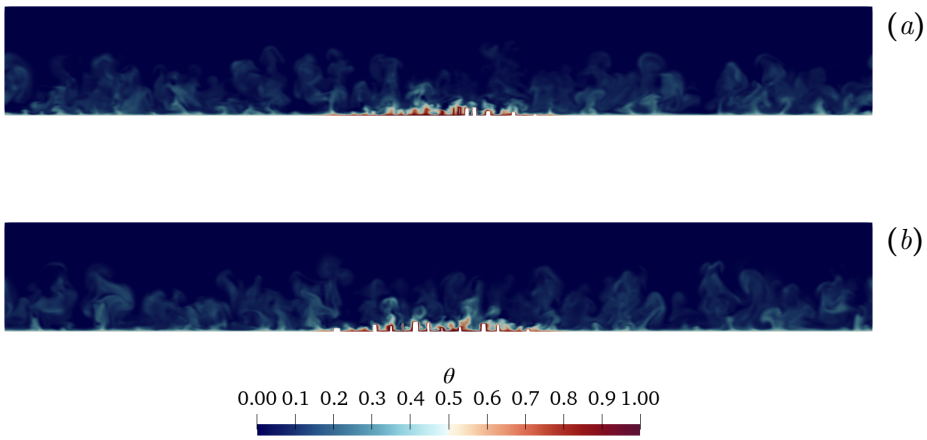

Figure 7.12: Instantaneous slices of dimensionless temperature θ in the y-z plane taken in the middle of the domain at 180 free-fall times. Panel (a) shows simulation 6 with $\lambda_p = 0.11$ and $\epsilon = 0.8$ while (b) shows simulation 1 with $\lambda_p = 0.08$ and $\epsilon = 1.08$.

7.4 Discussion on the parametric behaviour

At this point, it is useful to recap and highlight the main findings of the parametric study. The three geometrical parameters considered, surface density coverage λ_p, vertical aspect ratio $\mathcal{AR}_z$, and radial smoothing parameter ϵ, play a significant role in both pure and mixed convection regimes, although their influence differs, depending on the transport mechanisms. Regarding the effect of the density coverage λ_p, two behaviour emerge. In the pure convection case, the Nusselt number increases with increasing density coverage, especially for $\epsilon \sim 1$. In fact, with a strong radial smoothing applied, $\epsilon < 1$, roughness elements at the periphery can be easily trapped into the thermal boundary layer thickness and reduce thermal exchange, see Zhang et al. (2018) for the definition of a critical roughness height, although pyramidal roughness elements are considered or Tisserand et al. (2011). Assuming a linear trend as shown in figure 7.1, where Nu increases from 17.225 to 17.72 when λ_p varies from 0.08 to 0.11, a further extrapolation up to $\lambda_p = 0.16$ would lead to an estimated $Nu \approx 18.55$, an increase of 7.7% of the starting value. In contrast, when wind effects are included, the overall heat transfer performance is governed by the balance between shear produc-

tion and buoyancy driven transport. In this case, increasing urban density does not necessarily imply enhanced thermal exchange. Indeed, between $\lambda_p = 0.08$ and $\lambda_p = 0.11$, the Stanton number decreases by approximately 0.65%. Assuming again a linear trend, an increase up to $\lambda_p = 0.16$ would correspond to an estimated reduction of about 1.7% relative to the $\lambda_p = 0.08$ case. This reduction can be attributed to the blocking and sheltering effects induced by denser canopies which prevent flow penetration and weakens shear driven transport within the urban site made by staggered, and non homogeneous buildings. Examples also of numerical simulations present in the literature Jiang et al. (2008) and Coceal et al. (2006) show that the wind speed inside the canopy is inversely proportional to λ_p.
Concerning the vertical aspect ratio, its effect is positive in both regimes. An increase in $\mathcal{AR}_z$ enhances buoyancy production in pure convection and amplifies shear production in mixed convection, with a more pronounced impact in the latter. The larger percentage increase observed in the Stanton number for the same variation of $\mathcal{AR}_z$ indicates that, in mixed convection, vertical elongation of the buildings not only strengthens buoyancy transport but also promotes momentum redistribution above the canopy, thereby amplifying the overall heat transfer efficiency. This is also confirmed experimentally in Makedonas et al. (2021) where flow penetration is more evident when considering canopies characterized by buildings of different heights, even if in this case a much denser canopy is considered without the effect of buoyancy. The effect of the radial smoothing, ϵ, the last parameter, appears coupled with the canopy configuration. When wind is introduced, a clearer trend is observed: decreasing ϵ, thus generating a more peaked city profile, leads to a reduction of the Stanton number for both density levels considered. This suggests that stronger radial concentration enhances flow obstruction and limits shear penetration, independently of the coverage ratio.

To conclude, it is important to note that a deeper understanding of these mechanisms would require additional simulations, ideally varying one parameter at a time from a reference configuration. Moreover, the linear trends assumed in the present extrapolations should be interpreted with caution, as non-linear effects may arise outside the investigated parameter range.

Chapter 8

Conclusions

In the present thesis work, we propose a novel and general framework to generate controlled idealised urban patterns using a minimal set of five morphological parameters. The proposed parameterisation captures key geometrical characteristics of urban canopies, including coverage density, average building height, plan and vertical aspect ratios, and spatial distribution, which are quantities that can be directly derived from real urban layouts. The developed methodology enables the generation of heterogeneous urban patterns composed of hexahedral buildings, each characterised by distinct dimensions and orientations. Despite this, the resulting configuration statistically satisfies the prescribed global morphological parameters, which uniquely identify the urban morphology.

For the first time, a Direct Numerical Simulation (DNS) of a reference configuration defined by the parameter set $(N, \lambda_p, \mathcal{AR}_p, \mathcal{AR}_z, \epsilon) = (1963, 0.08, 1.7, 1.68, 1.08)$, corresponding to 176 buildings, representative of a moderately dense small town, was performed to investigate the fundamental mechanisms governing turbulent convective heat transfer over complex surfaces. In particular, non homogeneous temperature boundary conditions were imposed on both the ground and the roughness elements in order to reproduce a nocturnal urban heat island scenario under summer conditions. This configuration allowed for the detailed characterisation of buoyancy-driven large-scale circulation patterns, mean flow organisation, and turbulent mixing processes arising from the interaction between morphological heterogeneity and buoyancy.

The results show that the dominant flow feature is a large convective structure whose scale is comparable to the city size, resulting from the clustering of smaller thermal plumes originating within the canopy. This large-scale thermal structure, which acts as the principal carrier of heat, also generates a LSC of toroidal shape, whose ascending branch develops from the warmer urban regions and is sustained by a radially inward boundary layer transporting cooler air from the surrounding rural areas towards the city centre. This mechanism further implies that scalars released within the city, such as pollutants, are preferentially advected toward the central region be-

fore being redistributed vertically by the updraft. Within this framework, the thermal plume represents the most energetic region of the flow. The largest temperature fluctuations occur within the urban region, for $r \leq 25$ ($r\langle \ell_z \rangle_b / R \leq 1$), where their magnitude reaches approximately 20% of the maximum imposed temperature difference. A deeper analysis of the heat fluxes further clarifies the transport mechanisms governing the urban heat island. The total heat flux exhibits a predominantly inward radial component over most of the domain ($r \leq 80$, $r\langle \ell_z \rangle_b / R \leq 3.2$), converging toward the urban core where it is subsequently advected upward along the ascending branch of the large-scale circulation. However, turbulent heat flux displays an opposite radial tendency, reflecting its intrinsic role in enhancing mixing between dynamically distinct regions. By promoting heat exchange from warmer to cooler areas, turbulent transport reduces thermal gradients and contributes flow homogenisation, a mechanism that is directly relevant for understanding urban heat island mitigation processes.

The DNS results were used as a reference to evaluate two coarse-grained approaches, in particular an Implicit LES (ILES) and a Wall Adapting Local Eddy-viscosity (WALE) LES. The purpose of this comparison was to derive practical guidelines for high-fidelity coarse-grained simulations in urban climate studies, where computational cost represents a critical constraint. Both approaches successfully reproduce the large-scale flow organisation and the overall distribution of mean temperature and velocity fields confirming that reduced order simulations can retain the principal dynamical features of the system. However, differences emerge within the urban canopy. The WALE approach provides a more accurate representation of the mean temperature field, particularly in regions between adjacent buildings where strong thermal gradients develop, owing to the explicit subgrid-scale closure and enhanced near-wall resolution. At the same time, it exhibits a more dissipative behaviour in the momentum field, leading to a systematic underestimation of turbulent fluctuation levels. In contrast, the ILES approach tends to overpredict the mean temperature within the canopy and to generate a slightly stronger large-scale circulation. The absence of an explicit subgrid-scale model reduces artificial dissipation and partially preserves fluctuation intensity, although at the expense of thermal accuracy. From a best-practice perspective, the choice of modelling strategy should depend on the objectives of the study: applications requiring accurate near-wall resolution and detailed canopy-scale mixing favour WALE, whereas investigations focused on large-scale circulation trends or computationally demanding parametric campaigns may reasonably rely on ILES.

In the second part of this work, the reference urban configuration was

analysed under mixed convection condition, characterised by a Richardson number Ri ~ 1, thus accounting for the combined effects of buoyancy and an externally imposed cooler inflow interacting with the urban canopy. The introduction of a mean wind, significantly alters the flow organisation compared to the purely convective case. In the streamwise direction, elongated thermal streaks develop at the bottom boundary, indicating the dominance of shear driven transport mechanisms superimposed on buoyancy-induced motion. At urban scale, the incoming colder wind enhance a downstream heat advection, generating a longitudinal thermal wake extending over a distance comparable to the city size, and characterized by mean temperature reaching 35% of the maximum temperature difference in the domain, highlighting the efficiency of longitudinal heat transport and the effect of advection in reshaping the urban heat island structure. As a result, lower temperatures are observed on the windward side of the city, while the central and leeward portions of the canopy exhibit higher mean temperature levels.

In conclusion, a parametric study was conducted in order to understand the role of plan area density λ_p, vertical aspect ratio AR_z and ϵ the coefficient control- ling the radial height distribution, in shaping the urban climate. Eight different urban configurations were analysed under both pure and mixed convection setups. The results indicate that in both regimes, buildings with vertical aspect ratio $AR > 1$ enhance heat transfer efficiency. In pure convection, this effect is associated with increased buoyancy production, whereas in mixed convection it amplifies shear production and strengthens the interaction between mean flow and canopy geometry. The influence of plan area index, λ_p, depends on the flow regime considered. Under pure convection, increasing λ_p leads to a corresponding increase in the Nusselt number. In contrast, in mixed convection, the Stanton number decreases as λ_p increases, primarily due to the enhanced blocking effect of buildings, which progressively attenuates the mean flow within the urban canopy. For configurations characterised by $\mathcal{AR}_z > 1.5$ and $\epsilon \sim 0.48$, a 27% increase in λ_p results in a 2.76% increase in the Nusselt number and a 0.65% reduction in the Stanton number when comparing the two flow regimes. The effect of ϵ by contrast, is more strongly coupled with the urban configuration. Under mixed convection conditions, reducing ϵ , corresponding to a more peaked city profile, leads to a decrease in the Stanton number, regardless of the density factor considered. This behaviour differs from the purely convective case, where the response depends on λ_p. At lower density, stronger radial smoothing concentrates taller buildings in the central region, where temperature gradients are higher. As ϵ increases and the height distribu-

tion becomes more uniform, peripheral buildings do not generate sufficient additional mixing, resulting in a slight reduction in global heat transfer efficiency. On the contrary, for higher plan area density the trend reverses, leading to a moderate enhancement of heat transfer.

To conclude, the innovative and versatile framework developed in this thesis provides the basis for future investigations on urban climate flow dynamics.

Appendix

Appendix A

Moist Raileigh-Beńard convection

During my PhD, I conducted additional research activities within the framework of a Master's thesis that I co-supervised. In this appendix, I present the results of a study on moist Rayleigh–Bénard convection (Zadro, 2025).

A.1 Moist Rayleigh-Bénard convection

It is widely known that clouds play a fundamental role in the Earth's climate system, profoundly affecting both weather patterns and long-term climate dynamics (Stephens, 2005). By modulating the radiative balance and controlling vertical fluxes of heat, water vapour, and momentum, clouds serve as key agents in Earth's energy and hydrological cycles (Muller and Abramian, 2023). However, due to their complex, multiscale, multiphase nature and high sensitivity to initial and boundary conditions, their representation in climate models remains a major source of uncertainty (Arakawa, 2004). These challenges require the use of idealized systems with the goal of isolating the core physical processes involved in moist convection and cloud formation. In this regard, the canonical model for buoyancy-driven turbulence, the Rayleigh–Bénard convection setup (RBC), can be extended to include moisture and latent heat release, becoming then the so called moist Rayleigh–Bénard convection (MRBC) (Pauluis and Schumacher, 2010),(Weidauer et al., 2010). This work, following Pauluis and Schumacher (2011), investigates Moist turbulent Rayleigh–Bénard convection under conditionally unstable conditions by direct numerical simulations of an idealized setting, where a piecewise linear thermodynamic model, following Bretherton's framework, is used for describe the buoyancy fields, represented through two scalar fields, dry and moist buoyancy, with condensation that occurs through a threshold condition (Bretherton, 1987).
Hereafter, RBC will denote the classical dry Rayleigh–Bénard configuration,

to distinguish it from the moist Rayleigh–Bénard case (MRBC).

A.2 Governing equations of moist Rayleigh-Bénard convection

The simplified approach, introduced by Bretherthon, can be used to study the challenging scenario of atmospheric buoyancy flow. By expressing the thermodynamic properties of moist air as function of entropy, pressure and total water content, the full set of governing equations are derived. For brevity, only the final non dimensional form is reported here; the full derivation can be found in (Zadro, 2025).

$$\frac{\partial u_i}{\partial x_i} = 0 \tag{A.1a}$$

$$\frac{\partial u_i}{\partial t} + u_j \frac{\partial u_i}{\partial x_j} = -\frac{\partial p}{\partial x_i} + \sqrt{\frac{Pr}{Ra_M}} \frac{\partial^2 u_i}{\partial x_j \partial x_j} + B\hat{g}_i \tag{A.1b}$$

$$\frac{\partial M'}{\partial t} + u_j \frac{\partial M'}{\partial x_j} = \frac{1}{\sqrt{PrRa_M}} \frac{\partial^2 M'}{\partial x_i \partial x_i} + \delta_{i3} u_i \tag{A.1c}$$

$$\frac{\partial D'}{\partial t} + u_j \frac{\partial D'}{\partial x_j} = \frac{1}{\sqrt{PrRa_M}} \frac{\partial^2 D'}{\partial x_i \partial x_i} + \frac{Ra_D}{Ra_M} \delta_{i3} u_i \tag{A.1d}$$

Here u and p are respectively the velocty and the pressure field, δ is the Kronecker delta and D' and M' are deviation from the linear profile of the dry buoyancy $\bar{D}$ and moist buoyancy $\bar{M}$. B indicates the buoyancy term, expressed as $B = max[M, D - N_s^2 z]$ where N_s is the moist Brunt-Väisälä frequency thus the angular frequency of a particle when subjected to vertical displacement within a statically stable environment. In this formulation, contrary to the RBC, there are two Rayleigh number: the dry Rayleigh number Ra_D and the moist Rayleigh number Ra_M, which quantify the driving of the unsaturated and saturated fields D and M, respectively.

$$Ra_D = \frac{H^3(D_0 - D_H)}{\nu\alpha} \quad Ra_M = \frac{H^3(M_0 - M_H)}{\nu\alpha} \tag{A.2}$$

where H is the height of the vertical domain, the footnotes $0, H$ stands for quantities evaluated at the domain bottom and at the top plate respectively. As will be discussed in the following paragraphs, saturated regions, driven by the moist buoyancy field, $B = M$, exhibit strong turbulent activity, whereas dry buoyancy corrected by the background stratification, $B = D - N_s^2 z$,

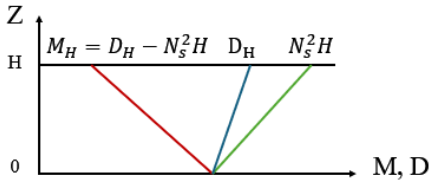

Figure A.1: Vertical profile of moist buoyancy (red), dry buoyancy (blue) and Brunt-Vaisala frequency (green) in the Kuo-Bretherton regime

which characterizes unsaturated areas, has a lower turbulent activity and do not support cloud formation. In order to correctly set up the simulations, it is also important to clarify the meaning of the conditionally unstable regime, which is the case of interest for moist convection. This regime occurs when the atmosphere is stable with respect to unsaturated parcels and unstable with respect to saturated parcels, corresponding to $Ra_D < 0$ and $Ra_M > 0$. Depending on the relative stability of the unsaturated and saturated states, several unstable regimes can be identified, such as the Kuo–Bretherton regime, the one considered in this study. In this regime, the equilibrium state lies at the onset of saturation, i.e, $\bar{M}(z) = \bar{D}(z) - N_s^2 z$, where $\bar{(\cdot)}$ stands for mean quantities. This also means $Ra_D^{KB} = Ra_M - Ra_{BV}$ as illustrated in figure A.1, where Ra_{BV} is the Brunt-Väisälä Rayleigh number, condition used to derive different conditionally unstable regimes defined as:

$$Ra_{BV} = \frac{N_s^2 H^4}{\nu \alpha} \tag{A.3}$$

A.3 Numerical method and flow settings

Two direct numerical simulations were performed using CaNS (Costa, 2018). The original version of the code, based on the Boussinesq approximation, was modified in the computation of the buoyancy term and in the Runge–Kutta time integration subroutine to consistently solve the modified set of equations A.1d. The two simulations differ only in the horizontal spatial resolution, with grid sizes $(n_x, n_y, n_z) = (1024, 1024, 129)$ and $(2048, 2048, 129)$, respectively. In the following, only the results obtained with the higher-resolution simulation are discussed. The domain dimensions and the corresponding flow parameters are reported in tables A.1 and A.2. Uniform grid spacing is adopted in the horizontal direc-

tions (x, y), whereas in the wall-normal direction z a hyperbolic tangent stretching is applied to ensure enhanced resolution near the two plates, where the largest gradients occur. With this choice, the resolution satisfies $\eta_{k,\max}(z)/\Delta_{x,y} = 1.2$ inside and $\eta_{k,\max}(z)/\Delta_{x,y} = 0.34$ outside the cloud regions. Along the wall-normal direction, $\eta_{k,\max}(z)/\Delta z(z) = 0.25$ inside and $\eta_{k,\max}(z)/\Delta z(z) = 0.1$ outside the cloud regions. The Kolmogorov scale is computed as $\eta_k = (Pr/Ra_M)^{3/8}\epsilon^{-1/4}$. The computational domain is characterized by an aspect ratio $AR = W/H = 64$, which is sufficiently large to ensure statistically steady and spatially well-developed moist convection.

$L_x \times L_y \times L_z$	$nx \times ny \times nz$
$64H \times 64H \times 1H$	$2048 \times 2048 \times 129$

Table A.1: Parameters of the simulation. The domain dimensions express as a function of the reference length, the heigth of the domain H

Pr	Ra_M	Ra_D	Ra_{BV}	N_s^2
0.7	3.73×10^5	-1.24×10^5	4.97×10^5	4

Table A.2: Flow parameters

To simulate an infinite horizontal domain, for both velocity and scalars fields periodic boundary conditions are applied at the lateral side walls, while on the top and bottom plates, free-slip boundary conditions are set for the velocity field and a Dirichlet boundary condition for scalars fields, $M_0 = D_0 = 0$ while $D_H = 1$ and $M_H = -3$. Additional noise is applied on both scalar fields to trigger transition. Velocity and scalar fields, after an initial transient, are collected for a period of $\tau = 115$ times, the yellow region in figure A.2, with a time interval of $\Delta\tau = 5$.

A.4 Results

A.4.1 Flow topology

The structure and the statistical properties of MRBC are significantly different from the classical RBC. In dry convection, the absence of moisture-driven buoyancy effects typically results in simpler and more symmetric convective thermal structures, the so called thermal plume, without the

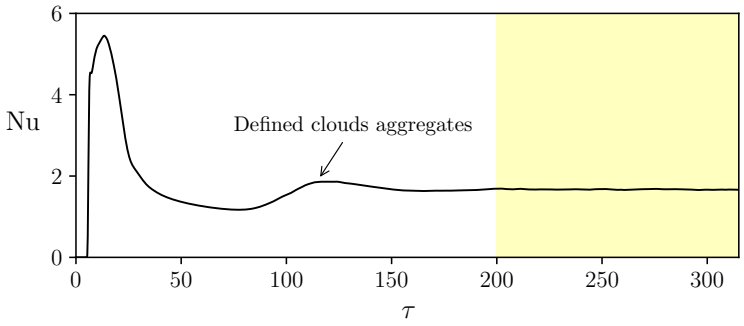

Figure A.2: Nusselt evolution in time

persistent localization and aggregation phenomena as for clouds surrounded by unsaturated air, observed here.

Moving to the MRBC case, following the evolution of the Nusselt number, figure A.2 is it possible to observe different flow arrangement of the moist buoyancy field, before reaching stationarity. At the beginning, due to the noise imposed, when the Nusselt number is at his highest values, the upper part of the domain display a cluster of moist structures which is subsequentially followed by a reduction of the Nusselt number, and so the convective activity, with the appearance of small isolated clouds, figure A.3 (a-b). After this stage, in which prevail dry buoyancy, some localized convective activity produces in addition to an increase of the Nusselt number, the formation of clearly defined cloud aggregates surrounded by unsaturated regions. Once the system reaches stationarity, the mean buoyancy profiles remain essentially unchanged and the moist buoyancy field exhibits clear clouds pattern as shown in figure A.3(c-d). At equilibrium, moist buoyancy becomes a relevant driving mechanism for convective activity, see figure A.3(a), in the upper region of the domain, from $z > 0.6$ where clouds may undergo also to self aggregating phenomena. This trend characterize the conditionally unstable regime where convective structures, given also by the boundary conditions applied at the top boundary, are encourage to self-organize into larger and stable configurations.

The analysis of the followings quantities is done by exploiting also conditional statistics, to differentiate between clouds region and dry region exploiting the diagnostic fields water content, $CW = max(M - D + N_S^2 z, 0)$. In this framework dry regions will be characterised by a null water content in contrast to cloudy areas with a positive water content.

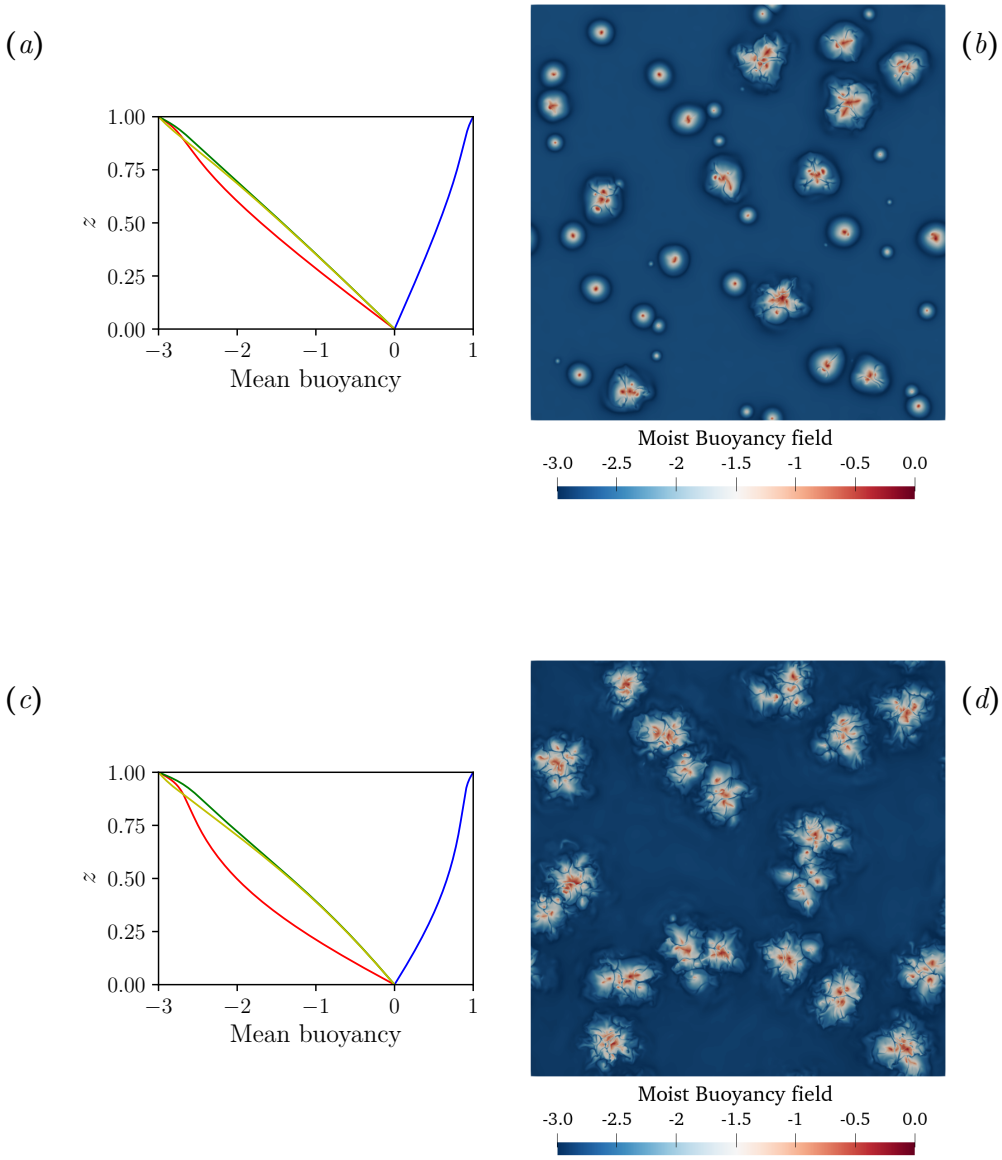

Figure A.3: Left column: (a) mean buoyancy profiles along the vertical direction for $\tau = 80$ and c) for $\tau = 300$. Dry buoyancy D (blue), total buoyancy B (dark green), moist buoyancy M (red), and dry buoyancy corrected by the background stratification, $D - N_s^2 z$ (light green); Right column: (b) instantaneous horizontal slice of the moist buoyancy field taken at $z = 0.9$ for $\tau = 80$ and (d) for $\tau = 300$.

A.4.2 Characterization of clouds

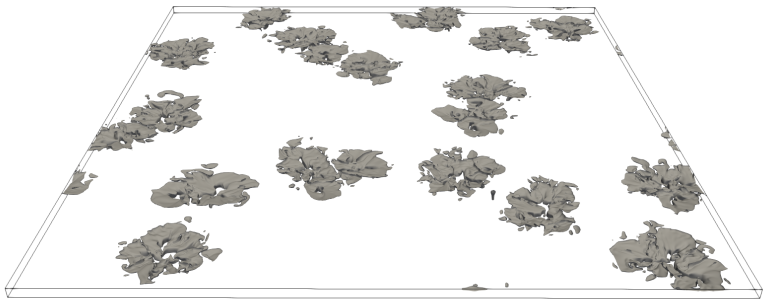

Figure A.4: Instantaneous 3D rendering of the cloud boundary, given by $M(\mathbf{x}, t) - (D(\mathbf{x}, t) - N_s^2 z) = 0$

A better description of the flow topology also leads to a deeper analysis of the main feature of MRBC, i.e. clouds, figure A.4. Considering the vertical distribution of the plane averaged cloud fraction and liquid water content, figure A.5(a–b), the lower part of the domain is characterised by vertically elongated and relatively narrow structures, occupying only about 1.5% of the horizontal plane. For $z > 0.5$, where most of the liquid water content is concentrated, these structures progressively broaden and expand horizontally, reaching a maximum coverage of approximately 23% of the horizontal cross-section. This widening results from the combined effects of enhanced buoyant ascent and increased lateral entrainment at higher levels. In addition to plane averages, conditional statistics are employed to separately analyse moist and dry contributions, allowing for a clearer interpretation and characterisation of saturated and unsaturated regions in the horizontal (x–y) planes. The results shown in figures A.6(a–b) and A.7 further support and refine the cloud structure described above. In particular, figure A.7(a) highlights the effective cloud shape: a narrow column originating at the bottom plate, widening in the central region of the domain, and narrowing again near the top boundary. The liquid water content within these structures is primarily concentrated in the upper portion of the domain, approximately within $0.75 < z < 0.95$. As expected from their definition, the contributions of both liquid water content, CW, and cloud fraction CF, vanish in the dry region. Finally, to avoid misleading interpretation of figure A.6, it should be noted that although $CF = 100\%$ near the top boundary,

this does not imply that the horizontal plane is entirely filled with clouds due to the imposed boundary condition, $\langle CW(H)\rangle = 0$, consistently with the definition $CW = \max(M - D + N_S^2 z, 0)$.

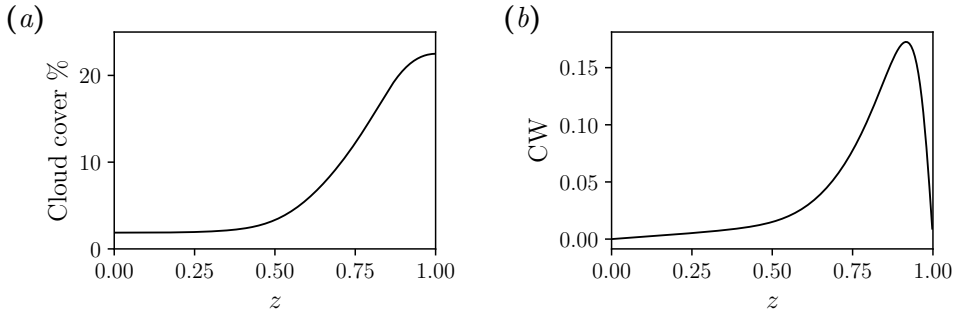

Figure A.5: Meanvertical profiles of (a) water content and (b) cloud cover.

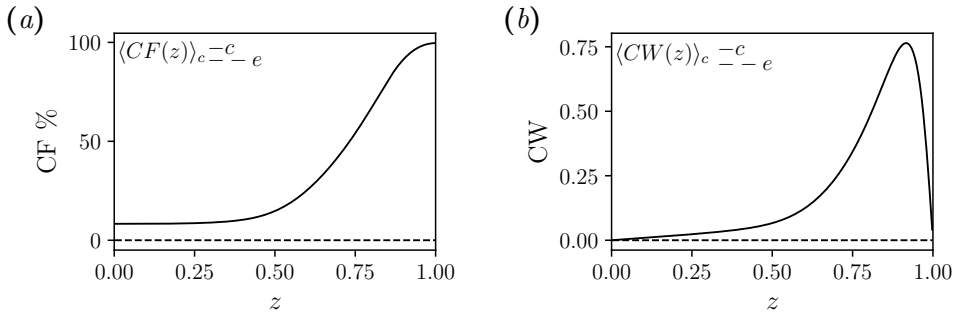

Figure A.6: Conditioned profiles of (a) cloud fraction, CF, which is equal to 1 when $CW > 0$, and (b) water content. Solid lines indicate conditional statistics computed inside, dashed lines indicates conditional statistics computed outside cloud regions

A.4.3 Statistical analysis

By extending the analysis to conditional statistics, it is possible to examine the distinct behaviour of the buoyancy fields figure A.8(a). The mean buoyancy profiles in the cloud-free region (dashed lines) display an approximately linear trend, consistent with a stably stratified environment. This behaviour suppresses turbulent motions and maintains a relatively stable regime. In contrast, the profiles within cloudy regions (solid lines) are clearly non-linear, reflecting the strong mixing processes induced by turbulent moist convection. Moreover, the convergence of $\langle M(z)\rangle$ and $\langle B(z)\rangle$ for

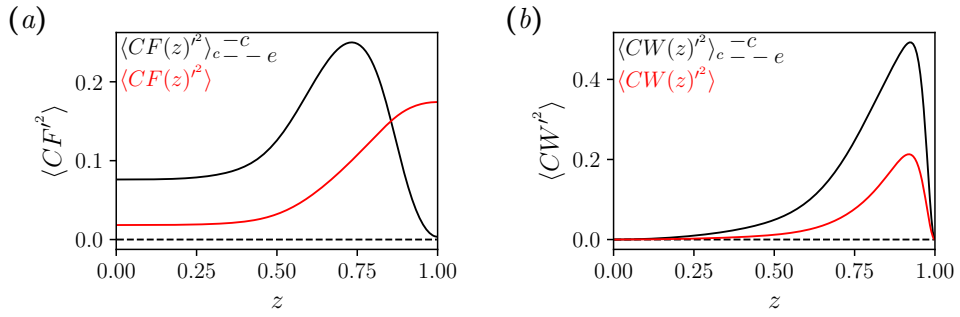

Figure A.7: Vertical variance profiles of (a) water content and (b) cloud cover. Solid lines indicate conditional statistics computed inside, dashed lines indicates conditional statistics computed outside cloud regions and red lines stands for non conditional profiles

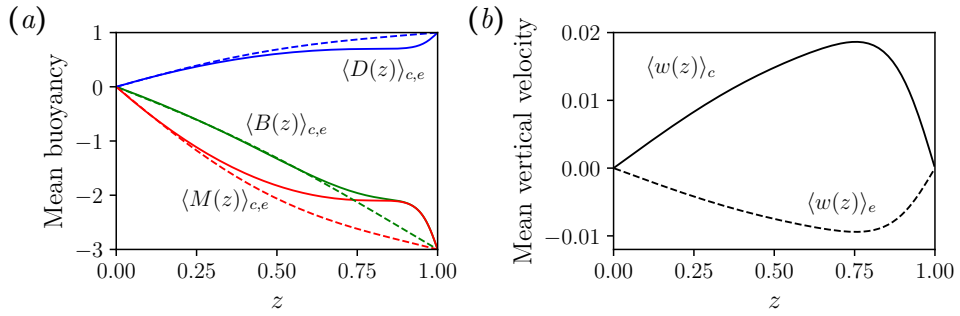

Figure A.8: Mean plane profiles of (a) buoyancy (b) vertical velocity. Solid lines indicate conditional statistics computed inside cloud regions while dashed lines indicates conditional statistics computed outside cloud regions.

$z \gtrsim 0.8$, up to the top boundary, highlights the dominant role of buoyancy-driven convection and its impact on cloud dynamics in the upper part of the domain. The large-scale circulation within the domain is revealed by the conditional statistics of the mean vertical velocity shown in figure A.8(b). A simple plane average in the horizontal directions would yield $\langle w\rangle = 0$ at all heights. However, the conditional averages show a clear partition of motion: moist air rises within cloud regions, with a global maximum of the mean vertical velocity at $z \simeq 0.77$, while compensating downward motion occurs in the unsaturated environment, where $\langle w\rangle_e$ remains negative throughout the domain. This separation of upward and downward motions reflects the physically consistent coupling between buoyancy, moisture, and momentum transport: moist convection drives upward mass flux within clouds, while

the surrounding unsaturated air provides subsidence to ensure mass balance. Although not shown here, the probability density function (PDF) of w exhibits a pronounced peak at negative values and a right-skewed tail, indicating positive skewness. This confirms the presence of stronger upward motions within clouds compared to the surrounding environment. In the classical dry Rayleigh–Bénard case (RBC), the skewness of w would instead be approximately zero, i.e. $Sk(w) \simeq 0$.

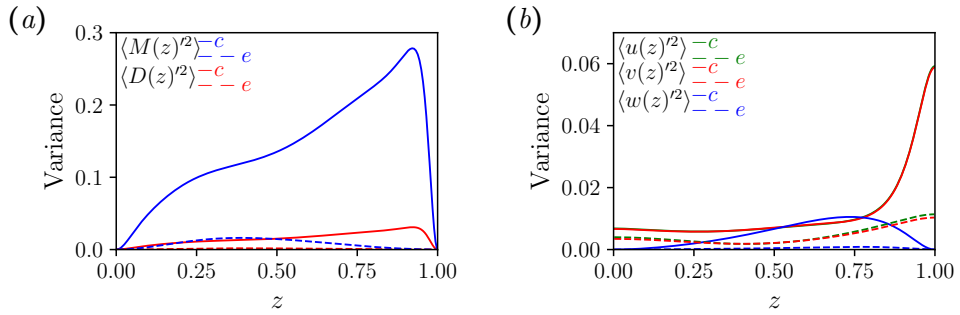

Figure A.9: Conditioned variances of (a) moist and dried buoyancy and (b) the velocity field. Solid lines indicate conditional statistics computed inside, dashed lines indicates conditional statistics computed outside cloud regions.

To further characterise the turbulent activity, it is necessary to examine higher-order statistics, such as variances. Figure A.9(a–b) reports the conditional variances of both buoyancy fields and velocity components. In the unsaturated regions, the profiles are nearly zero, indicating that these areas are only weakly active. In contrast, saturated regions exhibit significantly enhanced fluctuations. In particular, figure A.9(a) shows that the variance of the moist buoyancy field within cloud regions is several times larger than in dry regions, highlighting the intense turbulent mixing occurring in saturated areas. Regarding the velocity components, statistical homogeneity and isotropy in the two horizontal directions imply that $\langle u'^2 \rangle$ and $\langle v'^2 \rangle$ follow the same trend in both saturated and dry regions. Near the top plate, these horizontal components attain higher values than the vertical one due to the imposed boundary conditions. Conversely, $\langle w'^2 \rangle$ exhibits a pronounced maximum around $z \sim 0.75$, corresponding to the region of enhanced vertical motions associated with cloud broadening. Once again, considering the RBC case, we can see how moist convection, alters the statistical structures of the flow. In fact, even if the horizontal statistical homogeneity is retained, the formation of localized cloudy areas, characterized by high turbulent activity respect the surroundings, which in dry RBC would otherwise exhibit

symmetric temperature and velocity structures.

A.4.4 Conclusion

This thesis investigate moist turbulent Rayleigh–Bénard convection under conditionally unstable conditions by adopting a simplified set-up, using Bretherton's thermodynamic approach and the Boussinesq approximation. The use of conditional statistics was fundamental to have insight on cloud regions and unsaturated ones. One of the key phenomena detected was cloud self-aggregation at higher altitudes, eventually merging into persistent large-scale formations. This behaviour emphasised how moisture significantly influences convective patterns, contrasting sharply with the more uniform convection typically seen in RBC. Statistical analyses of the velocity and scalar fields also consistently showed highly localized turbulence and strong asymmetries, reinforcing the complexity moisture introduces into convective flows. Future studies could explore regimes at higher moisture content and Rayleigh numbers, investigate the effects of a variable Brunt–Väisälä frequency N_s, and incorporate more realistic thermodynamic formulations. It would also be of interest to examine how moisture interacts with additional environmental factors, such as wind shear or variable boundary conditions. Furthermore, applying conditional statistics to the turbulent kinetic energy budget could help clarify the pathways of energy transfer within saturated regions. In this context, filtering the velocity field may provide insight into whether cloud self-aggregation is predominantly driven by small-scale or large-scale turbulent motions beside their role. Finally, the influence of bottom-plate roughness distributions on cloud formation and organisation could also be systematically investigated.

Appendix B

Coanda effects in planar plumes

During my PhD, I conducted additional research activities within the framework of a Master's thesis that I co-supervised. In this appendix, I present the results of a study on the merging of two planar plumes (Speziali, 2024).

B.1 Introduction

Plumes belong to the class of buoyancy-driven free shear flows, in which fluid motion is generated by density variations under the action of gravity. These density variations may arise from thermal forcing or from the injection of a lighter fluid into a denser surrounding environment (Khan and Rao, 2023). Plumes are ubiquitous across a wide range of scales in both natural, such as volcanic eruptions or avalanches, and man-made environment, e.g. the vapour rising from smoke stacks. Depending on the condition at their release, in particular on the ratio between buoyant and momentum flux, plumes can be classified as "lazy", "pure" or "forced". In "lazy" plumes, this ratio is lower than one, meaning that buoyancy dominates over initial momentum, while for "forced" plumes is higher than unity. When buoyancy and momentum fluxes are of comparable magnitude, so when their ratio is equal to one, the plume is called "pure". Jets are forced plumes in case of no density difference between the surrounding environment and the injected fluid. Based on the geometrical shape of the buoyant source, plumes can by additionally subdivide as axisymmetric or planar. Axisymmetric plumes originate from circular sources and have been extensively investigated in the literature, both experimentally (Ezzamel et al., 2015; Shabbir and George, 1994) and numerically (Bhaganagar and Bhimireddy, 2020; Devenish et al., 2010). Planar plumes, which arise from elongated or horizontally distributed heat sources, have received comparatively less attention Van den Bremer and Hunt (2014). The study of plumes is crucial

in many different fields. In atmospheric and climate research, for instance, plume dynamics influence pollutant dispersion, boundary-layer mixing, and large-scale energy transport. A proper understanding of plume behaviour is therefore essential for improving air-quality predictions and climate models. The present thesis aims to investigate the physical mechanisms governing planar plumes and their mutual interaction by means of Direct Numerical Simulations. It is noteworthy to point out that our case, in contrast to the majority of literature examples where plumes are free to develop in elongated domain along the streamwise direction, we will deal with a confined plume due to the imposed domain dimension.

B.2 Morton-Taylor-Turner model

The modelling of turbulent plumes can be divided into two main approaches: microscopic and macroscopic (Hunt and Van den Bremer, 2011). The microscopic approach focuses on the numerical solution of the Navier–Stokes equations and on the characterization of turbulent phenomenology and entrainment, including the mixing processes and the spatial distribution of key quantities such as turbulent kinetic energy across the plume. On the other hand, the latter is based on the work of Morton et al. (1956), who develop a simplified theoretical model for the study of plumes, hereinafter referred as MTT (Morton-Taylor-Turner), valid whether or not Boussinesq approximation is it considered. The assumptions on the basis of this model are related to the rate of entrainment of the ambient fluid, the ratio between the density of the two fluids considered thus plume and environment, and the properties of the flow in the orthogonal direction to the plume. In this context, the mass conservation equation combined with the momentum and internal energy equation, B.1 are the starting points of the MTT model:

$$\frac{\partial \rho}{\partial t} + \nabla \cdot (\rho \mathbf{u}) = 0 \tag{B.1a}$$

$$\frac{\partial (\rho \mathbf{u})}{\partial t} + \nabla \cdot (\mathbf{u} \otimes \mathbf{u}) = -\nabla p + \rho \mathbf{g} \tag{B.1b}$$

$$\frac{\partial (\rho e)}{\partial t} + \nabla \cdot (\rho e \mathbf{u}) = -p \nabla \cdot \mathbf{u} \tag{B.1c}$$

where ρ is the fluid density, $\mathbf{u}$ the velocity vector, p the pressure field, e the internal energy per unit volume and $\mathbf{g}$ the gravitational acceleration vector. Considering a long thin and circular plume, doing time averaged

profiles of cross-stream vertical velocity and buoyancy, it was noted that when suitably scaled, the radial dependence of these quantities is independent of height. This self similar behaviour, is exploited in order to define the fluxes of mass G, volume Q and momentum M as a function of the wall normal coordinate by only considering the vertical velocity $w(z)$, the plume radius $b(z)$ and $\eta = \rho/\rho_a$ the ratio of plume and ambient density.

$$G = \eta w b^2 \tag{B.2}$$

$$Q = w b^2 \tag{B.3}$$

$$M = \eta w b^2 \tag{B.4}$$

Assuming that the flow considered is incompressible, integrating the system (B.1) along a cross section and applying the Boussinesq approximation, leads to:

$$\frac{d(\eta w b^2)}{dz} = 2 b u_e \tag{B.5}$$

$$\frac{d(w^2 b^2)}{dz} = g(1-\eta) b^2 \tag{B.6}$$

$$\frac{d(w b^2)}{dz} = 2 b u_e \tag{B.7}$$

where u_e is the horizontal entrainment velocity at the edge of the plume, that must be parametrized in order to close the system:

$$u_e = \begin{cases} \alpha w & \text{Boussinesq} \\ \alpha w \sqrt{\eta} & \text{non Boussinesq} \end{cases}$$

with α defined as entrainment coefficient. For the sake of brevity, the theoretical derivation of the MTT model solutions for the different plumes, is not reported here and can be found in Speziali (2024). It is important to emphasize that one of the main strengths of this approach lies in its flexibility: the governing equations can be readily extended to incorporate additional physical processes, such as ambient stratification or chemical reactions, provided that the entrainment closure is appropriately formulated.

B.3 Numerical simulation and flow setup

The analysis of two turbulent natural convection flows generated by heated planar sources, single and double, in a quiescent environment is presented below. Both simulations were performed using CaNS Costa (2018)

with minor modifications to incorporate the present configurations. In particular, starting from the original version of the code with the Boussinesq approximation, the subroutine responsible for imposing the thermal boundary conditions was adapted to allow the generation of planar slots at the bottom of the domain, with user-defined positions, dimensions, and number of sources. All simulations were carry out for a Grashof number, $Gr = Ra/Pr = 2{\cdot}10^7$ and for a given Prandtl number $Pr = 0.7$. The domain height was taken as the reference length, $H = 1$, and the width of the planar slots was set to $h = 2b_0 = H/10$, see figure B.1. The imposed temperature difference within the domain is defined as $\Delta\Theta = \theta_{source} - \theta_{amb} = 1$, where θ_{amb} denotes the ambient temperature prescribed throughout the domain, except at the planar source(s), where the temperature is fixed at θ_{source}. The relevant physical and geometrical parameters are summarized in tables B.1 and B.2.

Pr	Gr	ν	$\Delta\Theta$
0.7	$2 \cdot 10^7$	$7.07 \cdot 10^{-4}$	1

Table B.1: Physical parameters of the simulation

$Lx \times Ly \times Lz$	$nx \times ny \times nx$	H	h
$4H \times 4H \times 1H$	$1024 \times 1024 \times 356$	1	0.1

Table B.2: Computational domain and numerical resolution

A uniform spatial resolution is adopted along the two horizontal directions x and y, while a hyperbolic tangent stretching is used in the wall-normal direction to achieve a finer resolution near the walls and accurately capture the steepest gradients. With the Kolmogorov scale, $\eta_k = (\nu^3/\epsilon)^{1/4}$ computed a posteriori, the final resolution reads as follows ensuring an adequate discretization: $\eta_{k,max}(z)/\Delta z(z)_{min} \sim 3$ along the wall normal direction and $\eta_{k,max}(z)/\Delta x, y \sim 3$ along the two horizontal directions. To simulate an unlimited horizontal domain, periodic boundary conditions are applied in the cross-flow and spanwise directions for both velocity and scalar field. No-slip conditions are applied on the bottom wall, and free-slip conditions on the top wall for the velocity field. On the other side, for the scalar field at the bottom plate, the slots has the prescribed temperature difference $\Delta\Theta$ relative to the rest of the wall, which is maintained at a uniform tem-

perature, the same as the top plate. To complete, a zero normal pressure gradient is applied. Spatial discretization is based on a staggered second order finite different scheme, while integration in time is performed using a third order accurate Runge-Kutta method with a condition on a cfl = 0.95. Both simulations were carried out for almost 550 characteristic times and no disturb was applied to trigger transition. Once the statistically stationary state is established, after the initial transient is washed out, velocity and temperature fields have been collected in order to average among 50 non correlated time samplings for both single and double plume.

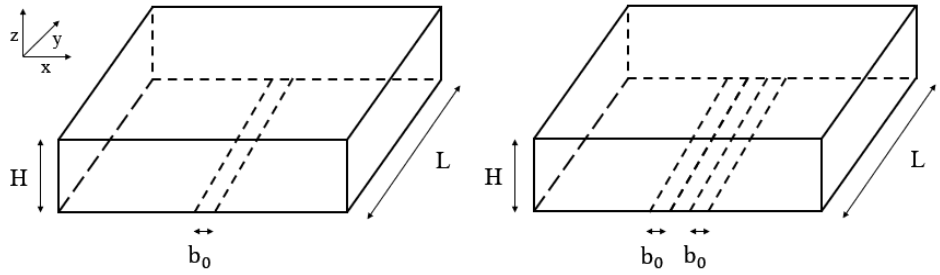

Figure B.1: Simulation domain configuration: (a) single plume (b) double plume.

B.4 Results

This section presents the main results obtained for the single-plume and double-plume configurations.

B.5 Single plume analysis

B.5.1 Flow pattern

Once a statistically stationary state is reached, the global flow structure is characterized by the development of a buoyant plume rising from the heated slot located at the bottom plate. The plume boundary is identified following the method proposed by Fanneløp and Weber (Fanneløp and Webber, 2003), where the plume radius b is defined as the radial distance from the plume axis at which $\langle W \rangle = \langle W_c \rangle e^{-1}$. Here, $\langle W_c \rangle$ denotes the mean vertical velocity evaluated along the slot centreline. The vertical evolution of the plume radius, figure B.2), reveals the presence of a necking phenomenon

in the vicinity of the source. This feature, commonly observed in both lazy and pure plumes (Hunt and Van den Bremer, 2011), corresponds to the location where the plume reaches its minimum cross-sectional area. In the present case, this occurs just above the buoyant source at $z/b_0 = 0.43H$, where b_0 is the half-width of the planar source.

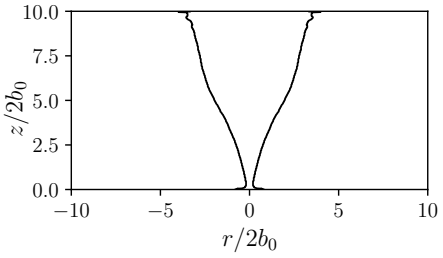

Figure B.2: Plume radius evolution along the vertical direction. The x and z coordinates are normalized by the slot length $2 * b_0$, two times the distance between the plume edge and the plume axis at $z = 0$.

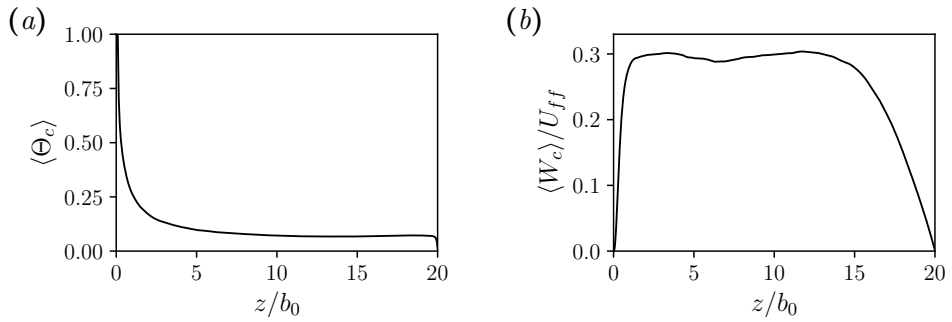

Figure B.3: Vertical profiles of normalized mean temperature (a) and mean vertical velocity along the centerline.

The footprint of the plume contraction is also evident in the mean vertical velocity computed at the centreline, $x = Lx/2$, figure B.3(b). As can be seen the flow immediately accelerates and reaches its highest value until it starts to decelerates under the influence of the top plate, in the last part of the domain height, when it diverges radially, due to the impose free-slip boundary condition. In contrast, the mean temperature profile evaluated along the centreline exhibits a different behaviour. The temperature attains its maximum at the bottom plate and rapidly decreases within the region $0 < z/b_0 < 2.5$. Beyond this height, it remains slightly positive throughout

the domain until reaching the top boundary, where the condition $\theta = 0$ is prescribed. For clarity, the subsequent analysis is divided into two regions: the near field ($0 < z/b_0 < 5$) and the far field ($5 \leq z/b_0 < 20$), in order to better highlight the distinct trends and flow characteristics in these two regimes.

B.5.2 Near field behaviour

Instantaneous slices of the temperature field taken in the $x-z$ plane, and zoomed at the source region can help to delineate the so called "near field behaviour", a laminar zone that extends from the source to the transitional region, before becoming turbulent. Figure B.4 (a-d), show four successive times of zoom extracts of length $(lx, lz) = (0.3, 0.25)$ and centred in the middle of the domain. In particular all of them present a hot column of fluid identified for $z < 0.05H$, with variable extension across the times. At $\tau = \tau_0$, figure B.4(a), the breakdown of the main column leads to enhanced mixing with mushrooms shape plumes, departing from it. The same scenario can also be observed in the following times, B.4 (b-c-d), where the swinging motion of the plume is also noted with respect to its axis. Another common feature observed in all instantaneous snapshots, is the presence of instabilities located at the source. Considering figure B.5, is it possible to note puffs, vortical structures, which develop on the heated source on both side of the plume axis, forming a thermal plumelet, called bulge that eventually entrain and surrounds the central ascending column Hattori et al. (2013). However, based on the selected time instants considered here, is not possible to clearly identify puffs along the vertical axis.

B.5.3 Far field behaviour

Moving the attention to the upper region of the domain, and considering the radial profile of the mean vertical velocity computed at different vertical coordinates $z/b_0 \in [5, 10, 15]$ B.11, it is possible to also analyse the behaviour outside the plume outline. As expected $\langle W \rangle$ has always a maximum in the core of the plume and decreases as it moves away from the centreline. In particular, by rescaling each velocity profile using the maximum velocity $\langle W(z)_{max} \rangle$ and the spatial coordinate with b at the height of the profile under consideration, it is possible note a self-similar behaviour, due to the collapsing of the curves. This collapse indicates that, within this flow region, quantities such as buoyancy and vertical velocity, when properly normalized, exhibit a universal transverse distribution that is independent

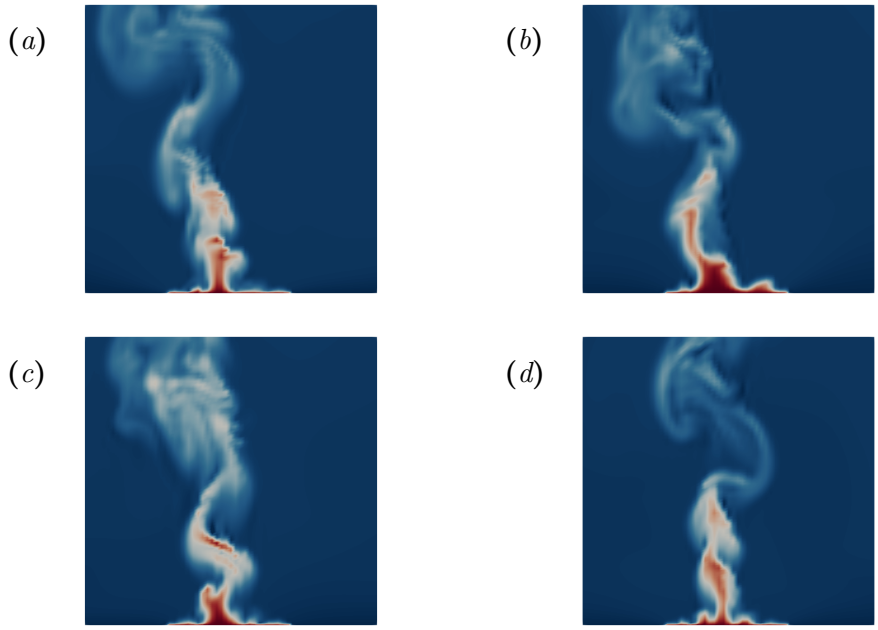

Figure B.4: Zoom in of the istantaneous temperature field, Θ, near the heated source region and its evolution over time: (a) $\tau = \tau_0$, (b) $\tau = \tau_0$+1,(c) $\tau = \tau_0 + 2$ and (d) $\tau = \tau_0 + 3$. Warm colours indicate high temperature, whereas cold colours indicate low temperature.

of the vertical position. Farther from the source, however, negative velocity peaks emerge, highlighting the presence of large-scale recirculation spanning the entire domain.

B.5.4 Two-point correlation

To measure the dimensions of characteristics structures, we can use the two-point correlations that for a fluctuating component of a generic flow variable along the homogenous direction y, as in our case, is defined as:

$$R_\gamma = \frac{\langle \gamma(x,y,z,t)\gamma(x,y+r_y,z,t)\rangle}{\langle \gamma(x,y,z,t)^2\rangle} \tag{B.8}$$

Figure B.7, reports the autocorrelations functions R_θ, R_u and R_w taken at $x = L_X/2$ and $z = H/2$ along the y direction. The autocorrelation of temperature fluctuations, B.7(a) has a slightly negative peak for $r_y/b0 \simeq 15$.

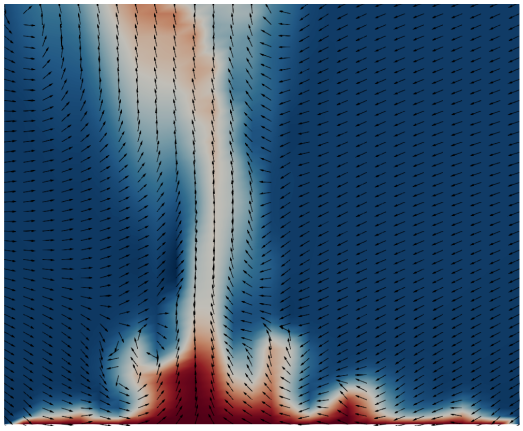

Figure B.5: Particular of the temperature field at $\tau = \tau_0 + 4$ with superimposed velocity vectors. Warm colours indicate high temperature, whereas cold colours indicate low temperature.

R_u, the autocorrelation of the cross-flow fluctuations, exhibit a negative peak located for $r_y = 40$, at the middle of the domain with a decorrelation length at $r_y/b_0 \simeq 19$. In contrast, the autocorrelation functions of the streamwise flow structures R_w, shows no negative values indicating that turbulent fluctuations of w are statistically not opposed in sign along the homogeneous direction.

B.6 Double plume analysis

We now extend the analysis to the case of two planar plumes, positioned symmetrically at a distance of from $2.5b_0$ the domain centreline. The statistical results are presented following the same methodology adopted for the single-plume configuration.

B.7 Flow pattern

Starting from the analysis of the mean quantities evaluated at the mid-plane of the domain, figure B.12, several differences with respect to the single-plume configuration can be observed. In the near-source region, the variation in the mean temperature profile, figure B.12(a), is primarily due to the lateral displacement of the two slots from the domain centre. The peak occurring at $z/b_0 \sim 1.7$ corresponds to the height at which the two

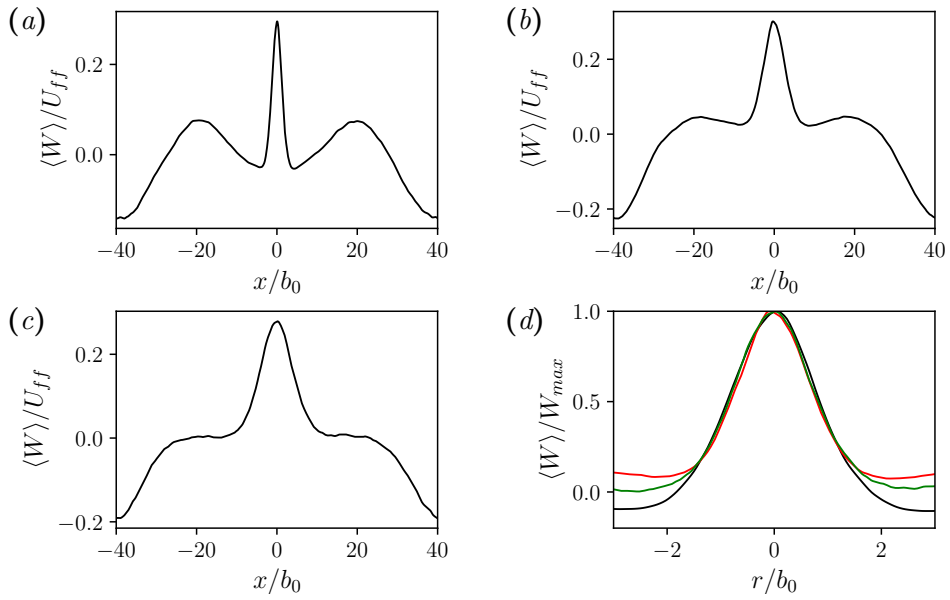

Figure B.6: Mean vertical velocity profile at different height along the cross-flow direction: (a) $z/b_0 = 5$, (b) $z/b_0 = 10$,(c) $z/b_0 = 15$ and (d) normalized vertical velocity profiles using the maximum velocity and the half-width of the plume at the height of the considered profile. Black curve $z/b_0 = 5$, red $z/b_0 = 10$ and green for $z/b_0 = 15$

plumes merge; above this location, their dynamics resemble those of a single plume. Figure B.12(b) shows the mean vertical velocity profile, which displays a markedly different behaviour compared to the single-plume case. In the near-source region, the velocity increases gradually, reaching a maximum around $z \approx 0.5H$. Beyond this height, the flow begins to be influenced by the presence of the top boundary, where the condition $\langle W \rangle = 0$ is imposed at $z = H$, leading to a progressive deceleration. Profiles of the mean vertical velocity at different heights are presented in figure B.10. Close to the source ($z/b_0 = 1$), a double positive peak can be observed, symmetrically displaced with respect to the centreline, indicating that the two plumes have not yet coalesced. In contrast, at higher elevations, figure B.10(b–d), the double-peak structure is replaced by a single central maximum, reflecting the merging process. After coalescence, the plume exhibits a tendency toward self-similar behaviour, analogous to the single-plume case. This merging process is also evident in the instantaneous temperature field (figure B.8), where the two plumes are seen to progressively bend toward the domain

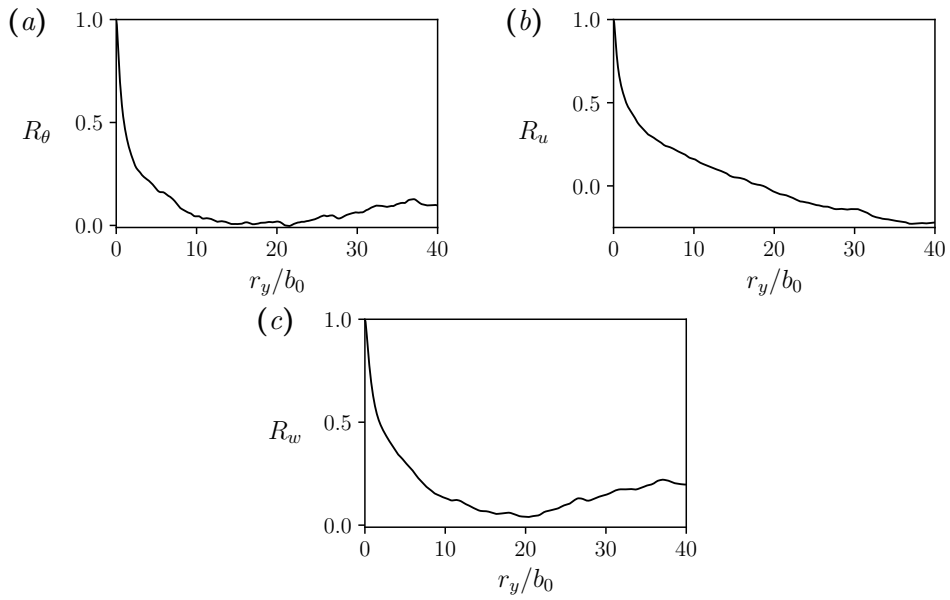

Figure B.7: Two points correlation functions along y: (a) temperature θ , (b) cross flow velocity u and (c) vertical velocity w

Figure B.8: Instantaneous temperature slice of the two plume simulations, zoomed at the source region.

centreline until they coalesce as a result of mutual entrainment, associated with the Coandă effect.

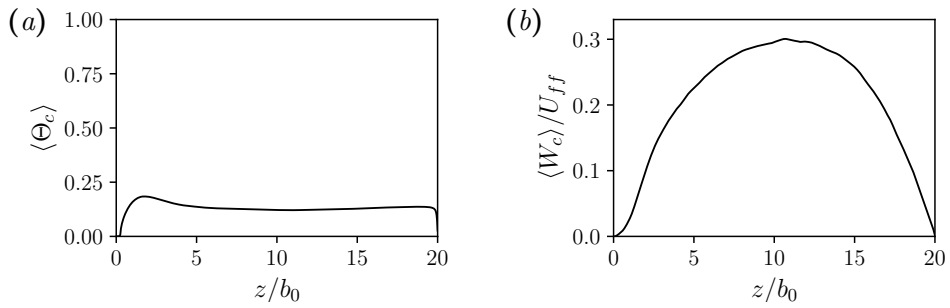

Figure B.9: Vertical profiles of normalized mean temperature (a) and mean vertical velocity along the centreline in double plume case

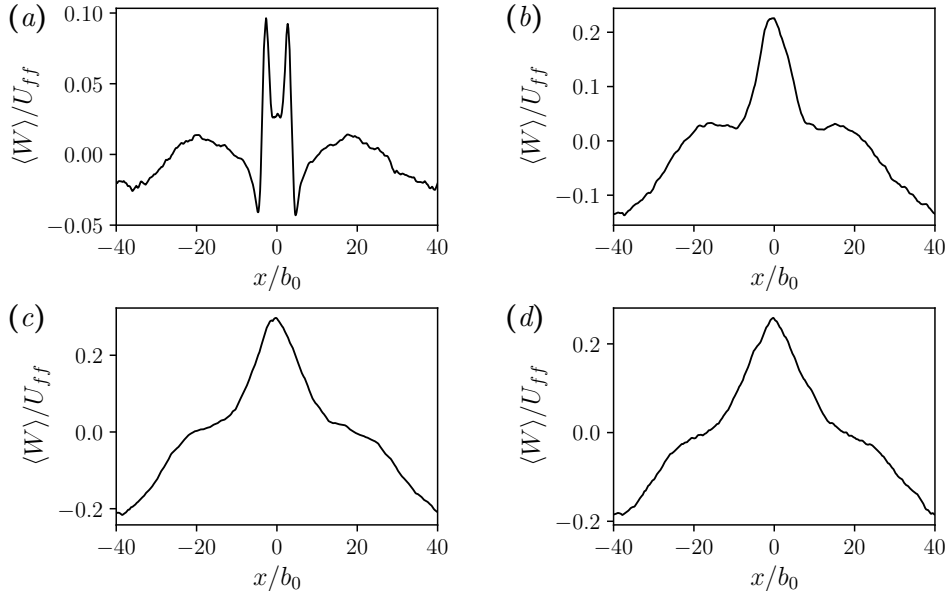

Figure B.10: Mean vertical velocity profile at different height along the cross-flow direction: (a) $z/b_0 = 1$, (b) $z/b_0 = 5$, (c) $z/b_0 = 10$,(d) $z/b_0 = 15$.

B.7.1 Two-point correlation

Figure B.12 shows the autocorrelation functions along the homogeneous direction y, of temperature and velocity fluctuations for the two-plume configuration, evaluated at the same streamwise and vertical locations as in the single-plume case. Compared to the single-plume configuration, all three autocorrelation functions exhibit more pronounced negative peaks. In par-

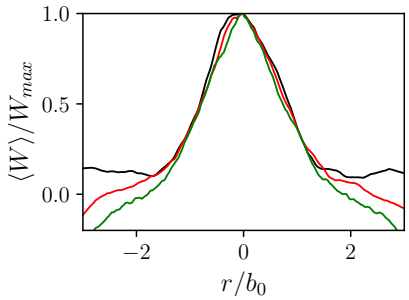

Figure B.11: Normalized vertical velocity profiles using the maximum velocity and the half-width of the plume at the height of the considered profile. Black curve $z/b_0 = 5$, red $z/b_0 = 10$ and green for $z/b_0 = 15$

ticular, the autocorrelation of the vertical velocity fluctuations, figure B.12 (c), which remained strictly positive in the single-plume case, now displays a clear negative peak, with a trend similar to that observed for temperature fluctuations. This behaviour indicates that plume interaction reduces the lateral coherence of the vertical velocity field, leading to alternating upward and downward motions along the homogeneous direction.

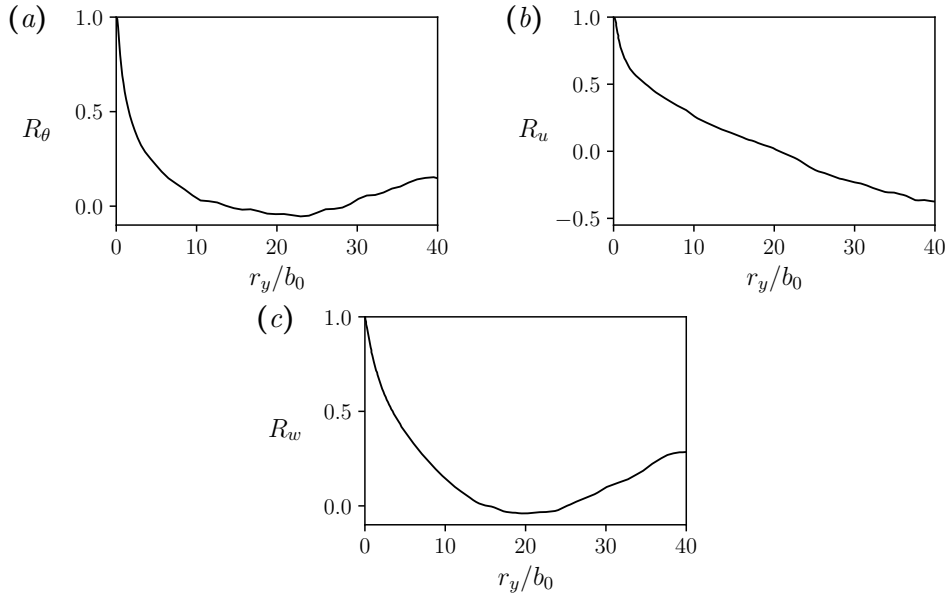

Figure B.12: Two points correlation functions along y: (a) temperature θ , (b) cross flow velocity u and (c) vertical velocity w

B.8 Conclusion

In this thesis work, direct numerical simulations were employed to investigate and characterize first a single planar plume and subsequently the interaction between two such plumes. The analysis of the single plume initially allowed the identification of the main features of a generic plume, by distinguishing the region close to the source from the region farther downstream, commonly referred to as the far field. Phenomena such as necking, characteristic of plumes originating from finite size sources, and puffing, corresponding to the periodic formation of vortical structures near the plume axis, were observed. The subsequent analysis of two parallel heat sources enabled a deeper understanding of the interaction process between plumes, commonly known as the Coandă effect. The results show that the two flows merge at a relatively short distance from the sources, while preserving characteristic plume features already observed in the single plume configuration. Overall, the numerical results are in good agreement with classical plume theory Future studies, may deeper investigate the coalescence and entrainment process by applying two points statistics and budget analysis, and by extending the investigation to unconfined plumes configuration.

Acknowledgements

At the end of this journey, I would like to express my gratitude to my supervisor, Professor Andrea Cimarelli, a true inspiration. Thank you for all your support and for encouraging me at every step since the beginning. I would also like to thank Professor Enrico Stalio for his availability and support.

I would like to thank my friends in Delft for welcoming me and for never letting me feel homesick. You will always have a special place in my heart: Sanath, Giando, Letizia, Shaina, Baptiste, Tarun, Muhammad, Surya, Marko, Heng, Rafael, Teja, Asif, Pietro, and above all Dr. Pedro Costa, to whom I am sincerely grateful for his availability, discussions and support. and for giving me the opportunity to spend six months at TU Delft. *Dankjewel!*

To my dearest paranymphs, Gabriele and Roberto, and to my other office colleagues, Marco, Yves, Filippo, Lorenzo, and Daniele, thank you so much for all the moments we shared and for all the support you gave me throughout these three years.

To all the Cevapcici, Ele, Franci, Lisa, Matteo, Stefi, Thea & Carlo, Ceci, Lorenzon, Giulia, Mattia, Marty, thank you for all the adventures we have shared. Finally, to my friends in Modena, Stefano, Razie, Francesco, Serena, Annina, Panna, Luccia, to name a few, thank you for always being there.

Infine, un ringraziamento particolare va ai miei genitori Karin, Paolo e mia sorella Alessia, che mi hanno sempre insegnato a seguire i miei sogni e a non mollare mai. Grazie per ogni sacrificio e soprattutto per il sostegno che mi avete offerto in ogni momento. Non sarei la persona che sono oggi senza di voi e senza quelle quattro stelle lassù.

Tesi di dottorato finanziata dall'Unione europea - Next Generation EU, Missione 4, componente 1 "Potenziamento dell'offerta dei servizi di istruzione: dagli asili nido all'Università" - Investimento 4.1 "Estensione del numero di dottorati di ricerca e dottorati innovativi per la pubblica amministrazione e il patrimonio culturale".

Bibliography

A. Abd Razak, A. Hagishima, N. Ikegaya, and J. Tanimoto. Analysis of airflow over building arrays for assessment of urban wind environment. *Building and Environment*, 59:56–65, 2013.

A. Arakawa. The cumulus parameterization problem: Past, present, and future. *J. Clim.*, 17(13):2493–2525, 2004.

J. Barlow and O. Coceal. A review of urban roughness sublayer turbulence. Technical Report Technical Report No. 527, Meteorology Research and Development, Met Office, 2008.

J. Barlow, M. Best, S. I. Bohnenstengel, P. Clark, S. Grimmond, H. Lean, A. Christen, S. Emeis, M. Haeffelin, I. N. Harman, et al. Developing a research strategy to better understand, observe, and simulate urban atmospheric processes at kilometer to subkilometer scales. *Bull. Am. Meteorol. Soc.*, 98(10):ES261–ES264, 2017.

M. Belda, J. Resler, J. Geletič, P. Krč, B. Maronga, M. Sühring, M. Kurppa, F. Kanani-Sühring, V. Fuka, K. Eben, et al. Sensitivity analysis of the palm model system 6.0 in the urban environment. *Geoscientific Model Development*, 14(7):4443–4464, 2021.

K. Bhaganagar and S. R. Bhimireddy. Numerical investigation of starting turbulent buoyant plumes released in neutral atmosphere. *J. Fluid Mech.*, 900:A32, 2020.

L. P. Blunn, O. Coceal, N. Nazarian, J. F. Barlow, R. S. Plant, S. I. Bohnenstengel, and H. W. Lean. Turbulence characteristics across a range of idealized urban canopy geometries. *Boundary-Layer Meteorol.*, 182(2): 275–307, 2022.

C. S. Bretherton. A theory for nonprecipitating moist convection between two parallel plates. Part I: Thermodynamics and "linear" solutions. *J. Atmos. Sci.*, 44(14):1809–1827, 1987.

I. P. Castro, Z.-T. Xie, V. Fuka, A. G. Robins, M. Carpentieri, P. Hayden, D. Hertwig, and O. Coceal. Measurements and computations of flow in an urban street system. *Boundary-Layer Meteorol.*, 162(2):207–230, 2017.

B. Chen, W. Wang, W. Dai, M. Chang, X. Wang, Y. You, W. Zhu, and C. Liao. Refined urban canopy parameters and their impacts on simulation of urbanization-induced climate change. *Urban Clim.*, 37:100847, 2021.

F. Chillà and J. Schumacher. New perspectives in turbulent rayleigh-bénard convection. *Eur. Phys. J. E*, 35:1–25, 2012.

A. Cimarelli, A. Fenzi, D. Angeli, and E. Stalio. Assessment of the oberbeck–boussinesq approximation for buoyancy-driven turbulence in air. *Int. J. Heat Mass Transfer*, 243:126851, 2025.

J. F. Clarke. Nocturnal urban boundary layer over cincinnati, ohio. *Monthly Weather Review*, 97(8):582–589, 1969.

O. Coceal, T. G. Thomas, I. P. Castro, and S. E. Belcher. Mean flow and turbulence statistics over groups of urban-like cubical obstacles. *Boundary-Layer Meteorol.*, 121(3):491–519, 2006.

P. Costa. A FFT-based finite-difference solver for massively-parallel direct numerical simulations of turbulent flows. *Comput. & Math. App.*, 76(8): 1853–1862, 2018.

B. Devenish, G. Rooney, and D. Thomson. Large-eddy simulation of a buoyant plume in uniform and stably stratified environments. *J. Fluid Mech.*, 652:75–103, 2010.

A. Ezzamel, P. Salizzoni, and G. R. Hunt. Dynamical variability of axisymmetric buoyant plumes. *J. Fluid Mech.*, 765:576–611, 2015.

Y. Fan, Q. Wang, J. Ge, and Y. Li. Conditions for transition from a plume to a dome above a heated horizontal area. *Int. J. Heat Mass Transfer*, 156:119868, 2020.

T. Fanneløp and D. Webber. On buoyant plumes rising from area sources in a calm environment. *J. Fluid Mech.*, 497:319–334, 2003.

M. G. Giometto, A. Christen, C. Meneveau, J. Fang, M. Krafczyk, and M. B. Parlange. Spatial characteristics of roughness sublayer mean flow and turbulence over a realistic urban surface. *Boundary-Layer Meteorol.*, 160(3):425–452, 2016.

Gmsh Reference Manual. Gmsh reference manual. `http://gmsh.info/`, 2026. 2026-02-16.

D. D. Gray and A. Giorgini. The validity of the boussinesq approximation for liquids and gases. *Int. J. Heat Mass Transfer*, 19(5):545–551, 1976.

T. Hattori, S. E. Norris, M. P. Kirkpatrick, and S. W. Armfield. Simulation and analysis of puffing instability in the near field of pure thermal planar plumes. *Int. J. Therm. Sci.*, 69:1–13, 2013.

L. Howard. The climate of london vol 1 (london: W phillips, sold also by j and a arch), 1818.

G. Hunt and T. Van den Bremer. Classical plume theory: 1937–2010 and beyond. *IMA J. Appl. Math.*, 76(3):424–448, 2011.

D. Jiang, W. Jiang, H. Liu, and J. Sun. Systematic influence of different building spacing, height and layout on mean wind and turbulent characteristics within and over urban building arrays. *Wind Struct.*, 11(4): 275–290, 2008.

N. Kabisch, F. Remahne, C. Ilsemann, and L. Fricke. The urban heat island under extreme heat conditions: a case study of hannover, germany. *Sci. Rep.*, 13(1):23017, 2023.

M. Kanda, A. Inagaki, T. Miyamoto, M. Gryschka, and S. Raasch. A new aerodynamic parametrization for real urban surfaces. *Boundary-Layer Meteorol.*, 148(2):357–377, 2013.

J. u. R. Khan and S. Rao. Properties of the turbulent/non-turbulent layer of a turbulent boussinesq plume: A study using direct numerical simulation. *Phys. Fluids*, 35(5), 2023.

R. Kotharkar, A. Ramesh, and A. Bagade. Urban heat island studies in south asia: A critical review. *Urban Clim.*, 24:1011–1026, 2018.

S. Leonardi and I. P. Castro. Channel flow over large cube roughness: a direct numerical simulation study. *J. Fluid Mech.*, 651:519–539, 2010.

J. Lu, S. P. Arya, W. H. Snyder, and R. E. Lawson Jr. A laboratory study of the urban heat island in a calm and stably stratified environment. Part I: Temperature field. *J. Appl. Meteorol.*, 36(10):1377–1391, 1997.

A. Makedonas, M. Carpentieri, and M. Placidi. Urban boundary layers over dense and tall canopies. *Boundary-Layer Meteorol.*, 181(1):73–93, 2021.

B. Maronga, S. Banzhaf, C. Burmeister, T. Esch, R. Forkel, D. Fröhlich, V. Fuka, K. F. Gehrke, J. Geletič, S. Giersch, et al. Overview of the palm model system 6.0. *Geoscientific Model Development*, 13(3):1335–1372, 2020.

V. Masson, W. Heldens, E. Bocher, M. Bonhomme, B. Bucher, C. Burmeister, C. de Munck, T. Esch, J. Hidalgo, F. Kanani-Sühring, et al. City-descriptive input data for urban climate models: Model requirements, data sources and challenges. *Urban Clim.*, 31:100536, 2020.

B. R. Morton, G. I. Taylor, and J. S. Turner. Turbulent gravitational convection from maintained and instantaneous sources. *Proc. R. Soc. Lond. A*, 234(1196):1–23, 1956.

C. Muller and S. Abramian. The cloud dynamics of convective storm systems. *Physics Today*, 76(5):28–33, 2023.

F. Nicoud and F. Ducros. Subgrid-scale stress modelling based on the square of the velocity gradient tensor. *Flow Turb. Comb.*, 62(3):183–200, 1999.

T. R. Oke, G. Mills, A. Christen, and J. A. Voogt. *Urban climates*. Cambridge university press, 2017.

OpenFOAM Foundation. Openfoam user guide. `https://www.openfoam.org`, 2024. Version 2406.

O. Pauluis and J. Schumacher. Idealized moist rayleigh–bénard convection with piecewise linear equation of state. *Commun. Math. Sci.*, 8(1):295–319, Mar. 2010.

O. Pauluis and J. Schumacher. Self-aggregation of clouds in conditionally unstable moist convection. *Proc. Natl. Acad. Sci. U.S.A.*, 108(31):12623–12628, 2011.

E. Rostami, N. Nasrollahi, and J. Khodakarami. A comprehensive study of how urban morphological parameters impact the solar potential, energy consumption and daylight autonomy in canyons and buildings. *Energy Build.*, 305:113904, 2024.

A. Shabbir and W. K. George. Experiments on a round turbulent buoyant plume. *J. Fluid Mech.*, 275:1–32, 1994.

O. Shishkina, R. J. Stevens, S. Grossmann, and D. Lohse. Boundary layer structure in turbulent thermal convection and its consequences for the required numerical resolution. *New J. Phys.*, 12(7):075022, 2010.

G. Speziali. Direct numerical simulation of turbulent plumes. Master's thesis, Università di Modena e Reggio Emilia, 2024. ETD etd-03262024-085446.

G. L. Stephens. Cloud feedbacks in the climate system: A critical review. *J. Clim.*, 18(2):237–273, 2005.

I. Suter, T. Grylls, B. S. Sützl, S. O. Owens, C. E. Wilson, and M. van Reeuwijk. udales 1.0: a large-eddy simulation model for urban environments. *Geoscientific Model Development*, 15(13):5309–5335, 2022.

B. Sützl, G. G. Rooney, and M. van Reeuwijk. Drag distribution in idealized heterogeneous urban environments. *Boundary-Layer Meteorol.*, 178:225–248, 2021.

B. S. Sutzl. *Rising from the ground: Distributed drag parameterization of urban environments for numerical weather prediction.* PhD thesis, Imperial College London, 2021.

B. Sützl and M. van Reeuwijk. bss116/citygenerator: Urban Landscape Generator v1.0, 2020. URL `https://doi.org/10.5281/zenodo.3747476`.

J.-C. Tisserand, M. Creyssels, Y. Gasteuil, H. Pabiou, M. Gibert, B. Castaing, and F. Chillà. Comparison between rough and smooth plates within the same rayleigh–bénard cell. *Phys. Fluids*, 23(1), 2011.

T. S. Van den Bremer and G. R. Hunt. Two-dimensional planar plumes and fountains. *J. Fluid Mech.*, 750:210–244, 2014.

E. P. Van Der Poel, R. Ostilla-Mónico, J. Donners, and R. Verzicco. A pencil distributed finite difference code for strongly turbulent wall-bounded flows. *Comput. Fluids*, 116:10–16, 2015.

F. Venturelli. Simulazioni les di un caso paradigmatico di isola di calore urbana. Master's thesis, Università di Modena e Reggio Emilia, 2025.

Q. Wang, J. Hang, Y. Fan, and Y. Li. Urban plume characteristics under various wind speed, heat flux, and stratification conditions. *Atmos. Environ.*, 239:117774, 2020.

T. Weidauer, O. Pauluis, and J. Schumacher. Cloud patterns and mixing properties in shallow moist rayleigh–bénard convection. *New J. Phys.*, 12 (10):105002, 2010.

C. Wilson, J. K. Shonk, S. I. Bohnenstengel, A. Paschalis, and M. van Reeuwijk. Microscale to neighbourhood scale: Impact of shading on urban climate. *Building and Environment*, 275:112721, 2025.

C. E. Wilson, J. K. Shonk, S. I. Bohnenstengel, A. Paschalis, and M. Van Reeuwijk. Parameter investigation for urban surface-energy balance: A large-eddy simulation study. *Q. J. R. Meteorol. Soc.*, page e70154, 2026.

Z. Xie and I. P. Castro. Les and rans for turbulent flow over arrays of wall-mounted obstacles. *Flow Turb. Comb.*, 76(3):291–312, 2006.

Z.-T. Xie and I. P. Castro. Large-eddy simulation for flow and dispersion in urban streets. *Atmos. Environ.*, 43(13):2174–2185, 2009.

Z.-T. Xie, O. Coceal, and I. P. Castro. Large-eddy simulation of flows over random urban-like obstacles. *Boundary-Layer Meteorol.*, 129(1):1–23, 2008.

C. Xu, C. Zhang, L. Brandt, J. Song, and O. Shishkina. Direct numerical simulations of turbulent rayleigh–bénard convection with polymer additives. *J. Fluid Mech.*, 1014:A22, 2025.

J. Yang and E. Balaras. An embedded-boundary formulation for large-eddy simulation of turbulent flows interacting with moving boundaries. *J. Comput. Phys.*, 215(1):12–40, 2006.

E. Zadro. Moist turbulent rayleigh-bénard convection. Master's thesis, Università di Modena e Reggio Emilia, 2025. ETD etd-03202025-142236.

Y.-Z. Zhang, C. Sun, Y. Bao, and Q. Zhou. How surface roughness reduces heat transport for small roughness heights in turbulent rayleigh–bénard convection. *J. Fluid Mech.*, 836:R2, 2018.